School of Architecture, Civil and Environmental Engineering

Structural concrete laboratory IBETON

Crack kinematics prediction in concrete structures and assessment of their criticality

In partial fulfillment of the requirements for the degree of

Master of Science MSc in Civil Engineering

Submitted by:

Ludivine Menoud

Supervisor:

Professor Aurelio Muttoni
Full Professor, Structural Concrete Laboratory IBETON, EPFL

Tutors:

Enrique Corres Sojo and Marko Pejatovic
Doctoral Assistants, Structural Concrete Laboratory IBETON, EPFL

June 23, 2023

Abstract

The observation of cracks in normally functioning reinforced concrete (RC) structures is expected as the tensile strength of concrete is relatively low. However, one or more of those cracks can start to propagate with increasing crack openings, localizing strains and potentially indicating structural safety shortcomings.

In the present project, RC members with low amounts of transverse reinforcements subjected to shear forces have been studied with the help of digital image correlation (DIC). In such structures, a critical shear crack (CSC) typically develops rapidly and can cause brittle failures. Assessing the criticality of such a crack could be a useful tool for engineers to prevent unpredictable failures that can be deadly.

The present study is in continuation of Hugo Nick's Master thesis (2023) [17] where the first avenue of a method to predict crack kinematics evolution from a given initial state was proposed. Obtaining reliable predictions of the failure crack kinematics in RC members with shear reinforcements proved to be challenging. Indeed, several hypotheses valid for RC elements without shear reinforcement must be questioned even for elements with low shear reinforcement ratios, notably the rigid-body hypothesis. The presence of stirrups and secondary cracks connected to the CSC strongly influence its kinematics and create a complicated deformation scheme with local flexion. Only approximative predictions have been achieved in the present study and the crack kinematics prediction question remains open.

Knowing the crack kinematics allows to compute the shear transfer actions (STA). Identifying the load level at which the sum of the STA start decaying as the actual shear force continues to augment could indicate an unstable crack propagation and the structure's imminent failure. A decrease of the total STA was indeed observed around 90% of the ultimate load for the specimens with a shear reinforcement ratio $\rho_w > 0.1\%$, but not on the other specimens. Individually studying the STA revealed a high sensitivity of the residual tensile strength of concrete to the minimal crack width considered, and by extension the DIC error. It was also the case to a lesser extent for aggregate interlock. This parameter should be carefully selected. Even though the individual STA show variability across load levels and specimens, the statistical analysis of the sum of the STA for all SM10 specimens demonstrates that it follows the applied load relatively closely.

An attempt at understanding the CSC propagation as a function of the load level was also conducted and lead to the discovery of a load-propagation experimental relationship depending on the position of the failure crack tip at an initial load level and approximately proportional to the square of the shear reinforcement ratio. This relation offers an estimation that captures the general load-propagation trend despite the variability on the actual crack propagation. It was applicable on all tested specimens but could be limited to their specific experimental conditions. An attempt to predict the ultimate load has also been conducted using this load-propagation empirical relationship.

A common way of determining whether a RC structure is close to failure or not is to compare the acting loads with the strength obtained from nonlinear finite element analysis (NLFEA) . However, its application on RC elements with localised cracking, such as low transverse reinforcement ratio beams subjected to shear can lead to unrealistically high results. Mesh sensitivity and localisation issues were identified in the tested models. It is therefore important to study the limitations of NLFEA in such cases that differ from the habitual scope in order to avoid misinterpretation of the results.

Acknowledgements

I would like to express my gratitude to the people who accompanied me during my Master project :

Professor Aurelio Muttoni, my supervisor whose experience and exceptional insight in the field of concrete structures guided this project.

Doctoral assistants Marko Pejatovic and Enrique Corres, for their availability and help in literature research and software use, as well as their sound advice and explanations.

Dr Frédéric Monney for sharing and explaining the laboratory experiences conducted during his doctoral thesis on which the present study is based.

Dr João Simões for his valuable advice on finite element modelling and general reinforced concrete behaviour.

Dr Qianhui Yu for her help on jconc source code.

Dr Olivier Burdet for IT support.

Hugo Nick whose master's thesis brought out the first ideas of the research topic continued in my project.

Table of contents

1 Introduction

Cracks in concrete structures occur when the concrete tensile stress exceed its tensile strength. Several causes can lead to cracking of a reinforced concrete (RC) member, such as shrinkage, alkali-aggregate reaction, temperature gradient, frost, loads, creep etc. The observation of small cracks is not necessarily alarming in itself since they are expected with RC normal functioning. Indeed, the tensile strength of concrete is relatively low. It is therefore not surprising to find cracks, particularly in the tensed zones where the reinforcing steel ensures the transmission of the tension force. However, one or more of those cracks can start to propagate with increasing crack openings, localizing strains, which potentially indicates a structural strength deficiency.

This is the case for example in RC members with insufficient amounts of transverse reinforcements subjected to shear forces, where a critical shear crack (CSC) typically develops and cause the elements failure once the ultimate load is reached. Brittle shear failures tend to develop rapidly and are particularly dreaded in concrete structures.

The laboratory experiments of Monney (2022) [14] studied in the present project comprises such specimens with low shear reinforcement ratios and varying stirrups steel ductility classes. High precision measurements have been conducted on these specimens using digital image correlation (DIC), a recently developped instrumentation technique resulting in dense full-field surface displacements data. DIC is frequently used to detect cracks and measure their kinematics in laboratory experiments. In addition, fibre-optical measurements (FOM) of the longitudinal reiforcements and stirrups are availible and help to understand the rebars behaviour.

The present study is in continuation of Hugo Nick's Master thesis (2023) [17] on automatic crack detection in concrete structures. Hugo Nick proposed a method to predict crack kinematics evolution from a given initial state that could potentially be applied on all types of cracks. However, obtaining a prediction for the rigid-body rotation increment was unsuccessful. The method is further developed in the present project.

Understanding the CSC propagation as a function of the load level is also a potentially interesting research avenue that has been quickly explored in the present project, as it could help kinematics prediction using pre-existing relations such as the ones developed by Cavagnis et al. (2018) [8].

The total shear strength of a concrete member can be divided into different types of shear transfer actions (STA), usually classified as inclined compression chord action, cantilever action, residual tensile strength of concrete, dowel action, aggregate interlock action and stirrups contribution for concrete members with transverse reinforcement. Knowing the crack kinematics and concrete strain field allowed to compute the shear transfer actions (STA) of the test specimens.

Visual inspection is now a common way for engineers to detect cracks in existing structures. The crack opening is often punctually measured by hand, and the evaluation of its criticality is strongly based on the personal experience of the inspecting engineer. Studying the evolution of the total STA along the load level could give information on the crack criticality. Indeed, when the STA start decaying as the actual shear force continues to augment due to the crack lips disengagement, an unstable crack propagation can occur, indicating the specimen's imminent failure.

A common way of determining whether a RC structure is close to failure or not is to compare the acting loads with the strength obtained from a theoretical calculation. A relatively advanced method to quantify the strength of a RC member is the use of nonlinear finite element analysis (NLFEA). NLFEA

considers a continuous medium and perfect bound between concrete and reinforcements, which does not correspond to the real cracked state of concrete. NLFEA is in practice generally applied to RC elements with well-distributed and sufficient steel reinforcements, so that smeared cracking and stress redistribution can occur. Its application on RC elements with localised cracking, such as beams with low transverse reinforcement ratio subjected to shear can lead to unrealistic results. As a last chapter of the present study, different NLFEA calculations have been compared to the laboratory experiments of Monney (2022) [14] in order to better understand its limitations with specimens with low shear reinforcement ratio.

2 Literature review

2.1 Crack types and development

A crack is an abrupt discontinuity dividing an originally continuous medium into two parts caused by a local rupture of the material. Cracks geometry and behaviour vary under the applied solicitations. Three main crack opening modes are generally listed in literature. Mode I cracks open normal to the crack surface and are linked with tensile stresses perpendicular to the crack plane. Mode II cracks open parallel to the crack surface and follow shear stresses in the plane of the element. Mode III crack are also due to shear stresses in the plane of the element, but they open out-of-plane of the element. (Pantoja-Rosero et al. (2022) [21])

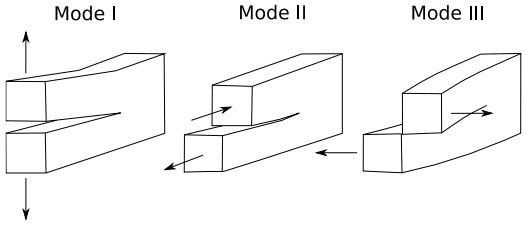

Figure 1 – Fracture propagation modes. Pantoja-Rosero et al. (2022) [21]

Cavagnis et al. [4] analysed in 2015 shear cracks development based on test results of shear failures in RC members without transverse reinforcement. The cracking patterns and their kinematics were precisely tracked using high-frequency photogrammetric techniques to expand the knowledge on the actual crack development during the process of failure. To better describe the failure process, a typology of cracks occurring during and before shear failure was introduced. The different types are illustrated in Table 1 and Figure 2.

Table 1 - Description of the crack types elaborated in the paper of Cavagnis et al. (2015) [4]

Type	Origin	Comments
A	Primary flexural crack	Cracks on the tensed side of a bent slab. They are perpendicular to the surface in the absence of shear force and get more and more inclined as the shear force increases towards the supports.
B	Secondary flexural crack	Same origin as type A but shorter.
C	Merging of type A and type B	-
D	Delamination (doweling) crack	Type D' develops at the same time as type A. Cracks type D'' or D''' (with delamination crack) are usually develop (according to photogrammetric measurements) after the maximum load was reached.
E	Aggregate interlock cracks	Aggregate interlock cracks type E occurs when an existing pure tension crack is subsequently subjected to shear displacements, inclined cracks develop due to the local aggregate interlock forces.
F	Propagation of a primary flexural crack within the compression chord.	Cracks type F propagated at load levels close to failure for low values of the acting moments (crack near support or point of moment inflection) whereas it developed already for relatively low load levels when the acting bending moment was significant.
G	Development of a crack within the compression chord but not originating from a primary flexural crack.	These cracks usually develop perpendicular to the edge of the slab.

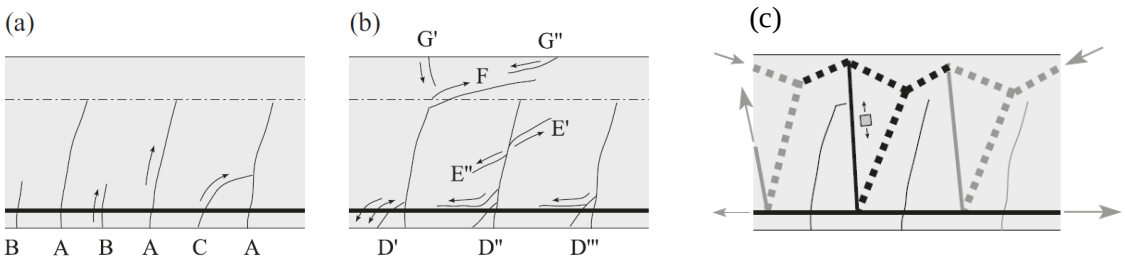

Figure 2 - Crack types and cantilever action in RC members without shear reinforcements: (a) primary and secondary flexural cracks; and (b) cracks originated by the shear-transfer actions (see chapter §2.4); (c) cantilever action. Cavagnis et al. (2015) [4]

The concrete segments between two type A primary flexural cracks, called Kani's teeth, act as cantilever beams that transfer shear between the tension and compression chord of a reinforced concrete member via the strut and tie model illustrated in Figure 2 (c). The tension force in the reinforcement on either side of a tooth varies due to the concrete bond between, bending the tooth and ultimately breaking its top where the tensile strength of concrete is reached, approximately at the section's neutral axis height. This creates a type F crack that propagates diagonally in the compression chord. (Classen (2020) [5])

As the shear force increases, one of these cracks is susceptible to develop in a major crack called critical shear crack (CSC) (see chapter §2.2) that limits the shear strength of the concrete element and whose development leads to failure of the concrete member. (Cavagnis et al. (2017) [3])

Cavagnis et al. (2017) [3] emphasizes the importance of distinguishing the CSC and the final failure surface developing near ultimate load that may partly differ from the CSC. They identified four critical crack development types (CCDT) illustrated in Figure 3 and commented in Table 2. It was observed that different failure modes can lead to similar shear capacity, thus similar specimens tested in shear can present different CCDT.

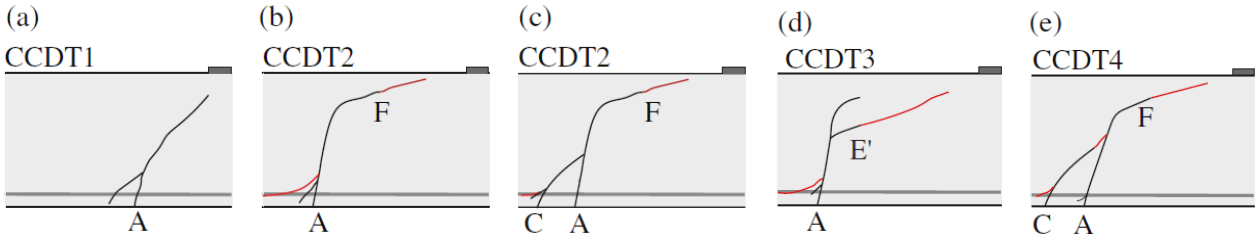

Figure 3 - (a–e) Critical Shear Crack Development Types (CCDT); black: cracks until maximum load; red: cracks after maximum load. . Cavagnis et al. (2017) [3]

Table 2 - Description of the critical crack development types (CCDT) elaborated in the paper of Cavagnis et al. (2017) [3]

Type	Principle
CCDT1	Full arching action can develop above the CSC, allowing a direct compression strut between the load and the support.
CCDT2	Stable propagation of the CSC from a primary flexural crack type A to a quasi-horizontal crack type F in the compression chord. A secondary flexural crack type C can also join the CSC (Figure 3 c)).
CCDT3	Propagation of the CSC from a primary flexural crack type A to a quasi-horizontal crack type E' originating from local high aggregate interlock stresses.
CCDT4	A secondary flexural crack type C causes failure by merging with the CSC formed by cracks type A and F.

2.2 Critical Shear Crack Theory

The Critical Shear Crack Theory (CSCT) was developed by Muttoni & Fernández (2008) [16] with the objective of proposing a rational model to estimate the shear strength of reinforced concrete members without shear reinforcements. The assumption governing the Critical Shear Crack Theory (CSCT) is that the shear strength of slender reinforced concrete members without shear reinforcements depends on the development of a critical shear crack (CSC). The strength of the theoretical inclined compression strut that carried shear is limited by the CSC development. This theory links the deformation capacity of a concrete member and its shear strength through a failure criterion. Higher strength members are related to lower deformation capacities. (Cavagnis et al. (2018) [8])

CSCT estimates the crack width w in the critical shear region accounting for the compressive strength of concrete f_c and the crack surface roughness, defined after the maximum aggregate size d_g. This relation is based on several hypotheses. Firstly, the width of the CSC in the considered section can be represented by the strain at a depth of $0.6 \cdot d$ from the compression face as illustrated in Figure 4. Secondly, the CSC opening w is proportional to the product of the longitudinal strain ε in a control section times the effective depth d of the member: $w \propto \varepsilon \cdot d$. This is one of the principal CSCT assumption and its validity has been confirmed by experimental investigations using DIC measurements by Cavagnis et al. (2017) [3]. The strain ε can be obtained through a cracked sectional analysis. The following relation is valid in the absence of axial force for a rectangular section without skin reinforcements on the side faces with the bending moment M in the critical section.

$$\varepsilon = \frac{M}{bd\rho E_s(d-c/3)} \cdot \frac{0.6d-c}{d-c} \tag{1}$$

$$c = d\rho \frac{E_s}{E_c}\left(\sqrt{1+\frac{2E_c}{\rho E_s}}-1\right) \tag{2}$$

c is the depth of the compression zone and the Young modulus of concrete can be estimated as $E_c \cong 10000 f_c^{1/3}$.

Finally, the shear strength can be defined after these assumptions as:

$$\frac{V_R}{bd\sqrt{f_c}} = \frac{1}{6} \cdot \frac{2}{1+120\frac{\varepsilon \cdot d}{16+d_g}} \tag{3}$$

with b the section width and d its effective depth.

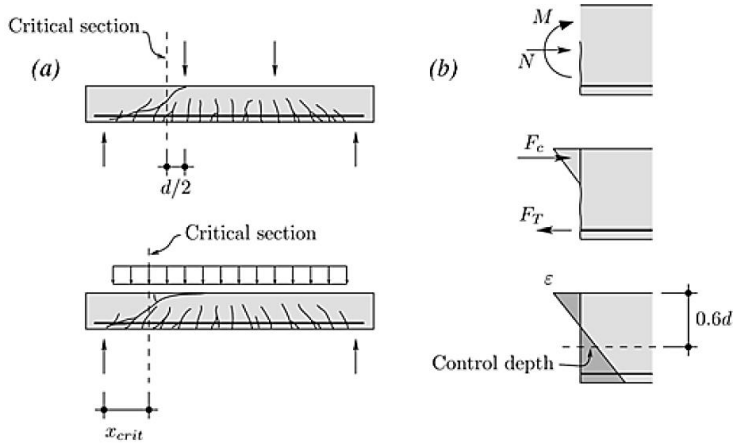

Figure 4 - Critical shear crack model: (a) critical section for point loading and distributed loading; and (b) determination of longitudinal strain in control depth using internal forces N and M. Muttoni & Fernández (2008) [16]

2.3 Crack kinematics

Crack kinematics describe how the crack lips move in relation to each other.

Crack locations and kinematics measurements can be fully extracted using digital image correlation (DIC), a full field optical measuring technique using digital cameras to measure surface geometry, displacement, and strain. (Nonis et al. (2013) [20]) DIC measures provide highly accurate quasi-continuous surface displacement measurements in time and space, even for cracks that are hardly visible to the naked eye.

However, the accuracy and precision of the DIC measurements strongly depend on the configuration and image resolution. The camera calibrations need a trained operator to obtain accurate measurements. Data smoothing can also improve the quality of the results to reduce DIC noise. (Gehri et al. (2020) [18])

Another downside of DIC techniques is the surface preparation required, that is the black speckle pattern applied to track points on a previously white painted area. This can be time consuming and invasive on an existing structure in use, which limits DIC measurements primarily to laboratory experiments even if on-site structures are also possible. (Pantoja-Rosero et al. (2022) [21]) For example, Nonis et al. (2013) [20] presented one of the early promising measurement tests using DIC for bridge structural health monitoring.

The kinematics measurement method proposed by Campana et al. (2013) [2] was used for the SM10 and SM00 laboratory experiments series performed by Monney in his PhD thesis (2022) [14] and described in chapter §3. Reference points were placed on each side of the cracks and the displacements extracted from the DIC measurements using VIC software. The crack kinematics were then obtained using Campana's method illustrated in Figure 5.

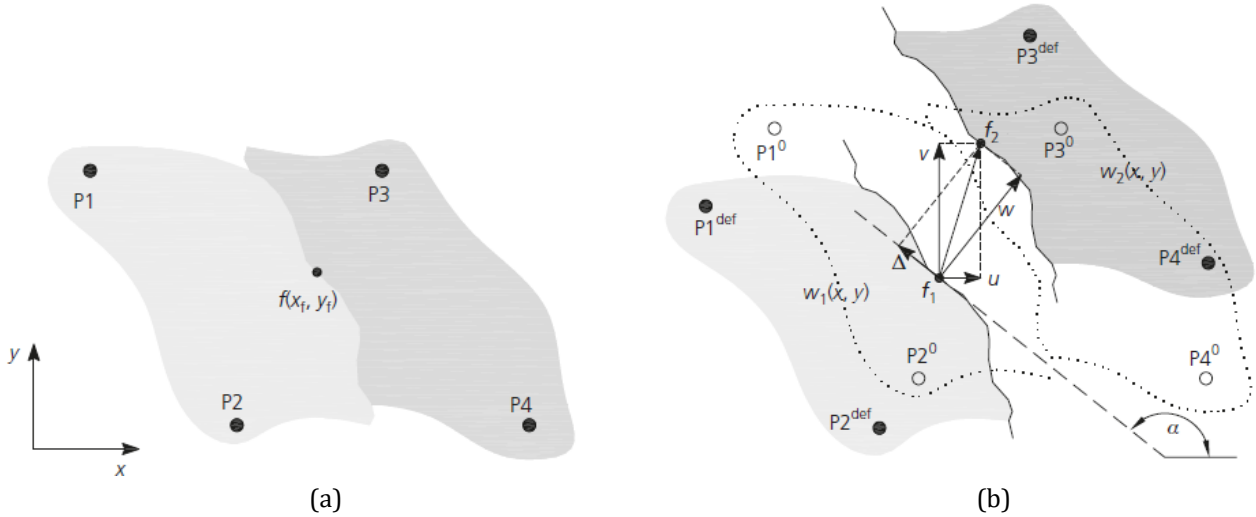

Figure 5 - Measurements for calculation of crack kinematics: (a) undeformed configuration; (b) deformed configuration. Campana et al. (2013) [2]

Cavagnis et al. (2018) [8] studied the crack kinematics of RC members without shear reinforcements and proposed a bi-linear approximation of the CSC. It comprises a quasi-vertical segment whose inclination is related to the moment-to-shear ratio and a quasi-horizontal segment up to the tip of the crack. The kinematics of the bi-linear approximated crack is shown in Figure 6.

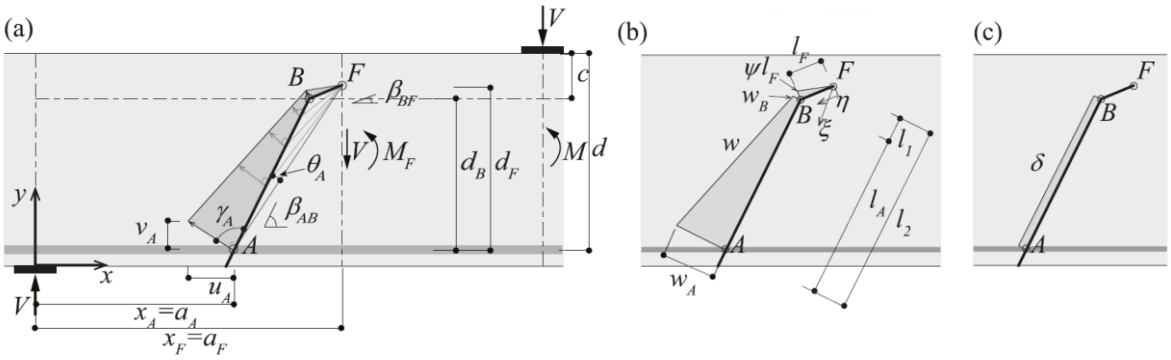

Figure 6 - (a) Kinematics and displacements of the crack lips according to the adopted crack shape; (b) crack opening w perpendicular to the crack surface and (c) sliding δ. Cavagnis et al. (2018) [8]

Supported by experimental investigations illustrated in Figure 7, the center of rotation can be assumed at the tip of the crack. The crack rotation can then be derived by the following relationship:

$$\psi = \frac{u_A}{d_F} = \frac{\varepsilon_s \cdot l_{trib}}{d_F} \tag{4}$$

with u_A and ε_s respectively the horizontal crack opening and strain at the level of the flexural reinforcement in tension, $l_{trib} = d - c$ the contributing length to the opening of the crack, and d_F the vertical distance from the tip of the crack to the flexural reinforcements. The crack opening and sliding can be defined after the shape and kinematics. The quasi-horizontal segment of the crack is characterized by pure opening (Mode I), whereas the quasi-vertical one comprises a mix of crack opening and sliding (Mode I-II).

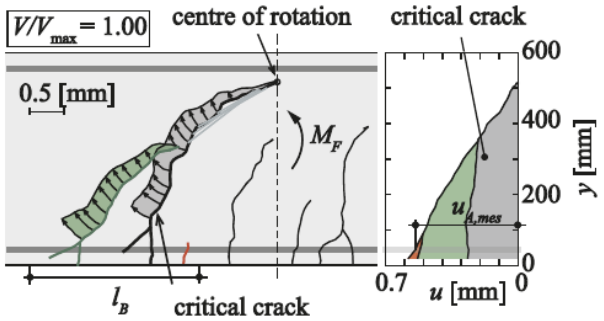

Figure 7 - Crack kinematics, center of rotation and horizontal opening u of the cracks tributary to the opening of the critical shear crack in a region of length l_B. Cavagnis et al. (2018) [8]

2.4 Shear transfer actions

The crack kinematics measurements obtained after the procedure described in chapter §2.3, as well as the concrete surface DIC strain field, allow to compute the shear transfer actions (STA). Indeed, the total shear strength of a concrete member can be divided into different types of STA that have been described by Cavagnis et al. (2015) [4] for RC members without shear reinforcement. They are usually classified as inclined compression chord action, cantilever action, residual tensile strength of concrete, dowel action and aggregate interlock action. For concrete members with transverse reinforcement, the stirrups contribution is added. The different STA are illustrated in Figure 8 and defined in Table 3.

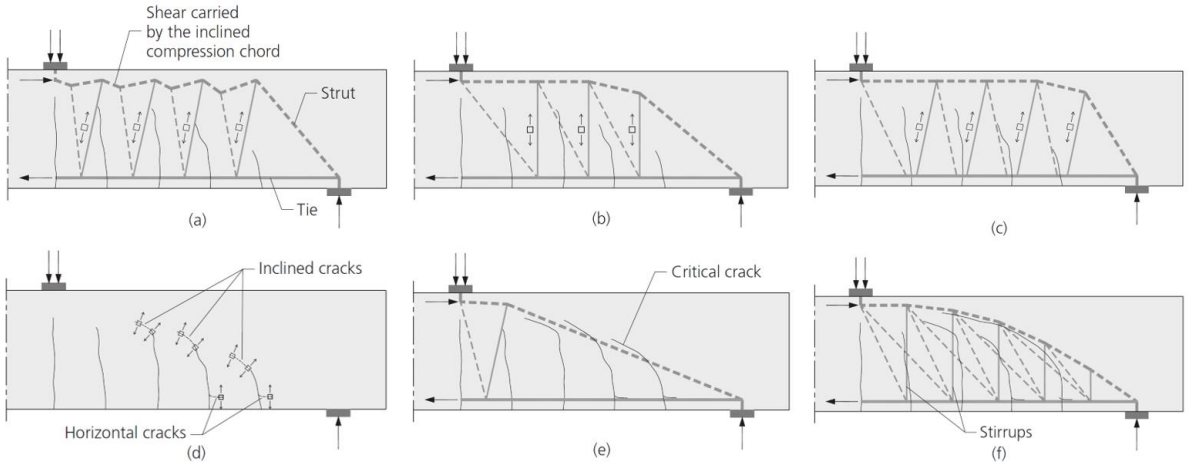

Figure 8 - Beam shear-transfer actions in cracked RC members: (a) cantilever action and inclined compression chord; (b) aggregate interlock action; (c) dowel action; (d) concrete residual tensile strength; (e) final cracking pattern and critical shear crack; (f) transverse reinforcements action. Campana et al. (2013) [2]

Table 3 – Shear transfer actions definition and notation

STA	**Description**
Inclined compression chord V_{cc}	The vertical component of the compressed chord carries shear to the support. This action can be predominant if a direct strut can form, which is the case in squat members with a shear slenderness ratio a/d<2.5.
Cantilever action V_{ca}	The cantilever action designates the development of inclined strut and ties in the uncracked concrete tooth between two flexural cracks, where the ties activate the concrete tensile strength.
Residual tensile strength of concrete V_{res}	The residual tensile strength of concrete allows tensile stress transmission through low crack openings corresponding to the fracture process zone. The corresponding strut and ties model is similar to that of the cantilever action, except that the ties can cross the tip of the cracks.
Dowel action V_D	The tensed and compressed longitudinal reinforcement can carry shear when intercepted by a crack and activated by a transversal displacement. Their capacity to transfer shear through dowel action is governed by the effective area of the concrete in tension near the bars and by its effective tensile strength.
Aggregate interlock action V_{agg}	The aggregate interlock effect allows for shear and compressive stresses through the cracks due to the roughness of the cracked concrete surface. This action, which depends mainly on the aggregate size, crack geometry and crack opening, can play a signification role in shear strength.
Shear reinforcements V_{sw}	Axial force in the stirrups.

Fernández et al. (2015) [6] demonstrated that all STA depend on the same mechanical parameters, which are the concrete compressive strength, the effective depth, the maximum aggregate size, and the crack width. Later, Cavagnis et al. (2017) [3] and Cavagnis et al. (2018) [8] observed that the amount of shear force carried by each action depends on the geometry, position, kinematics and crack roughness properties of the CSC. The research of Campana et al. (2013) [2], Cavagnis et al. (2017) [3], Cavagnis et al. (2018) [8] and Fernández (2021) [7] have led to various proposals for STA calculation models.

In the following subchapters, the STA calculation methodology followed by Monney in his PhD thesis (2022) [14] based for the most part on Cavagnis et al. (2017) [3] and adapted to include the stirrups contribution for RC members with transverse reinforcement. The following subchapters describe those calculation methods.

2.4.1 Aggregate interlock

Fernández (2021) [7] proposed an aggregate interlock model adapted for concrete members with shear reinforcements. Fernández's model describes the transfer of forces through rough cracked surfaces by combining limit analysis and material damage conditions, which avoids underestimation of the interface stresses at larger crack openings. It considers the CSC kinematics evolution and allows for a smooth transition between smeared and localised cracking conditions.

The interface stresses are the following:

$$\sigma_{agg} = -\frac{1}{2} f_{cp} \cdot \left(1 - sin\left(\frac{\pi}{2} - \alpha + \xi\right)\right) \tag{5}$$

$$\tau_{agg} = \frac{1}{2} f_{cp} \cdot cos\left(\frac{\pi}{2} - \alpha + \xi\right) \tag{6}$$

The corrected uniaxial compressive strength of concrete $f_{cp} = f_c \cdot \eta_{fc} \cdot \eta_w$ is defined as the product of the concrete cylinder compressive strength f_c, the brittleness factor $\eta_{fc} = (\frac{30}{f_c})^{1/3} \leq 1$ as per Model Code 2010 and the efficiency factor $\eta_w = 1/(1 + 100\frac{w}{d_{dg}})$ defined by Fernández (2021) [7] to account for disengagement of the aggregate at larger crack opening. The efficiency factor is function of the crack opening w and the parameter for average roughness $d_{dg} = \min(40\,mm,\ 16\,mm + d_g)$ for $f_c \leq 60\,MPa$ or $d_{dg} = \min(40\,mm,\ 16\,mm + d_g \cdot (60/f_c)^4)$ for $f_c > 60\,MPa$ considering the maximum aggregate size d_g. The relation $\tan\left(\frac{\pi}{2} - \alpha\right) = \frac{w}{\Delta}$ is valid for $\frac{\pi}{2} \geq \frac{\pi}{2} - \alpha + \xi \geq \varphi$ where α is the inclination of the crack, Δ is the crack sliding, $\varphi = 37°$ is the friction angle of concrete, $\xi = 17°$ is the dilatancy angle proposed by Fernández (2021) [7] for beams in shear.

The aggregate interlock force V_{agg} is obtained by integrating the stresses in the vertical direction along the crack length L :

$$V_{agg} = b_w \cdot \int_L (\tau_{agg} \cdot sin(\alpha) + \sigma_{agg} \cdot cos(\alpha))\, dL \tag{7}$$

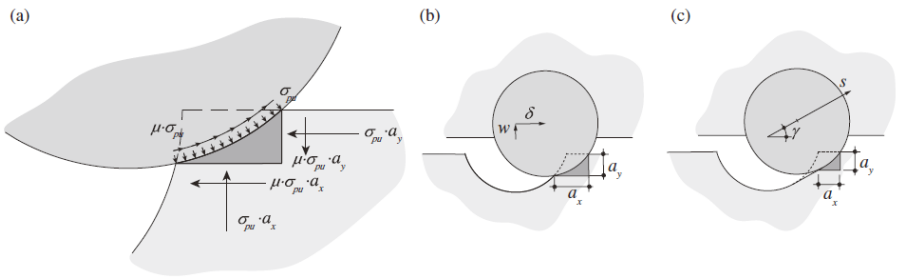

Figure 9 - Aggregate interlock contribution: (a) contact zone between aggregate and cement matrix and aggregate interlock stresses; (b, c) projections areas according to the kinematics proposed by Walraven [25] and Ulaga [23]. Cavagnis et al. (2017) [3]

2.4.2 Concrete residual tensile strength

The relation proposed by Hordijk (1992) [12] was used to calculate the force carried through concrete residual tensile strength:

$$\sigma_{res} = f_{ct} \cdot \left(\left(1 + \left(c_1 \cdot \frac{w}{w_c} \right)^3 \right) \cdot e^{-c_2 \cdot \frac{w}{w_c}} - \frac{w}{w_c} \cdot (1 + {c_1}^3) \cdot e^{-c_2} \right) \text{ for } \quad w \leq w_c \qquad (8)$$

where the tensile strength of concrete can be defined as $f_{ct} = 0.3 \cdot {f_c}^{2/3}$ for $f_c < 50\ MPa$, $w_c = 5.14 \cdot \frac{G_F}{f_{ct}}$ represents the maximum crack width for stress transfer, $c_1 = 3$ and $c_2 = 6.93$ are constants and G_F is defined according to fib Model Code 2010 : $G_F = 0.073 \cdot {f_c}^{0.18}$ $\left(\frac{N}{mm}, MPa\right)$.

The force carried through concrete residual tensile strength V_{res} is obtained by integrating σ_{res} in the vertical direction along the crack length L :

$$V_{agg} = b_w \cdot \int_L \sigma_{res} \cdot cos(\alpha)\, dL \qquad (9)$$

2.4.3 Dowel action

According to Cavagnis et al. (2017) [3], assuming that the bar is unbounded on a length of $l_{da} = l_d + d_b$ where l_d is the horizontal length affected by the dowelling crack and d_b is the diameter of the bar, the shear force carried by dowelling action for the tensed of compressed bars can be calculated by:

$$V_D = n \cdot E_s \cdot I \cdot \frac{d^3 v(x)}{dx^3} = \frac{6 \cdot n \cdot E_s \cdot I}{{l_{da}}^3} \cdot (v_0 - v_1 + \frac{l_{da}}{2}(v_0' + v_1')) \qquad (10)$$

where n is the number of bars and I is the moment of inertia of a longitudinal bar. The deflection is approximated to a third-order polynomial on the basis of the vertical displacements and rotations at the extremities of l_{da} (v_0, v_0' and v_1, v_1', see Figure 10), which are derived through the measurements of two points located in each external region at a distance $x_d = d_b/2$. This approach can be used when DIC measurements give the displacement field in the zone where the crack intercepts the flexural reinforcements.

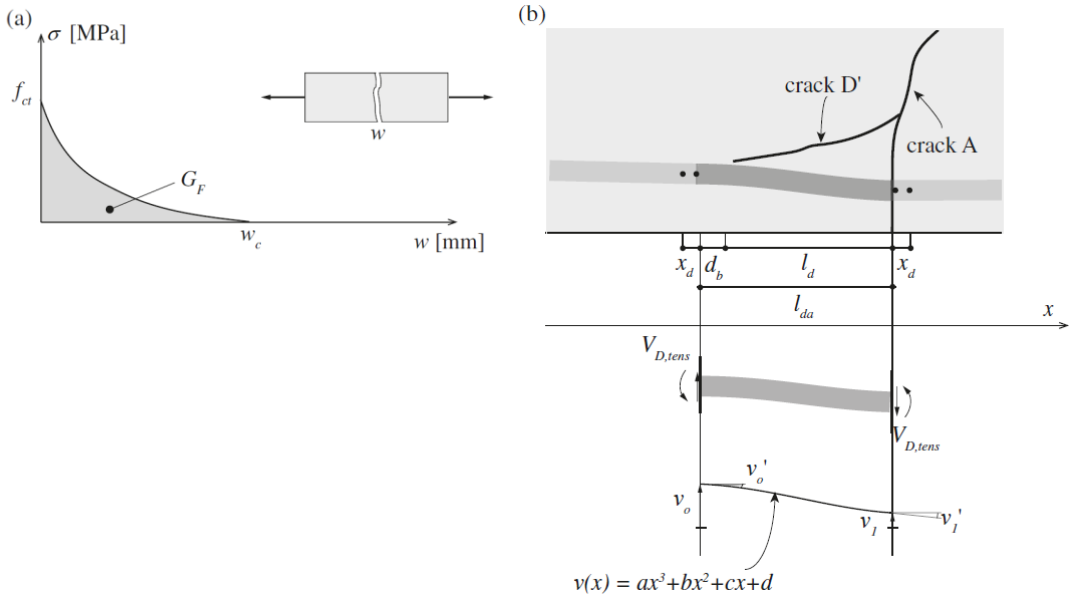

Figure 10 - (a) Tension softening of concrete under pure tensile stresses; (b) dowelling action: deflection of the flexural reinforcement in the proximity of the dowelling crack (crack type D'). Cavagnis et al. (2017) [3]

Cavagnis et al. (2018) [8] proposed a model that allow to calculate the dowel action in cases where only the crack kinematics have been measured and no DIC measurements have been performed based on an estimation of the effective area of concrete in tension near the bars and its effective tensile strength. The relation proposed to quantify dowel action is the following:

$$V_D = 2d_b k_b f_{ct} n(\frac{b}{n} - d_b) \quad (11)$$

where n is the number of bars activated, f_{ct} is the concrete tensile strength, d_b is the longitudinal bar diameter, $k_b = 0.063{\varepsilon_s}^{-1/4} \leq 1$ is a strength reduction factor that decays for increasing strains in the flexural reinforcements ε_s, that can be written as $\varepsilon_s = \frac{u_A}{d-c}$.

However, if FOM give the strain in the flexural reinforcement as it is the case for the studied specimens SM10 (see chapter §3), the internal forces of the flexural reinforcements can be directly estimated with the following formulas :

$$\chi_s = \frac{\varepsilon_{FOM,Top} - \varepsilon_{FOM,Bot}}{d_b - 2 \cdot d_{FOM}} \quad (12)$$

$$M_s = \chi_s \cdot E_s \cdot \pi \cdot \frac{{d_b}^4}{64} \quad (13)$$

$$V_s = -\frac{dM_s}{dx} \quad (14)$$

where ε_{FOM} is the strain given by the top and bottom fibres in the flexural reinforcements with diameter d_b and Young modulus E_s. The depth of the optical fibers inside the slit d_{FOM} is estimated at 1 mm for the SM10 series. The bending moment inside the flexural reinforcement M_s can be obtained with the calculated curvature χ_s and the shear force V_s is derived.

Both methods of Cavagnis et al. (2017) [3] and Cavagnis et al. (2018) [8] were compared against the FOM calculated dowel action in chapter §8.1.1.1 to determine which one is more suitable in the considered cases.

2.4.4 Compression chord

The contribution of the vertical component of the compression chord is calculated in the vertical section between the tip of the crack and the extreme compression fiber according to Cavagnis et al. (2017) [3]. The principal stresses are calculated after Kupfer as per Figure 11 from the principal strains derived using DIC measurements assuming a linear-elastic behavior of concrete before reaching its tensile strength:

$$\sigma_1 = \begin{cases} E_c \cdot \varepsilon_1, & E_c \cdot \varepsilon_1 < f_{ct} \\ 0, & E_c \cdot \varepsilon_1 \geq f_{ct} \end{cases} \quad (15)$$

$$\sigma_2 = \frac{E_c \cdot \varepsilon_2}{1 + (\frac{\varepsilon_2}{\varepsilon_0})^{\alpha}} \quad (16)$$

with:

$$\varepsilon_0 = \frac{\alpha \cdot f_{c,eff}}{E_c \cdot (\alpha - 1)^{(1 - \frac{1}{\alpha})}} \quad (17)$$

$$\alpha = 0.5 + \frac{f_{c,eff}}{20} + \frac{{f_{c,eff}}^2}{1500} \quad (18)$$

where ε_2 is the principal compressive strain, $E_c = 10000 \cdot {f_c}^{1/3}$ and $f_{c,eff} = f_c/(0.8 + 170 \cdot \varepsilon_1) \leq f_c$ is the effective compressive strength of concrete in MPa proposed by Vecchio and Collins (1986) [24].

The force carried through concrete by the arching action V_{cc} is obtained by integrating the projection of the principal stresses σ_1 and σ_2 in the vertical direction along the crack.

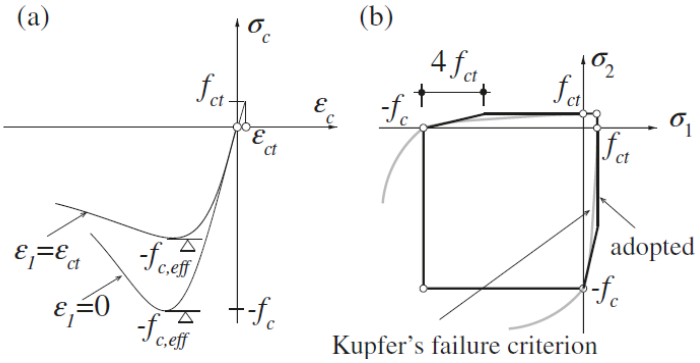

Figure 11 - (a) Adopted stress–strain diagram for concrete; (b) Kupfer's failure surface and the adopted one. Cavagnis et al. (2017) [3]

2.4.5 Cantilever action

This action was deemed negligible and is not considered in the model proposed by Cavagnis et al. (2017) [3]. It can be governing for load levels lower than the actual failure load but is disabled by the development of the quasi-horizontal branch of the CSC. (Cavagnis et al. (2018) [8])

2.4.6 Shear reinforcements

The stirrups are activated by the opening of the cracks intersecting them. Campana et al. (2013) [2] propose to assume a rigid-plastic bond at the stirrups interface. It follows that all tension force is carried in the shear reinforcements at the crack and decreases linearly by stress transmission to the concrete in the bounded regions, as per Figure 12. The bound stress is assumed to be constant at $\tau_{b0} = 2f_{ct}$ before yielding and $\tau_{b1} = f_{ct}$ after that, where $f_{ct} = 0.3 \cdot f_c^{2/3}$is the concrete tensile strength. This bound stress assumption was used by Marti et al. (1998) [13] for their proposed tension chord model.

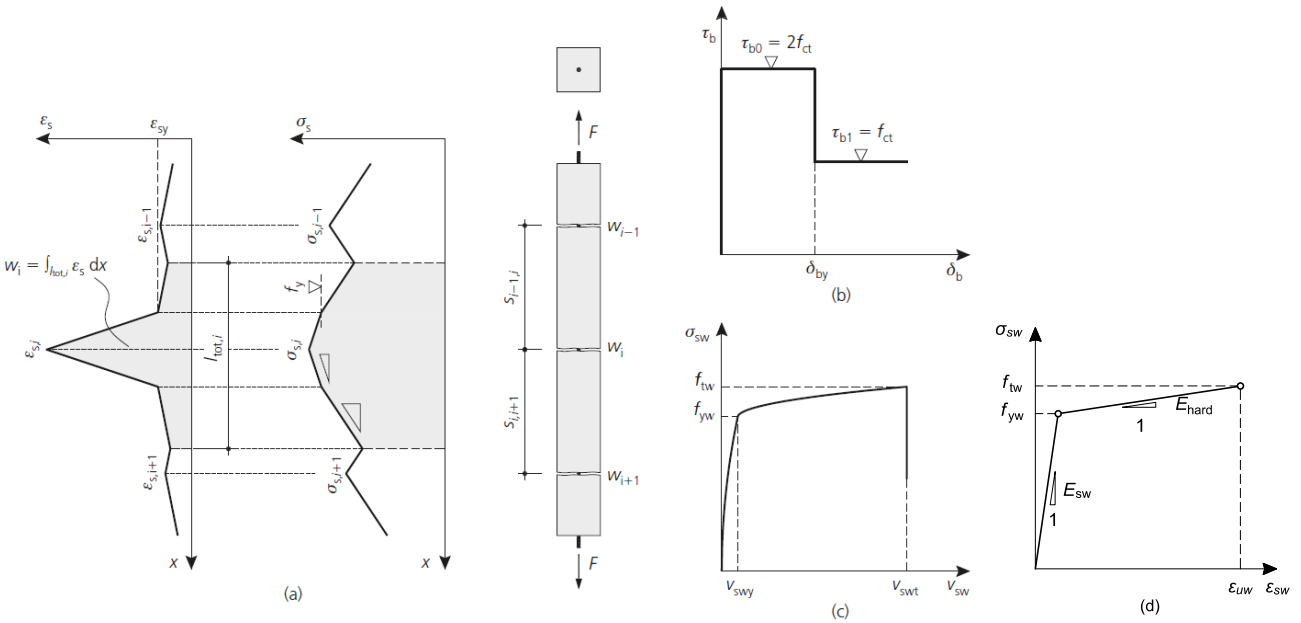

Figure 12 - Transverse reinforcement contribution. (a) Relationship between cracks opening and steel strain and stresses in a RC tie. (b) Assumed rigid–plastic bond behaviour. (c) Behaviour of an embedded (bonded) vertical stirrup. (d) Bilinear stress-strain law considered for the stirrup. Campana et al. (2013) [2]

The crack opening can be obtained by neglecting the concrete strains and integrating the steel strains $w_i = \int_{ltot,i} \varepsilon_s \, dx$ as illustrated in Figure 13. Monney (2022) [14] calculated the stress of each stirrup at the location of the crack σ_{sw} based on Campana et al. (2013) [2] considering the bilinear stress-strain law Figure 12 (d). This same law is also used to obtain the stress from FOM. The interaction effect of two close cracks on the bound stress distribution in cases of cracks intersecting the same stirrups was taken in account.

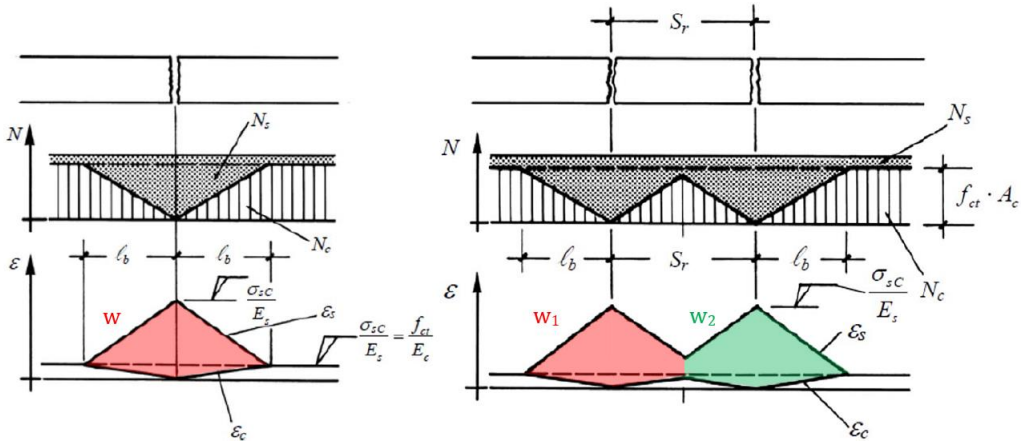

Figure 13 - Distribution of traction force and strains of the reinforcement and concrete in the cracked zone. Situation with crack without (left) and with (right) interaction between two cracks. Muttoni & Fernández, polycopié "Structures en béton" [15]

The force carried through shear reinforcements is defined by Campana et al. (2013) [2] as follows:

$$V_{sw} = \sum_{i=1}^{n} V_{sw,i} = \sum_{i=1}^{n} \frac{\sigma_{sw,i} \cdot \pi \cdot d_{sw,i}^{\,2}}{4} \tag{19}$$

where d_{sw} is the diameter of the stirrup, and n is the number of stirrups activated by the crack.

The shear reinforcements activated by the dowel action of the flexural reinforcement are not considered in the calculation of the stirrups action. Their effect is already considered in the dowel action in chapter §2.4.3.

Marti et al. (1998) [13] proposed a model to represent the behaviour of a tension chord under a monotonically increasing load. The strain distribution between two cracks can be determined assuming maximum steel strain ε_s at the cracks.
The crack spacing s_{rm} is limited in a fully developed crack pattern by the range $0.5 \leq \lambda \leq 1$.

$$s_{rm} = \lambda \cdot s_{rm0} \tag{20}$$

$$\text{where } s_{rm0} = \frac{d_b \cdot f_{ct} \cdot (1-\rho)}{2 \cdot \tau_{b0} \cdot \rho} \tag{21}$$

$$\text{and } \tau_{b0} = 2 \cdot f_{ct} \text{ before yielding and } \tau_{b0} = f_{ct} \text{ after.} \tag{22}$$

After concrete cracking, the steel stresses at the location of the crack jump from $f_{ct} \cdot \frac{E_s}{E_c}$ to:

$$\sigma_{sr0} = f_{ct} \cdot \left(\frac{1}{\rho} + \frac{E_s}{E_c} - 1\right) \tag{23}$$

For $\sigma_{sr} > \sigma_{sr0}$, the crack opening is:

$$w = \frac{\lambda \cdot s_{rm0} (2 \cdot \sigma_{sr} - \lambda \cdot \sigma_{sr0})}{2 \cdot E_s} \tag{24}$$

To use Marti's model on the stirrups of the SM10 series, an equivalent reinforcement ratio must be calculated. Galkovski et al. (2022) [9] proposed a method to obtain the equivalent reinforcement ratio based on the Compatible Stress Field Method (CSFM). The CSFM is a simplified nonlinear finite element-based continuous stress field analysis. The concrete tensile strength is neglected with the exception of tension stiffening. Simple uniaxial constitutive laws illustrated in Figure 14 a) are implemented for concrete and reinforcement. To determine the effective concrete area $A_{c,eff}$ for each reinforcement bar, a circle corresponding to the concrete area that can be activated at f_{ct} in the extreme case of $\sigma_s = f_t$ is drawn (Figure 14 b) step (i)) with diameter:

$$Ø_{c,eff} = d_b \cdot \sqrt{f_t / f_{ct}} \tag{25}$$

Symmetry conditions are then applied as per Figure 14 b) step (ii) following Frantz & Breen (1978) [11] to only consider twice the distance of the concrete surface to the bar's centroid as the concrete area acting in tension. Indeed, Frantz & Breen (1978) [11] found crack width in beam webs to be independent of the web width but proportional to the concrete cover of axial reinforcements. If the resulting areas overlap between adjacent bars, the intersection surfaces are attributed to the closest bar as per Figure 14 b) step (iii). Finally, identical crack spacing is imposed for proximate parallel reinforcement defined with a spacing $\leq$ 100mm. Proximate bars are therefore assigned an identical ratio of $Ø(1 - \rho_{eff})/\rho_{eff} \approx Ø/\rho_{eff}$. The effective concrete area in tension for a bar i in a proximity group of j bars is:

$$A_{c,eff,i} = A_{c,eff,tot} \frac{d_{b,i}}{\sum_1^j d_{b,j}} \tag{26}$$

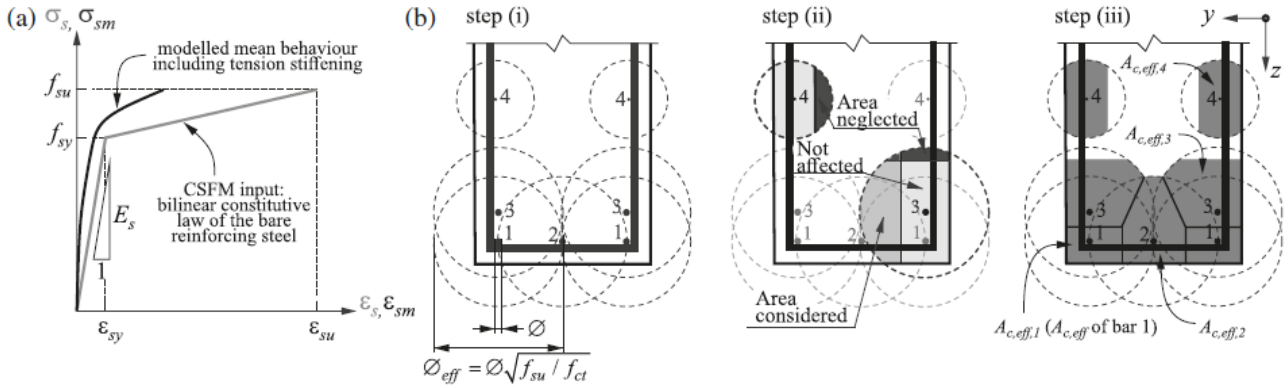

Figure 14 - Implementation of tension stiffening in CSFM: (a) implemented increased stiffness of the bonded bar; (b) determination of $A_{c,eff}$ (stabilized cracking): (i) maximum concrete area that can be activated per bar; (ii) local symmetry condition; (iii) global geometry condition and resultant effective concrete areas. Galkovski et al. (2022) [9]

Once the effective concrete area in tension defined for each bar, the effective reinforcement ratio that can be used in Marti's approach becomes:

$$\rho_{eff} = \frac{\pi \cdot {d_b}^2}{4 \cdot A_{c,eff}} \tag{27}$$

Both methods of Monney (2022) [14] and Marti et al. (1998) [13] applied with the effective reinforcement ratio according to Galkovski et al. (2022) [9] were compared against the FOM calculated stirrups stress in chapter §8.1.1.2 to determine which one is more suitable in the considered cases.

3 Description of the studied laboratory tests

The laboratory measurements used in the present study were conducted at EPFL by Frédéric Monney as part of his PhD thesis in 2022 [14]. The SM10 test series was used for research, whereas SM00 test series served as validation set. The full details of those experimental test series can be found in chapter 4.2 and 4.3 of Frédéric Monney's thesis [14]. Only the main information relevant to the present study is presented here.

3.1 Main set: SM10 series

Six loading tests were performed on three beams with identical shear span $a = 2600\,mm$ and height $h = 700\,mm$ with effective depth $d = 650\,mm$. The specimens have variable width and shear reinforcement ratios. Their complete parameters are featured in Table 4. SM10 specimens were cast from the same normal strength concrete with a water-to-cement ratio of 0.5 and 300 kg/m^3 of cement content with a maximum aggregate size of 16 mm.

Table 4 – Main parameters and experimental results of SM10 series (for definition of parameters, refer to Notation section). Monney (2022) [14]

Specimen	Shear reinf. ductility class[1)]	b_w	ρ_w	f_c	f_{ct}	f_{yw}	f_{tw}	ε_{uw}	V_{max}[2)]	τ_{max}[3)]
		[mm]	[%]	[MPa]	[MPa]	[MPa]	[MPa]	[%]	[kN]	[MPa]
SM11	A	800	0.063	50.7	3.2	505	549	3.1	603	1.16
SM12	C	800	0.063	50.6	3.2	538	641	9.0	610	1.17
SM13	A	600	0.084	50.4	3.2	505	549	3.1	540	1.38
SM14	C	600	0.084	50.4	3.1	538	641	9.0	639	1.64
SM15	A	500	0.101	50.2	3.1	505	549	3.1	454	1.40
SM16	C	500	0.101	50.0	3.1	538	641	9.0	515	1.58

[1)] according to [Eur04]

[2)] measured shear strength without the self-weight

[3)] $\tau_{max} = V_{max}/(b_w \cdot d)$

The shear reinforcements are made of Ø8mm stirrups of steel type B500 with a ductility type A or C depending on the specimen as per Table 4. The flexural reinforcement consisted of high strength Y1050 steel and B500B steel. The stress-strain curves for every type of steel used is found in Figure 15. The flexural reinforcement did not yield at ultimate load for this test series.

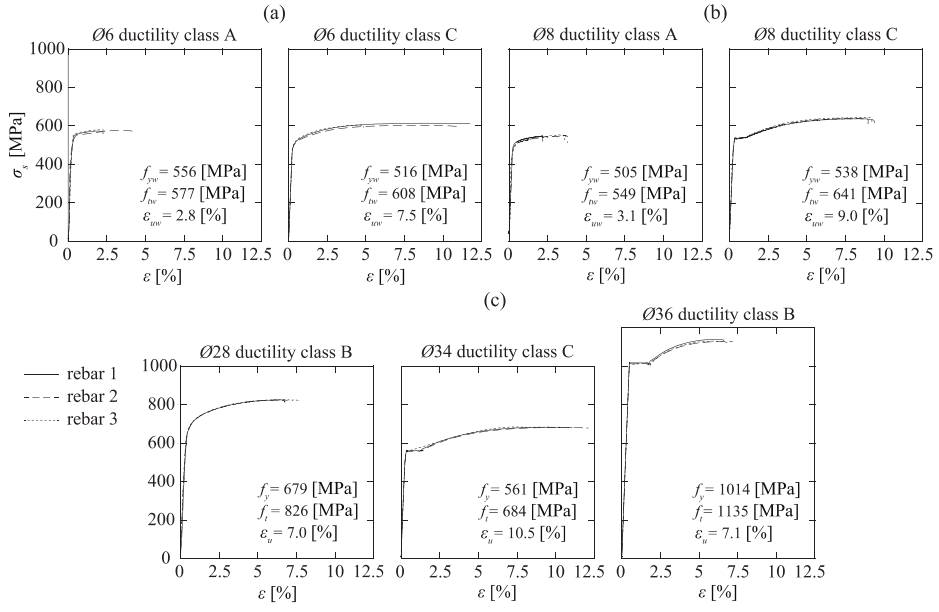

Figure 15 - Stress-strain curves for: (a) shear reinforcement bars of series SM00; (b) shear reinforcement bars of series SM10; and (c) flexural reinforcement bars of series SM00 and SM10. Monney (2022) [14]

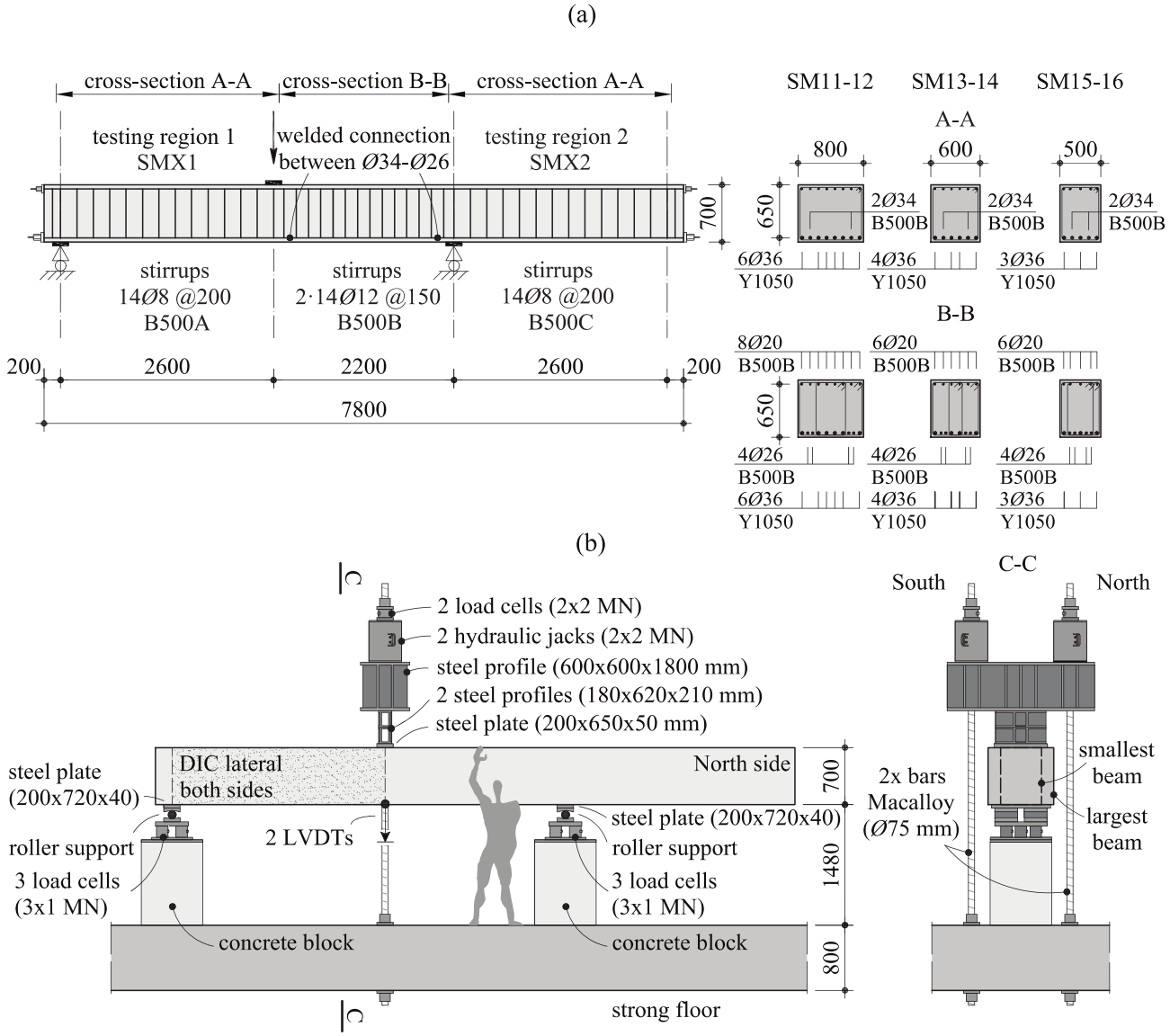

Figure 16 – Geometry with reinforcement layouts (a) and test set-up (b) of the SM10 specimens. Monney (2022) [14]

The test set-up and specimen geometry and reinforcement layout are shown in Figure 16. The beams were flipped over after the loading of one end to test the other one.

The force at each bearing support and hydraulic jacks was measured by load cells. Two linear variable differential transformer (LVDT) sensors placed under the hydraulic jacks measured the deflection of the beam. DIC measurements were performed on both lateral surfaces of the left span of the beam as shown in Figure 16. The mean DIC measurement error considered for all six specimens has been set at $err_{DIC} = 0.01\ mm$.

Fibre-Optical Measurement (FOM) were also performed on flexural reinforcement and selected stirrups. The positioning of the instruments used for FOM measurements is depicted in Figure 17. FOM allows for very detailed measurements of axial strains in the reinforcements.

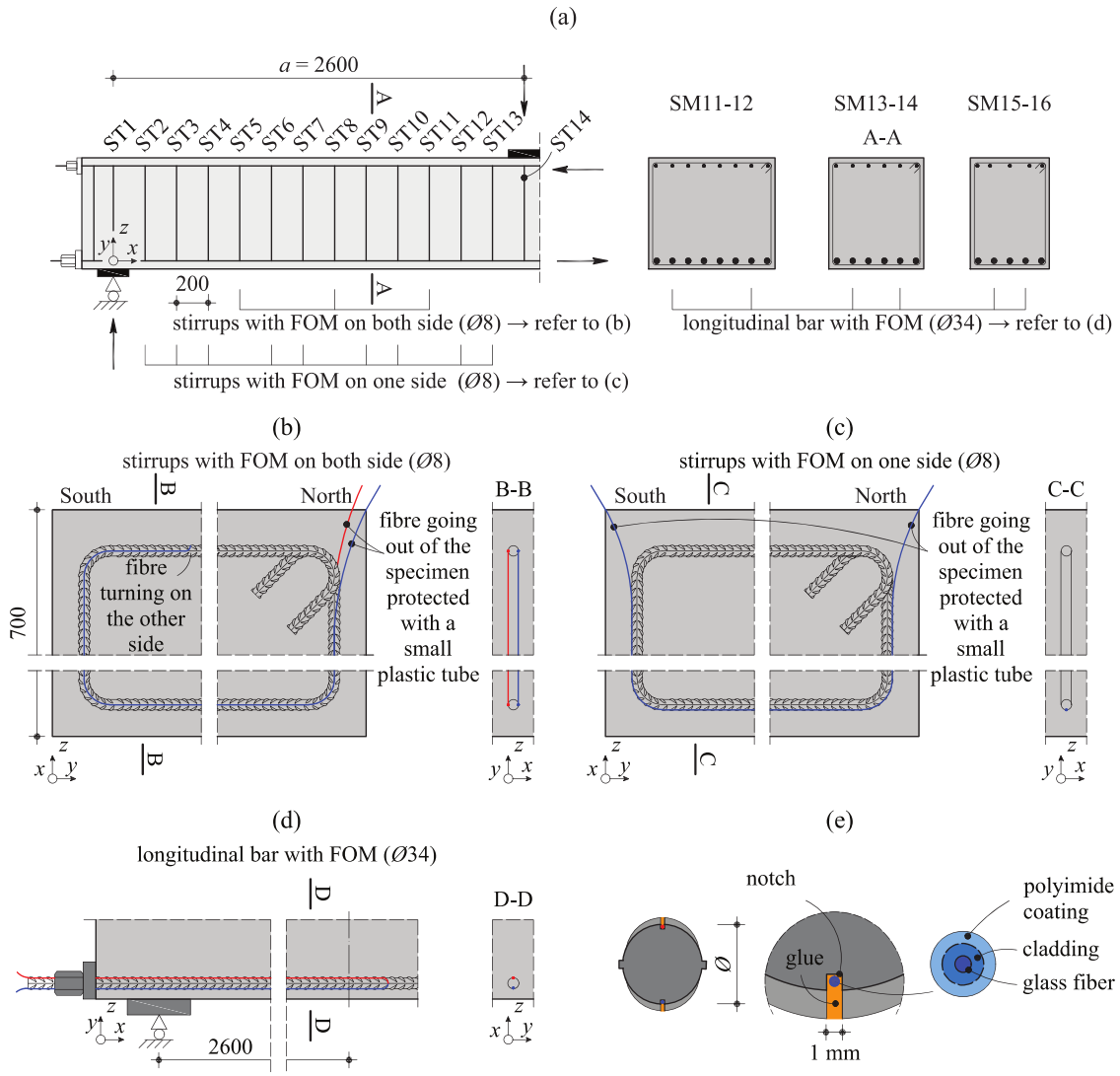

Figure 17 – Fibre-Optical Measurement: a) instrumented bars; b) positions on the strirrups with two fibres; c) position on the stirrups with one fibre; d) position on the flexural reinforcement; e) detail of installation. Monney (2022) [14]

3.2 Validation set: SM00 series

Four simply supported three-point bending tests were performed on beams with identical shear span $a = 1800\,mm$, width $b_w = 250\,mm$ height $h = 600\,mm$ with effective depth $d = 550\,mm$. The SM00 specimens have identical shear reinforcement ratios. Their complete parameters are featured in Table 5. The SM00 specimens were cast from the same normal strength concrete with a water-to-cement ratio of 0.65 and 308 kg/m³ of cement content and a maximum aggregate size of 16 mm.

Table 5 – Main parameters and experimental results of SM00 series (for definition of parameters, refer to Notation section). Monney (2022) [14]

Specimen	Shear reinf. anchorage	Shear reinf. ductility class[1)]	ρ_w [%]	f_c [MPa]	f_{ct} [MPa]	f_{yw} [MPa]	f_{tw} [MPa]	ε_{uw} [%]	V_{max}[2)] [kN]	τ_{max}[3)] [MPa]
SM01	Head	A	0.113	40.4	2.1	556	577	2.8	235	1.71
SM02	Head	C	0.113	40.5	2.1	516	608	7.5	286	2.08
SM03	Bend	A	0.113	40.6	2.2	556	577	2.8	235	1.71
SM04	Bend	C	0.113	40.6	2.2	516	608	7.5	269	1.96

[1)] according to [Eur04]

[2)] measured shear strength without self-weight

[3)] $\tau_{max} = V_{max}/(b_w \cdot d)$

The shear reinforcements are made of one-leg links Ø6mm of steel type B500 with a ductility type A or C depending on the specimen as per Table 5. The anchorages consisted of headed bars (SM01 and SM02) and links with short bends (SM03 and SM04).

The tensed flexural reinforcement consisted of Ø28mm S670 high strength steel, and the compressed ones of Ø16mm B500B steel. The stress-strain curves for every type of steel used is displayed in Figure 15. The test set-up and specimen geometry and reinforcement layout are shown in Figure 18.

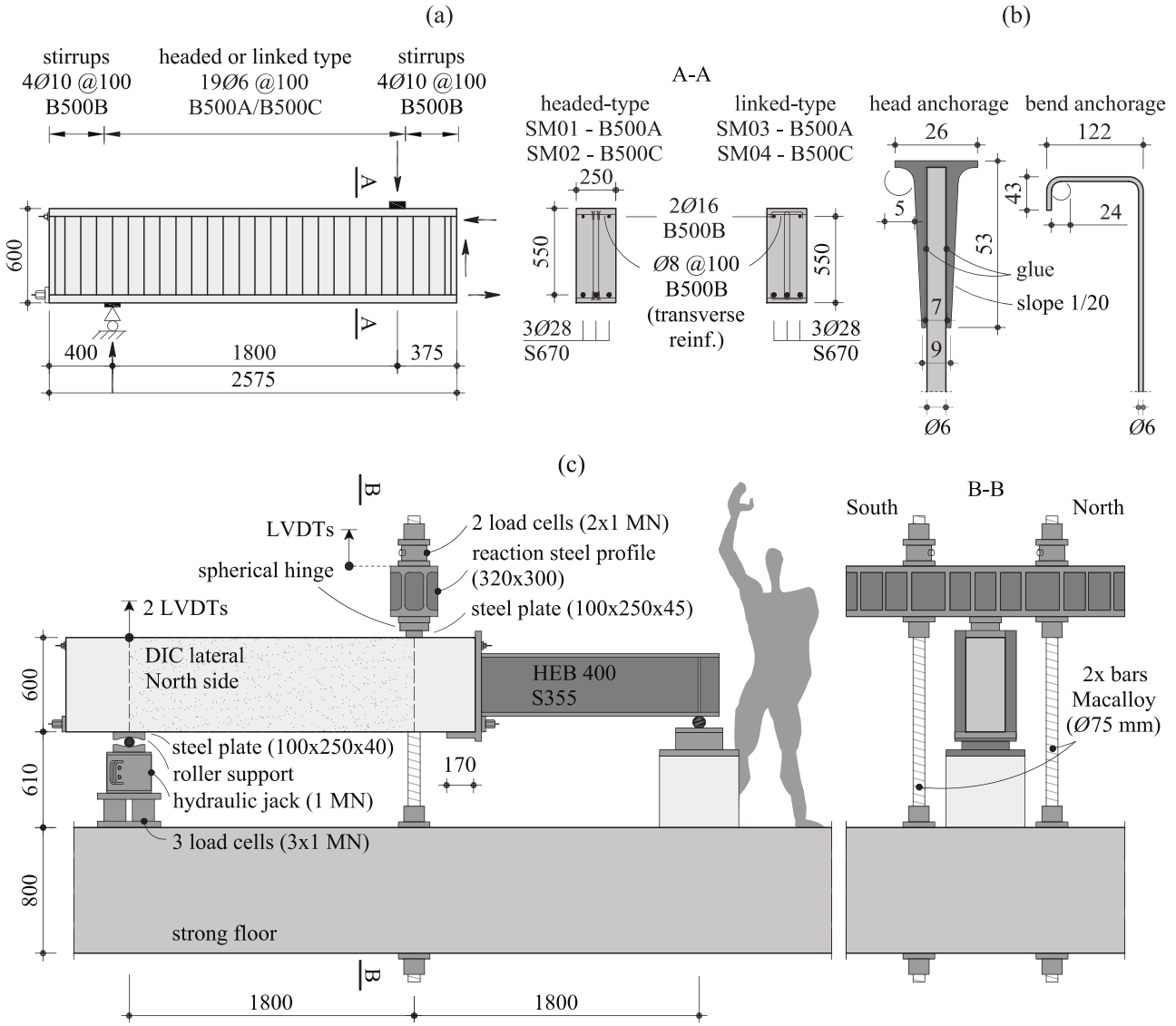

Figure 18 – Geometry with reinforcement layouts (a), shear anchorage detail (b) and test set-up (c) of the SM00 specimens. Monney (2022) [14]

The force at the hydraulic jacks and at midspan was measured by load cells. LVDT sensors placed at the hydraulic jack and at the reaction steel profile measured the deflection of the beam. DIC measurements were performed on both lateral surfaces of the left span of the beam as shown in Figure 18.

4 Cracking pattern development of the SM10 specimens

The cracks of the SM10 specimens first appear as the cracking bending moment is reached with primary (type A) and secondary (type B) flexural cracks developing quasi-vertically in a relatively regular spacing, forming Kani's teeth.

Specimens SM11 and SM12 (Figure 19) with the lowest shear reinforcement ratio $\rho_w = 0.063\%$ experienced a brutal rupture of the top of Kani's teeth at a load level very close to the ultimate load ($\geq 95\%\ V_{max}$). A type C secondary flexural crack induces failure of the specimens by joining the developping quasi-horizontal portion CSC. This corresponds to a CCDT4 according to Cavagnis et al. (2017) [3] (see chapter §2.1). The failure surface formed by the junction of the quasi-horizontal part of the CSC and the remaining Kani's tooth is relatively flat for those specimens, especially for SM11 with a stirrups ductility class A, which indicates brittle failure. Specimens SM11 and SM12 behaved in a similar fashion as concrete members without transverse reinforcements, with strains mainly localised in a single failure crack.

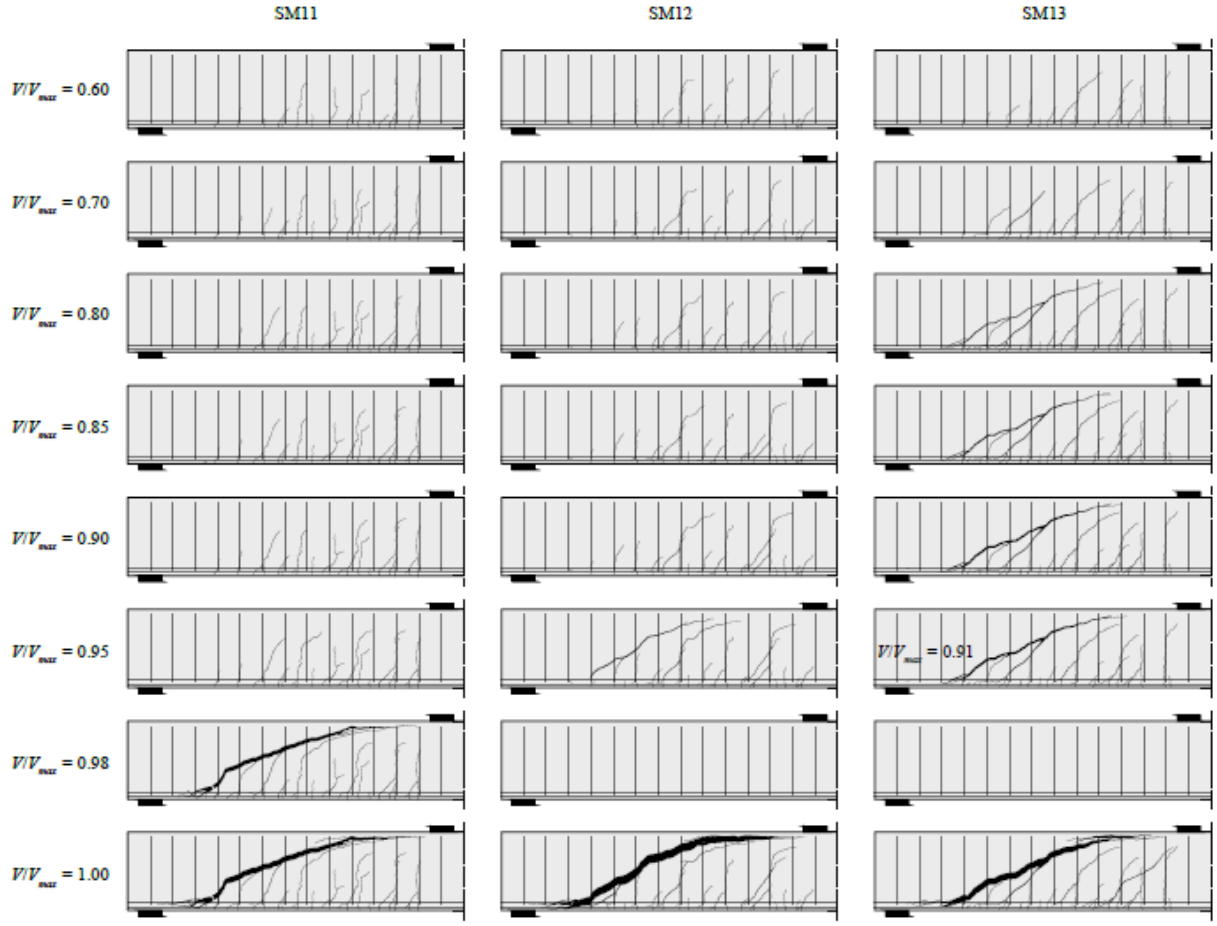

Figure 19 – Specimens SM11, SM12 and SM13 North: development of the cracking pattern along the load. Monney (2022) [14]

Specimens SM13 and SM14 (Figure 19 and Figure 20) with a medium shear reinforcement ratio $\rho_w = 0.084\%$ presented a CCDT2 according to Cavagnis et al. (2017) [3] (see chapter §2.1) with a secondary flexural crack type C joining the CSC around $70\%V_{max}$ and ultimately forming the failure surface. SM13 with stirrups ductility class A showed more localised strains in a single crack, whereas relatively large crack openings have also been detected in secondary cracks of SM14 with stirrups ductility class C. The failure surface is still relatively flat.

Specimens SM15 and SM16 (Figure 20) with the highest shear reinforcement ratio $\rho_w = 0.101\%$ presented a more distributed crack pattern than the other specimens, in particular for SM16 with a shear reinforcement ductility class C where three major cracks formed as well as secondary cracks at a rotated angle from the original cracks. Indeed, when the crack opening is kept low by sufficient shear reinforcement, high contact forces can develop between the rough crack lips, allowing for the development of secondary such cracking. (Fernández (2021) [7]) Specimen SM16 presented a CCDT2 or CCDT3 according to Cavagnis et al. (2017) [3] (see chapter §2.1) where a stable propagation of the CSC from a primary flexural crack type A was observed. It is unclear whether the quasi-horizontal portion of the crack corresponds to a type F or type E' crack. For specimen SM15, a CCDT2 is observed with a secondary flexural crack type C joining the stably propagating CSC and ultimately forming the failure surface. The failure surfaces adopted a more curved shape than those of the lower shear reinforcement ratios specimens, especially for SM16 with stirrups ductility class C.

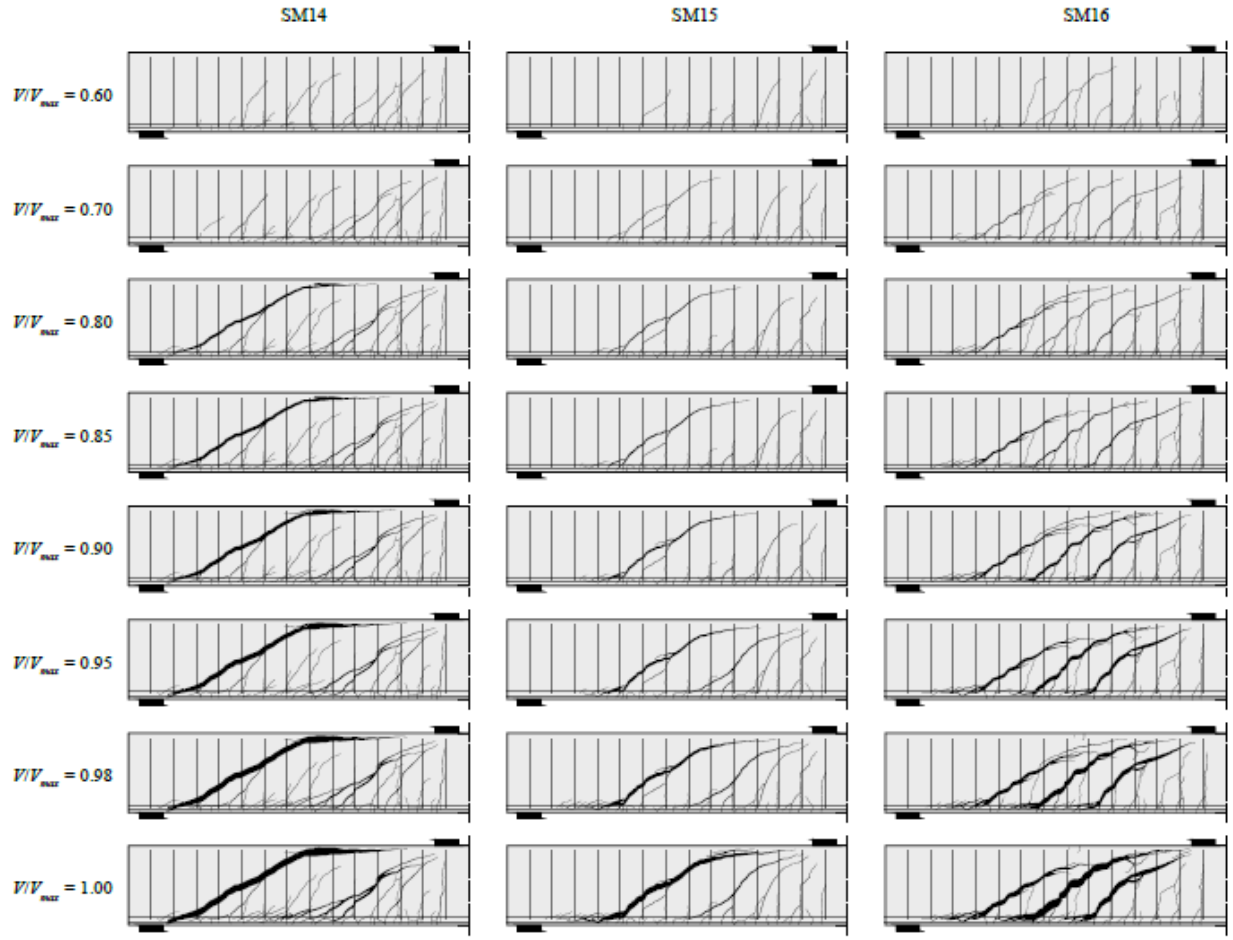

Figure 20 – Specimens SM14, SM15 and SM16 North: development of the cracking pattern along the load. Monney (2022) [14]

In all cases, the failure surface developed through the theoretical compression strut between the load and the support as observed by Cavagnis et al. (2017) [3] for RC members with a shear span ratio $\frac{a}{d} > 2.5$.

The SM10 specimens present a relatively brittle behaviour due to their low shear reinforcement ratio. Indeed, SM15 and SM16 attain the minimum shear reinforcement ratio of $\rho_w = 0.1\%$ recommended by SIA 262 standards (2013), but the other specimen are under-reinforced in shear. For those specimens, strains tends to localize in a single crack and cause brutal failure by disengagement of the crack lips, whereas the cracks would developp in a more controlled manner with sufficient shear reinforcement ratio. Smaller crack openings lead to an increased ability to transfer shear through aggregate interlock and concrete residual tensile strenght. (Fernández (2021) [7])

The shear reinforcement ratio had an impact on the measured ultimate load, as shown in Table 6. The ultimate load normalized by the beams width $V_{max,actual}/b_w$ tends to be higher for larger shear reinforcement ratio, except for SM14 that has the highest normalized ultimate load. This is probably due to statistical variability. The same trend is observed for the displacement capacity δ.

The importance of the ductility class of the shear reinforcement is also highlighted by the identified differences between specimens with class A stirrups and their class C twin. Specimens with class C stirrups consistently had a higher normalized ultimate load and displacement capacity than their their class A twin, highlighting the importance of the steel's ductility class.

Table 6 – SM10 specimens varying parameters and measured maximal shear force $V_{max,actual}$

Specimen	SM11	SM12	SM13	SM14	SM15	SM16
Shear reinforcement ductility class	A	C	A	C	A	C
Shear reinforcement ratio ρ_w	0.063 %	0.063 %	0.084 %	0.084 %	0.101 %	0.101 %
Width b_w [mm]	800	800	600	600	500	500
Measured maximal shear force [kN] $V_{max,actual}$	605	597	542	644	457	518
$V_{max,actual}/b_w$ [kN/m]	756	746	903	1073	914	1036

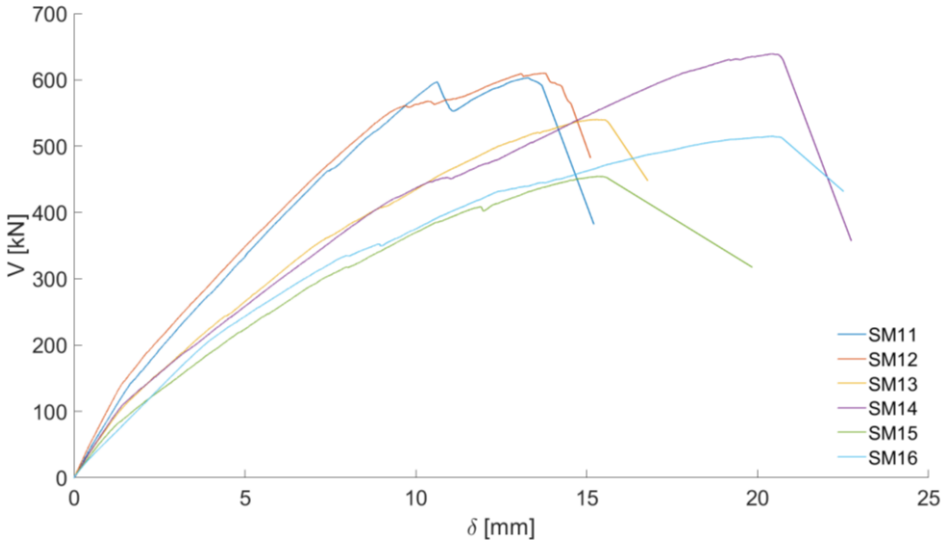

Figure 21 – Load-deflection curves for SM10 specimens. The shear force V is measured at the left support and the deflection under the hydraulic jack (see Figure 16)

5 Critical shear crack geometry prediction

A bilinear approximation is proposed to predict the geometry of the failure surface, which will be useful for the kinematics predictions of chapter §7. This method is different than the one presented by Hugo Nick in his Master thesis (2023) [17] as it allows for geometric predictions at earlier stages of the crack development, with a trade-off on precision.

The angle of the quasi-vertical part of the crack α_1 is estimated as the average angle of the crack in its initial state as per equation (28).

$$\alpha_1 = mean(\overline{\alpha_{init}}) \tag{28}$$

The quasi-horizontal part of the crack generally does not develop before around 70% of the maximum load. In order to predict the evolution of a crack still located in its quasi-vertical stage, two conditions are set.

The first condition is the position of the point where the slope changes, called "bilinear point" in what follows. The bilinear point is placed at the height of the neutral axis calculated by neglecting concrete in tension and assuming a linear response of concrete in compression according to Cavagnis et al. (2018) [8] and illustrated in Figure 22.

$$c = d \cdot \rho \cdot \frac{E_s}{E_c}\left(\sqrt{1 + \frac{2 \cdot E_c}{\rho \cdot E_s}} - 1\right) \tag{29}$$

$$Y_{bilinear} = h - c \tag{30}$$

The x-coordinate of the bilinear point $X_{bilinear}$ is obtained by extending the quasi-vertical crack portion with angle α_1 up to the y-coordinate of the bilinear point.

The second condition places the quasi-horizontal crack portion on a line linking the bilinear point and a point located on the top flexural reinforcement under the edge of the loading plate, approximately where the tip of the failure surface was located after ultimate load on the SM10 specimens. This point would not always be clearly identifiable in practice, especially if the point load is an axle whose position varies over time. The angle of the quasi-horizontal crack portion α_2 is thus estimated as per equation (31).

$$\alpha_2 = actan\left(\frac{h - d_{top} - Y_{bilinear}}{x_{endplate} - X_{bilinear}}\right) \tag{31}$$

The angle $\beta_{BF} = \frac{\pi}{8}$ of the quasi-horizontal segment and its length $l_F = \frac{d}{6}$ proposed by Cavagnis et al. (2018) [8] for the bilinear approximation of the CSC could have been used to simplify the bilinear approximation but those values do not apply well on the SM10 series.

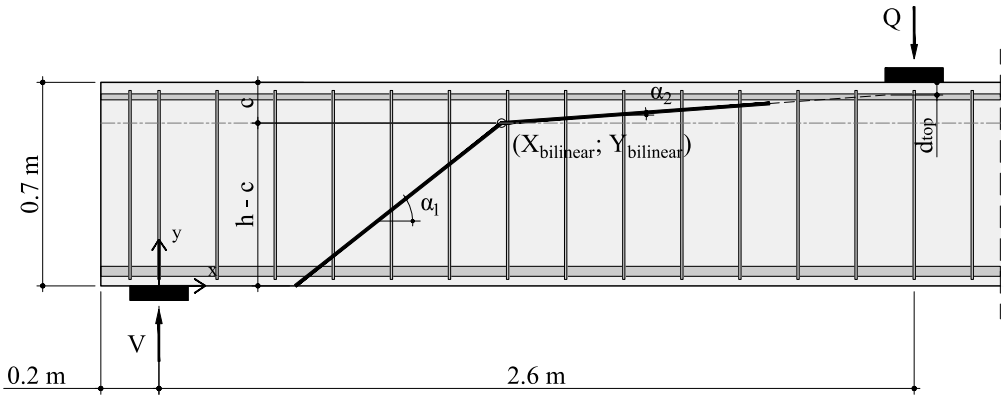

Figure 22 - Bilinear crack approximation

Figure 23 shows the bilinear approximation that will be used for the geometric predictions of the failure surface on two specimens. It gives a rough approximation of the trend followed by the actual crack angle.

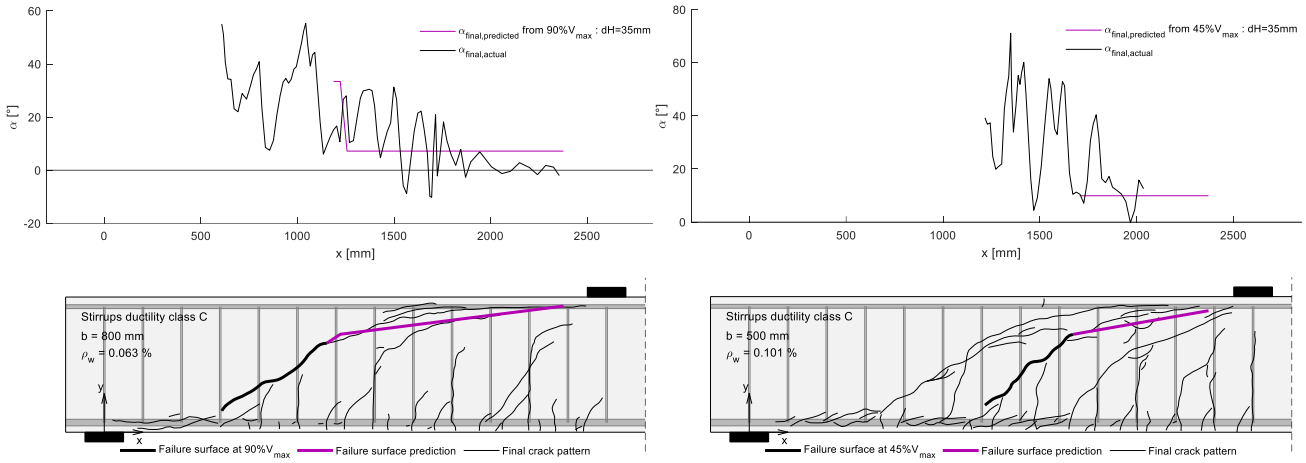

Figure 23 - SM12 North (left) and SM16 North (right): actual and predicted CSC horizontal angle with $Y_{bilinear} = h - c$ hypothesis

6 Crack propagation depending on load level

In the present report, the point considered as the propagating tip of the failure surface $(x_{tip};\ y_{tip})$ is defined at different load levels as the last point where the crack opening w is greater than the DIC error chosen as $err_{DIC} = 0.01\ mm$ for the SM10 series.

$$w_{tip} \geq err_{DIC} \tag{32}$$

The crack tip propagation of the failure crack was studied as a function of the load level. The initial load level considered for each specimen are listed in Table 7. They differ between specimens due to failure surface development closer to failure for specimens with lower transversal reinforcement ratios than for those with higher ratios.

Table 7 – Initial load level considered for each specimen

Specimen	SM11	SM12	SM13	SM14	SM15	SM16
Initial load level considered	90% V_{max}	90% V_{max}	55% V_{max}	55% V_{max}	45% V_{max}	45% V_{max}

In an attempt to find a common trend between the specimens, the crack tip propagation has been studied in the following chapters §6.1 and §6.2 in both x and y directions respectively. The propagation has been represented as a function of the load level and as a function of the ratio of the bending moment calculated in the section located at the crack tip M_{tip} (33) to the cracking moment $M_{cracking}$ (34). The objective was to evaluate the possibility of predicting the load-propagation relationship from known initial position and load level for a measured shear crack.

$$M_{tip} = V \cdot x_{tip} \tag{33}$$

$$M_{cracking} = f_{ct} \cdot \frac{b \cdot h^2}{6} \tag{34}$$

6.1 Crack tip propagation in the horizontal x-direction

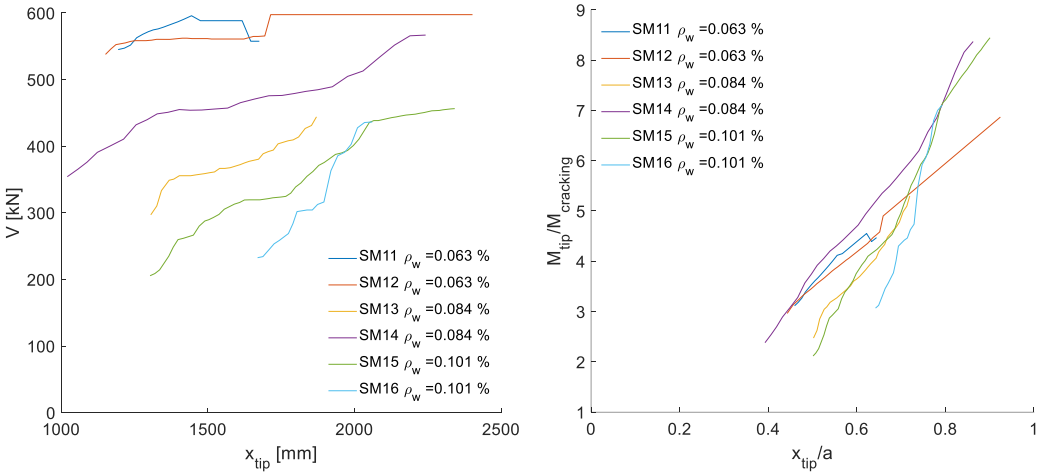

Figure 24 – SM10 North face : actual x-coordinate of the crack tip x_{tip} as a function of the shear force V (left) and actual x-coordinate of the crack tip x_{tip} over the shear span a of the ratio of the bending moment at the crack tip M_{tip} to the cracking moment $M_{cracking}$ (right).

The ratio of the bending moment calculated in the section located at the crack tip M_{tip} to the cracking moment $M_{cracking}$ has been represented as a function of the crack tip x_{tip} in Figure 24, normalized over the shear span a to make it adaptable to other beam configurations. It follows an approximately linear relation that has been expressed in equation (35). An experimental approximation depending on the square of the shear reinforcement ratio was used to determine the slope a_1, and the initial load and crack tip position gave the y-intercept b_1.

$$\frac{M_{tip}}{M_{cracking}} = a_1 \frac{x_{tip}}{a} + b_1 \qquad (35)$$

with $a_1 \cong 2.1 \cdot 10^7 \cdot {\rho_w}^2$ and using initial conditions $b_1 = \frac{x_{tip,init} \cdot V_{init}}{M_{cracking}} - a_1 \cdot \frac{x_{tip,init}}{a}$

The relation (35) fitted on SM10 results was in a second phase tested on the validation set SM00 (Figure 25). It follows that an approximately linear relationship is also observed for the SM00 test set. However, the fitted linear relationships only offer a smoothed estimate of the actual propagation and is very dependent on the initial position of the crack tip which is subjected to the high local and global geometric variability of cracks. Moreover, since these observations are based on RC beams with shear reinforcements transversely loaded by a fixed-point force, it is possible that the validity of relation (35) is limited to the specific experimental conditions of SM10 and SM00 series.

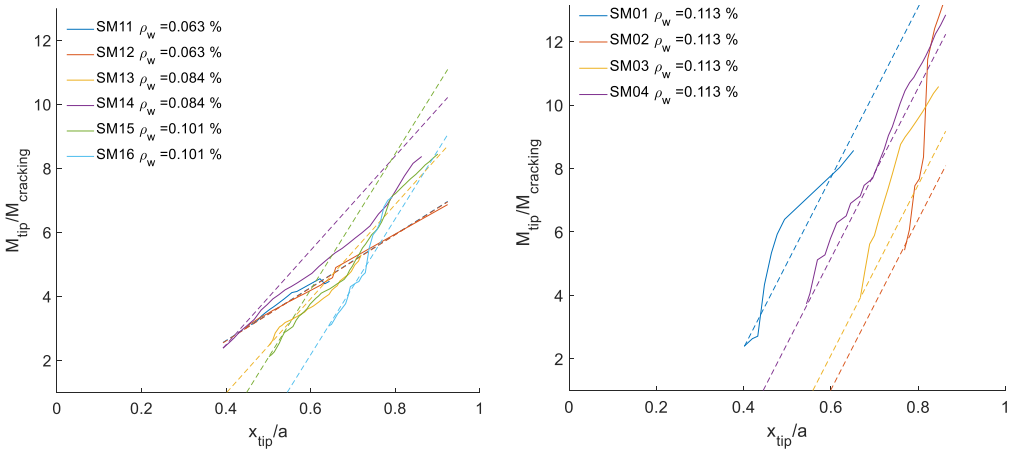

Figure 25 - North face SM10 (left) and SM00 (right) : actual x-coordinate of the crack tip as a function of the ratio of the bending moment at the crack tip M to the cracking moment $M_{cracking}$ with fitted experimental linear relation (dashed).

6.2 Crack tip propagation in the vertical y-direction

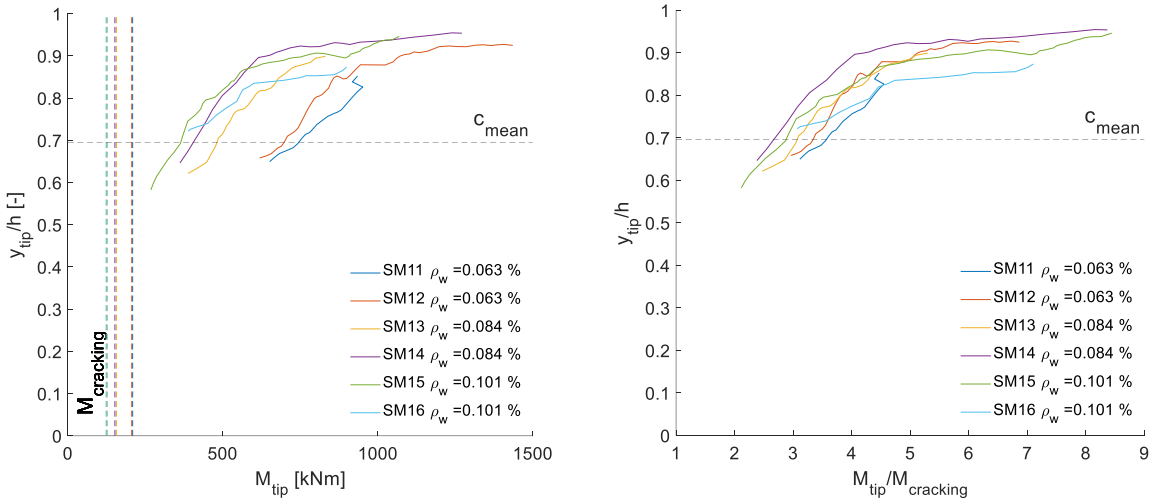

Figure 26 – SM10 North face : actual y-coordinate of the crack tip as a function of the bending moment at the crack tip M_{tip} (left) and of the ratio of the bending moment at the crack tip M_{tip} to the cracking moment $M_{cracking}$ (right).

The crack tip y_{tip}, normalized over the section height h to make it adaptable to other beam configurations, has been represented in Figure 26 as a function of the ratio of the bending moment calculated in the section located at the crack tip M_{tip} to the cracking moment $M_{cracking}$. A relationship of the type $y = c_1(1 - 1/x)$ has been fitted (36) using the initial load and crack tip position to obtain the coefficient c_1. An additional condition using relation (35) ensures that the crack the crack tip y_{tip} never exceeds the section height h, i.e. $\frac{y_{tip}}{h} < 1$ when $\frac{x_{tip}}{a} = 1$.

$$\frac{y_{tip}}{h} = c_1\left(1 - \frac{1}{\frac{M_{tip}}{M_{cracking}}}\right) = c_1\left(1 - \frac{1}{\frac{x_{tip} \cdot V}{M_{cracking}}}\right) \tag{36}$$

with initial conditions: $c_1 = \frac{\frac{y_{tip,initial}}{h}}{1 - \frac{1}{\frac{x_{tip,init} \cdot V_{init}}{M_{cracking}}}} < \frac{1}{1 - \frac{1}{a_1 + b_1}}$

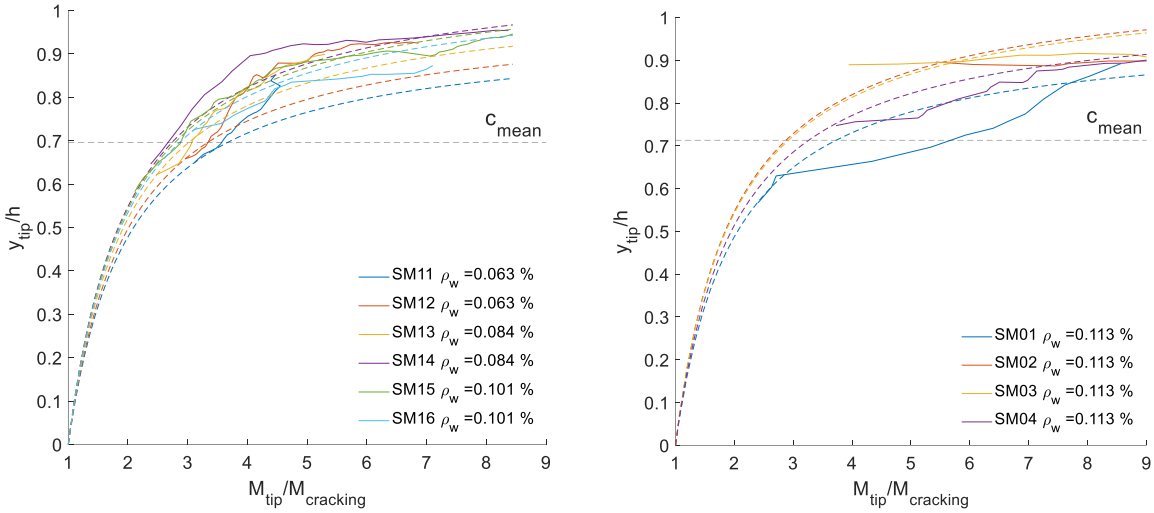

Figure 27 - North face SM10 (left) and SM00 (right) : actual y-coordinate of the crack tip as a function of the ratio of the bending moment at the crack tip M to the cracking moment $M_{cracking}$ with fitted experimental relation (dashed).

The relation (36) fitted on SM10 results was in a second phase tested on the validation set SM00 (Figure 27). The observed relationship for SM10 specimens is not present in the SM00 validation test set, compromising the soundness of relation (36).

7 Critical shear crack kinematics prediction

7.1 Kinematics prediction based on a constant rotation increment

Hugo Nick (2023) presented in his Master thesis [17] a method to predict crack kinematics evolution from a given initial state. This method relies on a bilinear approximation of the failure surface and is based on Cavagnis et al. (2018) [8] who observed with DIC measurements that the sum of the horizontal components of the crack widths of all cracks tributary to the CSC form at peak load an almost linear profile, as illustrated in Figure 28. With a known rigid-body rotation increment $\Delta\psi$, the kinematics predictions obtained from an initial state at 75% of the maximum load using Hugo Nick's method [17] were close to the real measurements of the SM10 specimens. However, obtaining a prediction for the rigid-body rotation increment $\Delta\psi$ was unsuccessful.

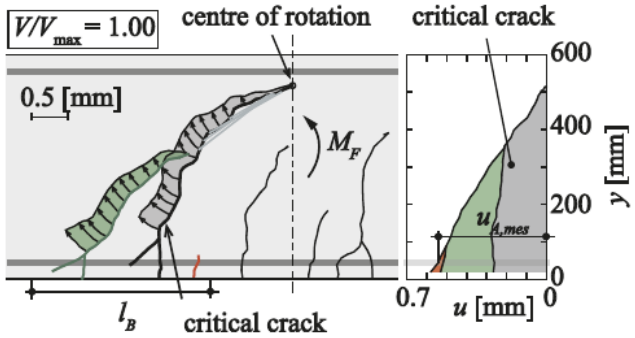

Figure 28 - Crack kinematics, center of rotation and horizontal opening u of the cracks tributary to the opening of the critical shear crack in a region of length l_B. Cavagnis et al. (2018) [8]

In an attempt to predict the crack kinematics, here in particular the crack opening w, an algorithm inspired by the work of Hugo Nick [17] based on the rigid-body rotation hypothesis is proposed. The center of rotation can be approximated as the tip of the failure crack. (Fernández (2021) [7])

The crack rotation ψ_i for each point i of the crack is therefore defined as follows:

$$\psi_i = \frac{w_{\perp \mathrm{L},i}}{L_i} \tag{37}$$

with $L_i = \sqrt{(x_{tip} - x_i)^2 + (y_{tip} - y_i)^2}$ the distance from the point i to the crack propagating tip at the load level considered and $w_{\perp \mathrm{L},i}$ the crack opening perpendicular to L_i as illustrated in Figure 29. The crack opening is obtained with the simplified expression:

$$w_i \cong w_{\perp \mathrm{L},i} \cdot cos(\alpha_i - \lambda_i) \tag{38}$$

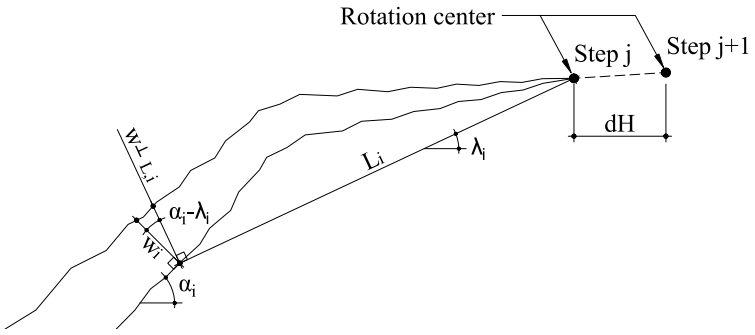

Figure 29 – Schematic definition of the CSC geometric parameters

The proposed algorithm starts with applying a horizontal propagation increment dH to the tip of the CSC at its initial state. The bilinear approximation described in chapter §5 is used to obtain the coordinates of the new predicted crack point:

$$x_{predicted,tip} = x_{initial,tip} + dH \quad (39)$$

$$y_{predicted,tip} = y_{initial,tip} + dH \cdot tan(\alpha_{bilinear}) \quad (40)$$

This new predicted crack point is arbitrarily assigned a crack opening corresponding to the DIC error $err_{DIC} = 0.01\ mm$ for the SM10 series. This is the chosen criterion to define the crack tip from the DIC measurements, lower values being considered unreliable to detect the presence of an actual discontinuity and treated as a continuous medium.

$$w_{predicted,tip} = err_{DIC} \quad (41)$$

The predicted crack opening along all other points i becomes the sum of the initial crack openings and a new component composed of a constant rotation increment $\Delta\psi_{cst}$ times the distance $L_{predicted,i}$ from the point i to the new crack propagating tip defined by equations (39) and (40):

$$w_{predicted,i} = w_{initial,i} + \Delta\psi_{cst} \cdot L_{predicted,i} \quad (42)$$

In order to find the constant rotation increment, the actual rotation increment has been calculated for all crack points i and the mean of the actual increment $d\psi_{mean,j}$ at each step j has been represented along with the actual rotation in Figure 30 and Figure 31 as per equation (43). The complete results for all specimens are available in appendix §11.4.

$$d\psi_{mean,j} = \frac{1}{n}\sum_{i=1}^{n}(\psi_{i,j} - \psi_{i,j-1}) \quad (43)$$

The initial load level considered for each specimen are listed in Table 8. They differ between specimens due to the failure surface development occurring closer to failure for specimens with lower transversal reinforcement ratios than for those with higher ratios.

Table 8 – Initial load level considered for each specimen

Specimen	SM11	SM12	SM13	SM14	SM15	SM16
Initial load level considered	90% V_{max}	90% V_{max}	55% V_{max}	55% V_{max}	45% V_{max}	45% V_{max}

The mean actual rotation increment turns out to vary differently across specimens. The specimens SM11 and SM12 (Figure 30) with the lowest transverse reinforcement ratio present mean actual rotation increment spikes reflecting a more brittle behavior with sudden local failures where the rotation increases abruptly.

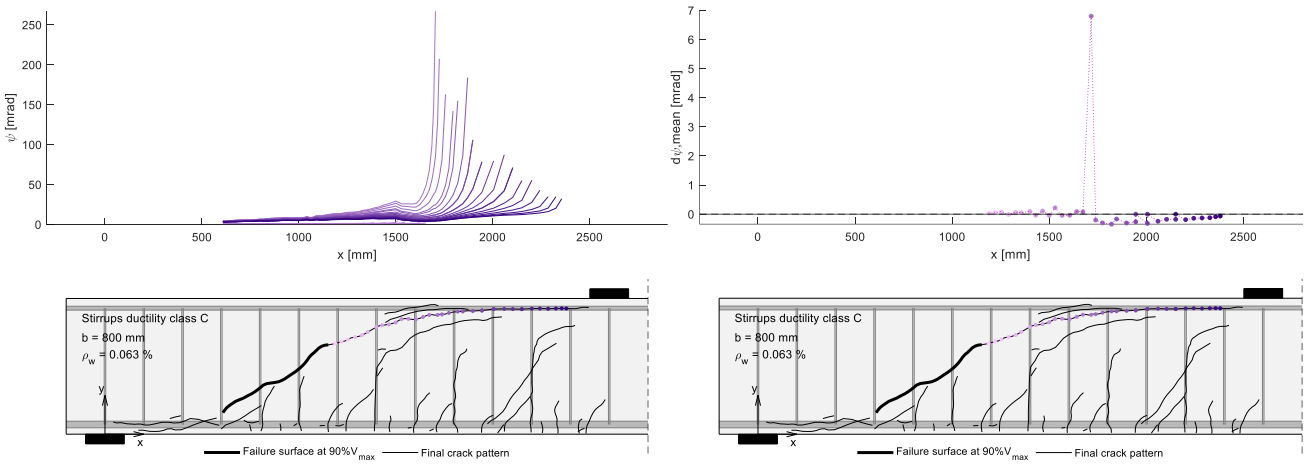

Figure 30 - SM12 North: crack rotation along the crack (left) and mean rotation increment (right) at each step of the crack propagation

On the other hand, specimens SM13, SM14 (Figure 31), SM15 and SM16 present a more regular behaviour. The regularity of the mean actual rotation increment could be disturbed locally as close cracks parallel to the quasi-horizontal portion of the failure crack form. For all specimens, the rotation increases mostly as the quasi-horizontal part of the failure crack develops.

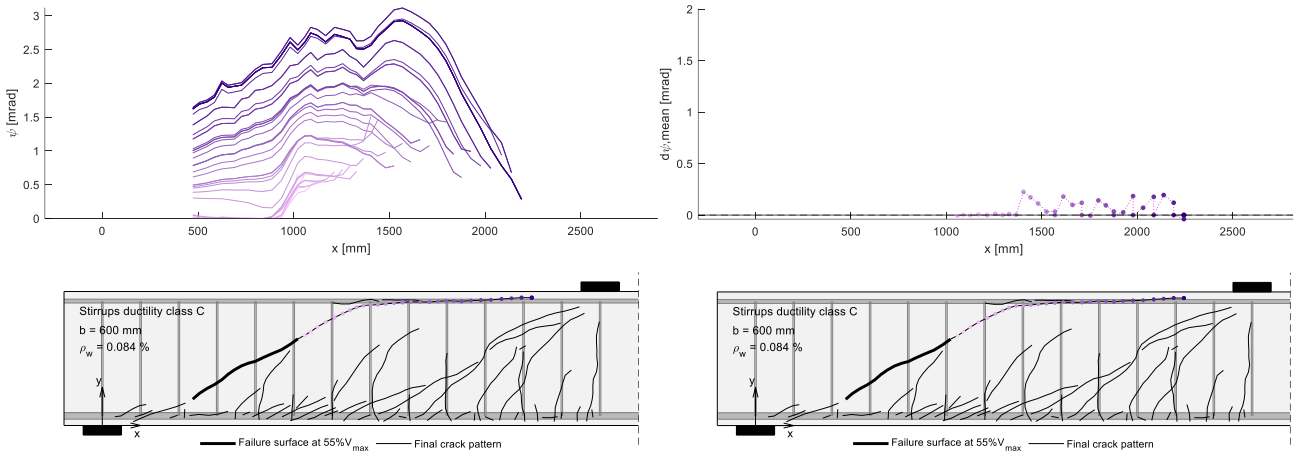

Figure 31 – SM14 North : crack rotation along the crack (left) and mean rotation increment (right) at each step of the crack propagation

The constant rotation increment used for predictions $\Delta\psi_{cst}$ is first calculated with the mean of the actual rotation increments $\Delta\psi_i$ along the crack and load for each SM10 specimen (see Table 9). The objective is to try out the algorithm with a measured constant rotation increment, before attempting to develop predicted values.

Table 9 – Constant rotation increment measured with the mean of the actual rotation increments along the crack and load for each specimen

Specimen	SM11	SM12	SM13	SM14	SM15	SM16
Constant rotation increment $\Delta\psi_{cst}$ [mrad]	0.172	0.328	0.080	0.154	0.287	0.134

The crack opening is then determined using equation (42) and the results are displayed in Figure 32. It should be noted that mild smoothing is applied on the actual measurement in order to reduce the local variations and enhance the quality of the predicted values.

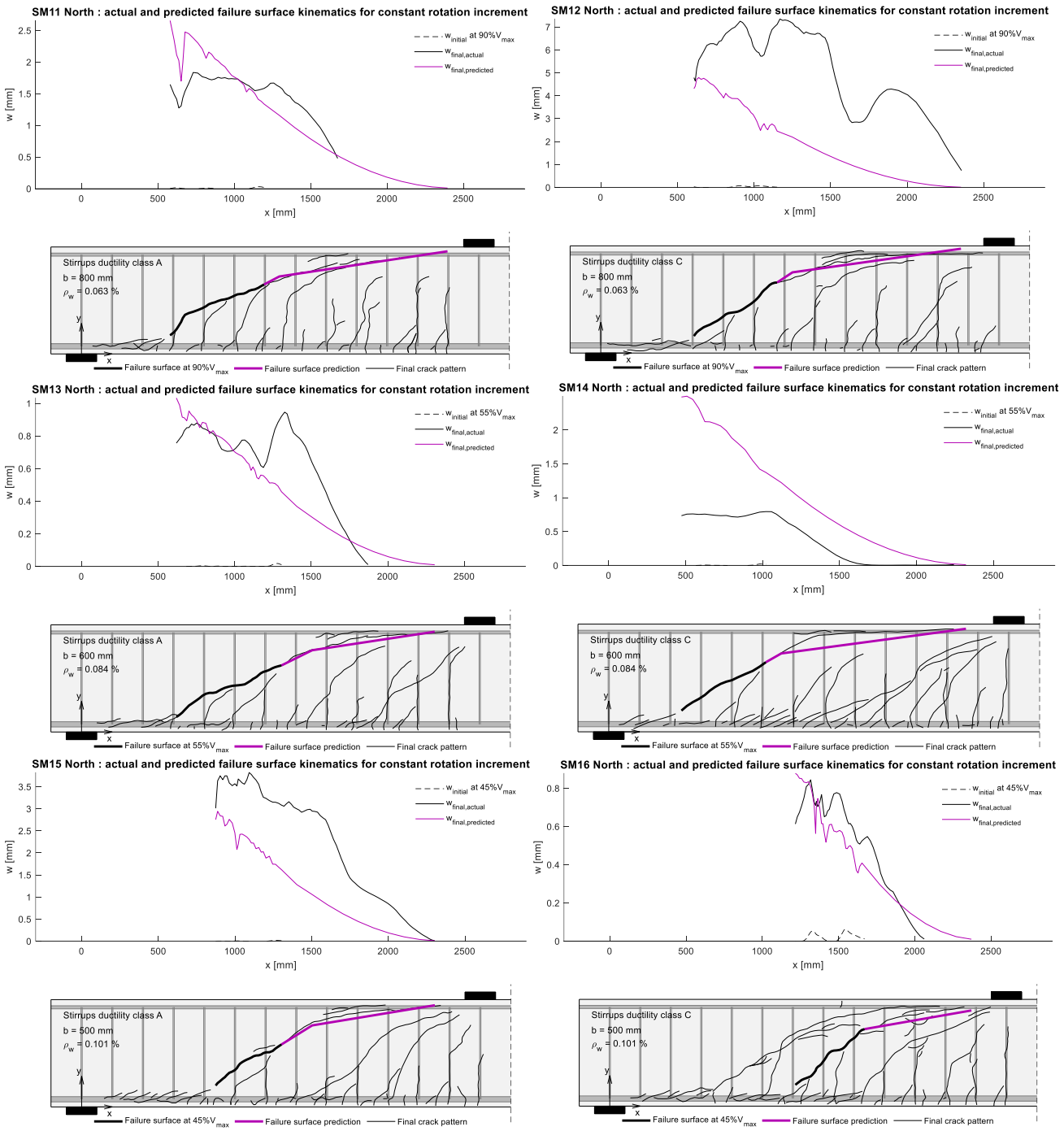

Figure 32 – Actual (black) and predicted (purple) crack opening at ultimate load. The initial crack opening (dashed black) corresponds to the initial load level chosen for each specimen

Figure 32 shows differences between the predicted and actual crack opening. Although predicted values sometimes come close to the actual values, it is generally not the case. The regular, almost linear predicted curve shape do not represent the irregularity of the actual curve. Furthermore, the mean of the actual rotation increments $\Delta\psi_i$ defined in Table 9 do not seem to correlate to the specimen parameters described in chapter §3 and no way to calculate its value in the initial state has been found.

While better results would be obtained for the constant rotation increment method using an initial load level closer to the ultimate load, the inability to calculate the constant rotation increment makes this method inapplicable. In conclusion, the failure crack rotation proved difficult to predict as it presents a high variability.

7.2 Kinematics prediction based on a single propagation increment

In a second attempt to predict the failure surface kinematics, a single horizontal propagation increment dH was applied to the crack tip in a given initial state. The new predicted crack point is located in the linear extension of the initial crack, with an inclination corresponding to the average angle of the crack tip over an arbitrarily chosen distance of $3 \cdot dH$ as per Figure 33.

$$x_{tip,predicted} = x_{tip,init} + dH \tag{44}$$

$$y_{tip,predicted} = y_{tip,init} + dH \cdot tan(\alpha_{mean}) \tag{45}$$

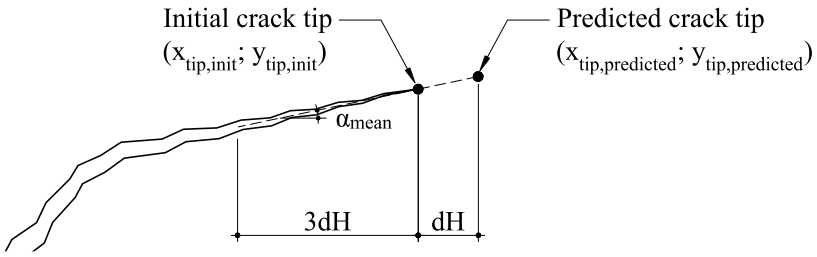

Figure 33 -Linear approximation adopted for the geometry of the predicted crack tip

To avoid the need to determine the crack rotation, which was unsuccessful in chapter §7.1, relations on the horizontal crack opening u have been derived to predict the kinematics after a single propagation increment.

Cavagnis (2018) [8] proposed a relationship between the horizontal crack opening and the strain at the flexural reinforcement height ε_s using a tributary length $l_{trib} = d - c$. This relation is valid for RC beams without transverse reinforcements at load levels close to failure.

$$u_s = \varepsilon_s \cdot l_{trib} = \varepsilon_s \cdot (d - c) \tag{46}$$

$$\text{with } \varepsilon_s = \frac{V \cdot x_{tip}}{E_s \cdot A_s \cdot (d - c/3)} \tag{47}$$

The strain is the tensed flexural reinforcements ε_s at the crack tip section is calculated by sectional analysis considering a linear profile of compression stresses and neglecting concrete tension. It was compared to the available FOM measurements in the tensed flexural reinforcements $\varepsilon_{s,FOM}$ at the crack tip section (Figure 34). The calculated ε_s tends to underestimate the FOM values but follows them relatively well at load levels close to the ultimate load.

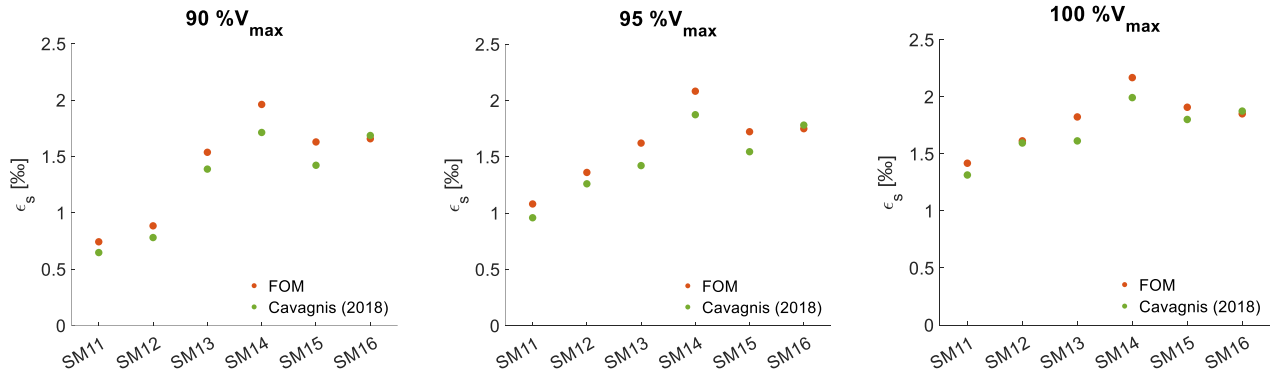

Figure 34 – FOM tensed flexural reinforcement strain at the crack tip section compared to Cavagnis's (2018) [8] relation at load levels close to the ultimate load

Cavagnis's relation was used to calculate the predicted horizontal crack opening increment Δu. However, since the DIC measurements are unavailable at the flexural reinforcements, the strain of the first available point of the failure crack close to the bottom surface $\varepsilon_{init}(1)$ is used instead of $\varepsilon_{s,init}$.

$$\varepsilon_{init}(1) = \frac{V_{init} \cdot x_{tip,init}}{E_s \cdot A_s \cdot (h - y_{init}(1) - c/3)} \tag{48}$$

The corresponding tributary length is estimated from the first crack point initial horizontal crack opening, and the predicted tributary length is modified by the same vertical increment than the predicted crack tip:

$$l_{trib,init} = \frac{u_{init}(1)}{\varepsilon_{init}(1)} \tag{49}$$

$$l_{trib,predicted} \cong l_{trib,init} + dH \cdot tan(\alpha_{mean}) \tag{50}$$

Assuming again $V_{predicted} \cong V_{init}$, the first crack point horizontal crack opening prediction is calculated, and its value is linearly extrapolated to the rest of the crack with the predicted crack tip as origin and assumed center of rotation.

$$\varepsilon_{predicted}(1) = \frac{V_{predicted} \cdot x_{tip,predicted}}{E_s \cdot A_s \cdot (h - y_{init}(1) - c/3)} \cong \frac{V_{init} \cdot x_{tip,predicted}}{E_s \cdot A_s \cdot (h - y_{init}(1) - c/3)} \tag{51}$$

$$u_{predicted}(1) = \varepsilon_{predicted}(1) \cdot l_{trib,predicted} \tag{52}$$

$$\Delta u(1) = (u_{predicted}(1) - u_{init}(1)) \tag{53}$$

$$u_{predicted}(i) = u_{init}(i) + \Delta u(1) \cdot \frac{y_{tip,predicted} - y_{predicted}(i)}{y_{tip,predicted} - y_{predicted}(1)} \tag{54}$$

$$u_{predicted}(end + 1) = err_{DIC,u} \tag{55}$$

The results displayed in Figure 35 shows that the predictions after relation (54) tend to underestimate the actual horizontal crack opening, but an overestimation is noted for SM11 and SM14. The hypothesis of a constant shear force is not causing this underestimation as relation (54) was also represented in Figure 35 in green using the actual final shear force V_{final}, resulting in slightly better results for most specimens. Both predicted curves are sometimes overlapping as the shear force increase is small. The predictions based on Cavagnis's (2018) [8] relation do not match the actual horizontal crack opening.

Other algorithms have been tested also unsuccessfully, for example one assuming a horizontal crack opening increment proportional to the bending moment augmentation at the crack tip section $\Delta u \propto \Delta M$.

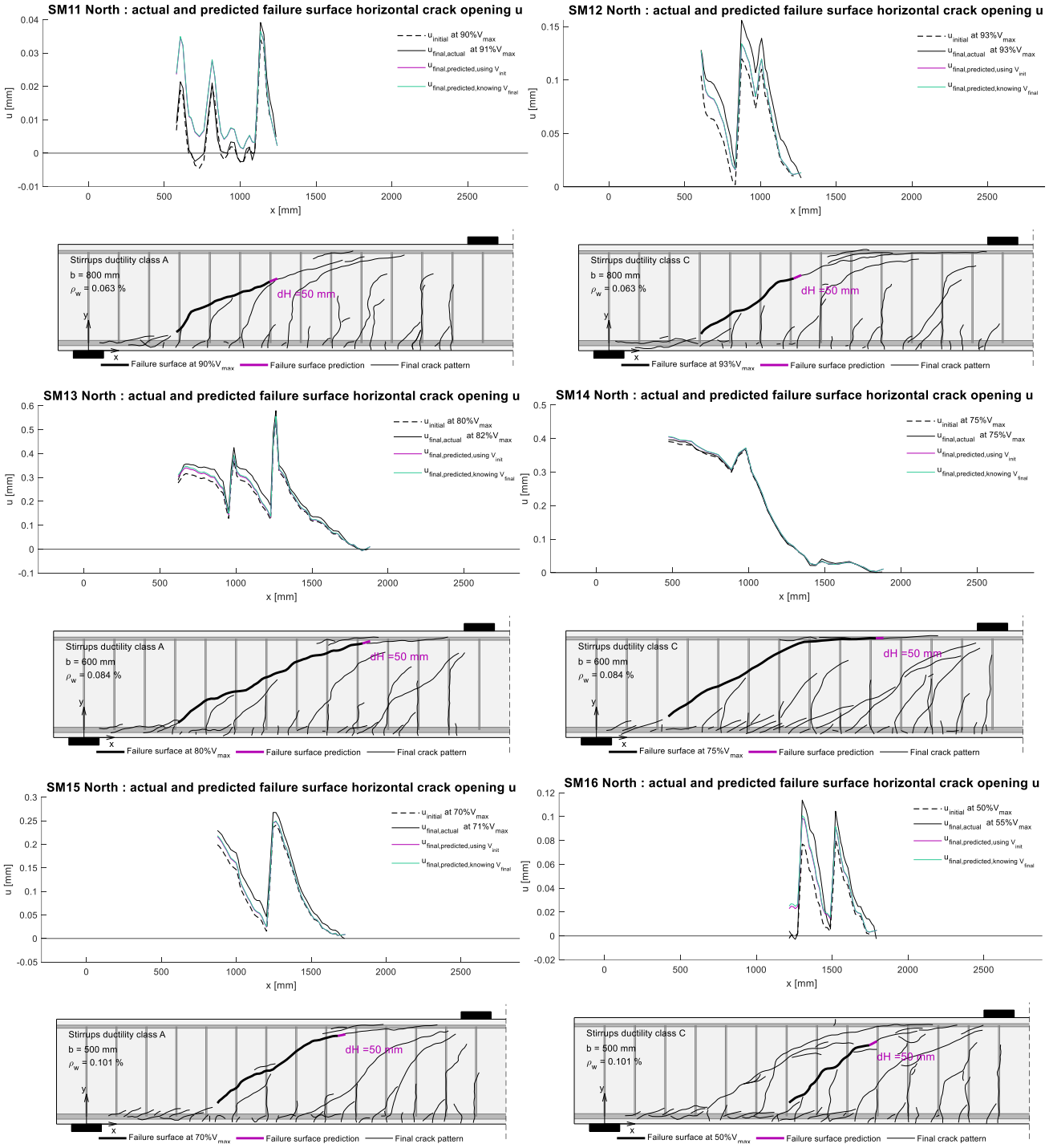

Figure 35 - SM10 North: Actual and predicted failure surface horizontal crack opening based on Cavagnis's (2018) [8] relation. Actual initial (dashed black) and final (black) horizontal crack opening, predicted horizontal crack opening using constant shear force (purple) and predicted horizontal crack opening using actual final shear force (green).

However, condensing the horizontal opening into a single crack does not correspond to the hypothesis of Cavagnis et al. (2018) [8] explained in chapter § 2.3. In fact, it is the sum of the horizontal crack openings on the cracks tributary to the CSC that gives a linear relationship close to ultimate load according to Cavagnis [8]. The tributary cracks are defined as the cracks connected to the CSC whose origin is located over a length $l_B \cong d$ around the CSC's origin, as illustrated in Figure 28.

The sum of the horizontal crack openings for the selected tributary cracks have been represented in Figure 36 and Figure 37. The complete results for all specimens including the sum of the vertical crack openings are available in appendix §11.5. The horizontal crack opening at the height of the flexural reinforcement u_s calculated using Cavagnis' equations (46) and (47) is also represented. However, the DIC kinematics measurements are not available between the bottom surface and a height of about 150mm due to the bottom smeared cracking of the failure crack preventing its clear definition around the flexural reinforcements. The failure surface is referred to in the figures as "CRI".

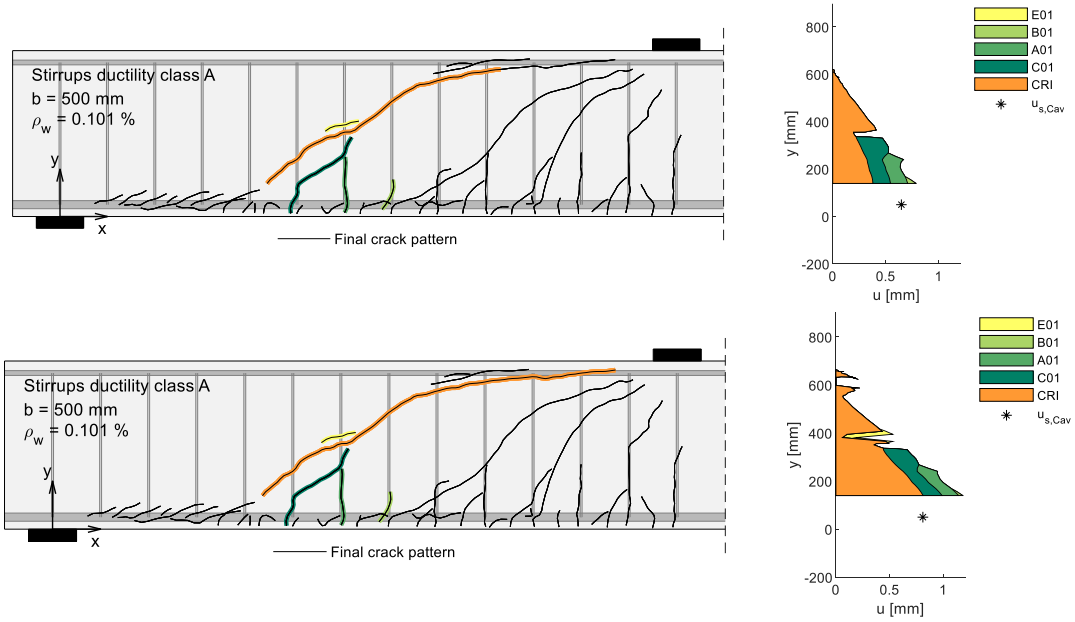

Figure 36 – SM15 North: actual horizontal crack opening u of different cracks combined at 80% (top) and 100% (bottom) of the ultimate load and calculated horizontal crack opening $u_{s,Cav}$ after Cavagnis (2018) [8]

Although a relatively linear relationship of the sum of the horizontal crack opening is indeed found for the SM10 series, Cavagnis' calculated horizontal crack openings does not lie consistently either in the extension of those of the failure surface or the sum of the tributary cracks. Considering the sum of the horiztonal crack opening those cracks instead of that of the failure crack only will not improve the kinematics predictions.

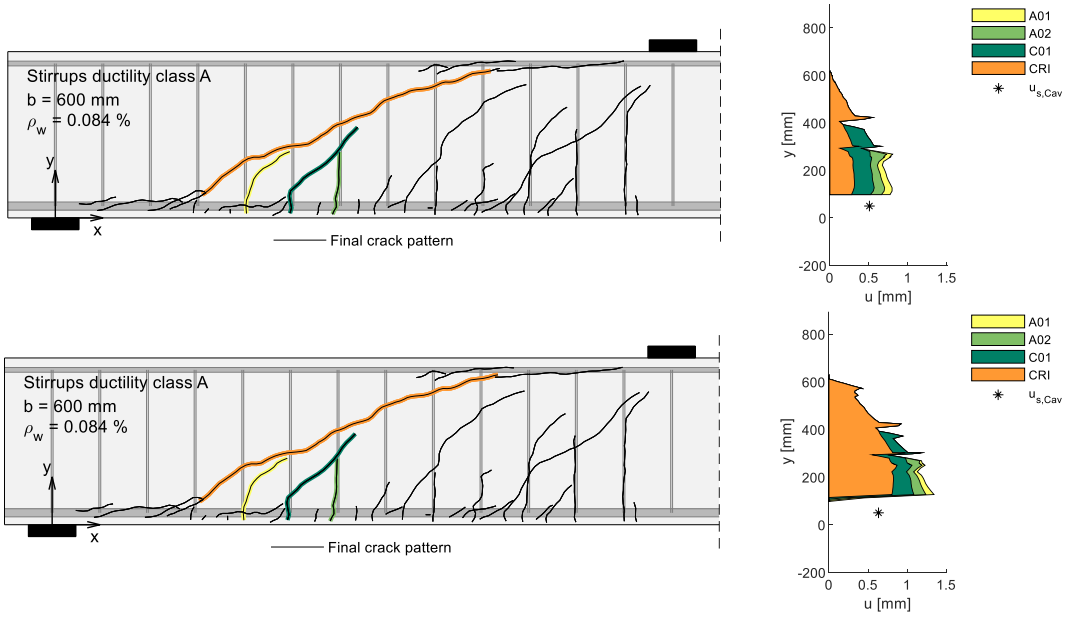

Figure 37 - SM13 North: actual horizontal crack opening u of different cracks combined at 80% (top) and 100% (bottom) of the ultimate load and calculated horizontal crack opening $u_{s,Cav}$ after Cavagnis (2018) [8]

Figure 36 and Figure 37 also show that the secondary cracks originating from the bottom face of the beams tend to open up sharply at the top when they connect to the failure crack. This phenomenon is particularly marked on crack C01 of specimen SM15.

Conversely, the presence of secondary cracks, particularly the connected ones, influence the failure surface kinematics. Indeed, Figure 38 shows the horizontal crack opening u of SM13 and SM14 projected on the x-axis for better visibility. The actual failure surface kinematics of the SM10 specimens, crack opening and slip as well as horizontal and vertical crack openings, are displayed in appendix §11.1. The close load steps show a regularly increasing horizontal crack opening for uncracked regions. However, this behaviour is highly disturbed as secondary cracks reach the failure surface. This is visible in specimen SM13 at $x = 1000\,mm$ and $x = 1250\,mm$, as well as specimen SM14 at $x = 1400\,mm$ where the horizontal crack opening starts decreasing with the load due to a neighboring crack.

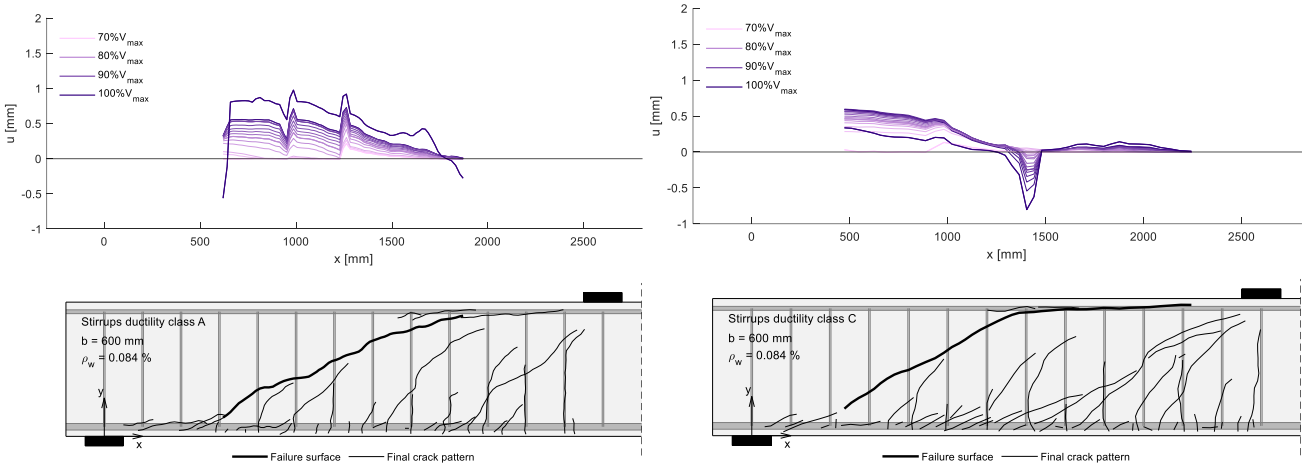

Figure 38 – SM13 (left) and SM14 (right) North: actual horizontal crack opening evolution during loading. Each line is 2% V_{max} apart.

The actual kinematics show a complicated deformation scheme. The predictions in Figure 35 tend to underestimate the horizontal crack opening due to its distribution pattern not being linear as would be expected if the concrete body on either side of the crack behaved as rigid bodies.

The rotation of the CSC in RC members without shear reinforcements is often assumed constant up to the tip of the crack and zero after as illustrated in Figure 39 a). This is based on the hypothesis that both concrete portion on either side of the CSC behave as a rigid body with a rotation center at the crack tip.

In order to test this hypothesis for RC member with shear reinforcements, the relative rotation of the compression chord has been calculated by setting points regularly on a line along the compression chord using VIC software and comparing their displacements to two reference points placed under the CSC, on a portion of the beam assumed to behave as a rigid body. The horizontal angle between two points is calculated with the following relation:

$$\theta_i = \arctan\left(\frac{P_{y,i+1} - P_{y,i}}{P_{x,i+1} - P_{x,i}}\right) \tag{56}$$

Then, the angle difference between two line points i and the reference points is retrieved:

$$\Delta\theta_i = \theta_{ref} - \theta_{line,i} \tag{57}$$

Finally, the relative rotation of the compression chord is calculated by the angle variation between initial load and current load j:

$$\psi_{i,j} = \Delta\theta_{i,j} - \Delta\theta_{i,0} \tag{58}$$

The complete results are displayed in Figure 42. Specimen SM15 missing data is due to cables obstructing the DIC. The usual constant rigid-body rotation profile schematized in Figure 39 a) was not reflected in the actual measurements. Two types of rotation profile were found : the actual types in Figure 39 b) and c) where the rotation is constant up to a x-coordinate hereafter defined as $x_{\psi,2}$, which approximately corresponds to the start of the quasi-horizontal crack portion. After this point, the rotation decreases linearly and becomes negative approching the loading plate. This reflects a deformation of the compressed chord after $x_{\psi,2}$, which bends and behaves akin to a small beam embedded at $x_{\psi,2}$ and at the CSC tip. The transition between a constant rotation and the linear profile is very gradual in specimens with a lower transverse reinforcement ratio ρ_w (SM11 and SM12) and at lower load levels for all beams.

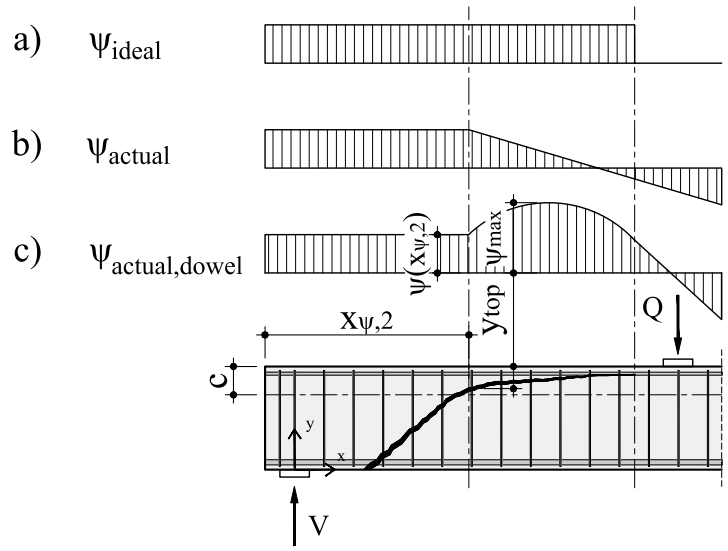

Figure 39 – Compressed chord relative rotation: a) rigid-body hypothesis scenario, b) actual idealized scenario, c) actual idealized scenario with dowel effect

For certain specimens with a higher transverse reinforcement ratio ρ_w (SM14, SM15 and SM16) close to failure (from 80 to 90% V_{max}), a bulging of the previously linear rotation occurs as per Figure 39 c). This could occur due to the dowel effect of the top flexural reinforcement which causes additional shear deformation in the compressed chord locally, especially when the CSC gets close to the top surface of the beam. For specimen SM16, this effect is probably caused by the major crack "A01" located close to the surface, and not the designated CSC. This bulging could be used as an indicator of imminent failure.

Several possible correlation have been tested to find a link between the parameters of the specimens SM10 and the x-coordinate $x_{\psi,2}$. A relation between the ratio of the vertical distance named y_{top} between the crack at x-coordinate $x_{\psi,2}$ and the top of the beam to the elastic cracked neutral axis c was attempted but proved quite variable across the specimens. The considered crack is the CSC, but the major crack "A01" closer to the support and to the top surface of the beam was also selected for SM16.

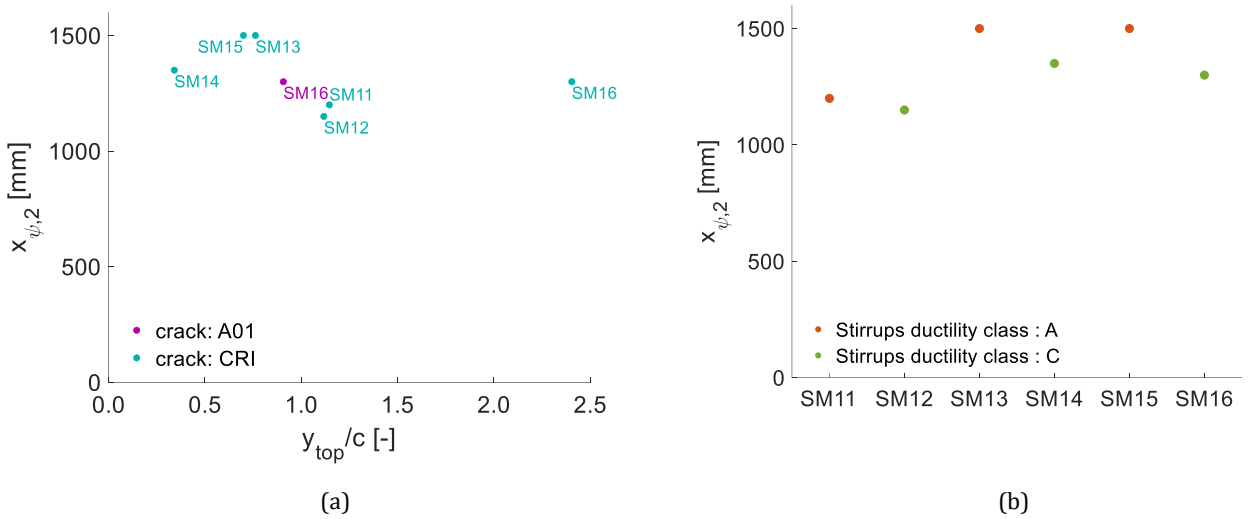

Figure 40 – North face : (a) crack distance to the top y_{top} at x-coordinate $x_{\psi,2}$ to cracked neutral axis c ratio; (b) x-coordinate $x_{\psi,2}$ and stirrups ductility class relationship

Relatively high variability across the specimens has also been found using different parameters such as the slenderness ratio h/b. The only consistent relationship found is the link between $x_{\psi,2}$ and the ductility class of the stirrups as per Figure 40 (b). Indeed, the major difference between specimen couples SM11-SM12, SM13-SM14 and SM15-SM16 lays in the stirrups ductility class. $x_{\psi,2}$ is systematically slightly higher for the couple's specimens with stirrups of ductility class C than for those with ductility class A.

The dowel action of the top flexural reinforcement was calculated according to Cavagnis et al. (2017) [3]. It has been compared to the ratio of the maximum rotation ψ_{max} to the rotation of the constant portion at x-coordinate $\psi(x_{\psi,2})$ illustrated in Figure 39 in order to find a relationship between the rotation bulging observed in the compression chord of specimens SM14, SM15 and SM16 and the dowel action. The CSC of specimen SM16 do not generate any dowel action of the top flexural reinforcement, but crack "A01" does. It follows that no strong direct relationship can be demonstrated as per Figure 41.

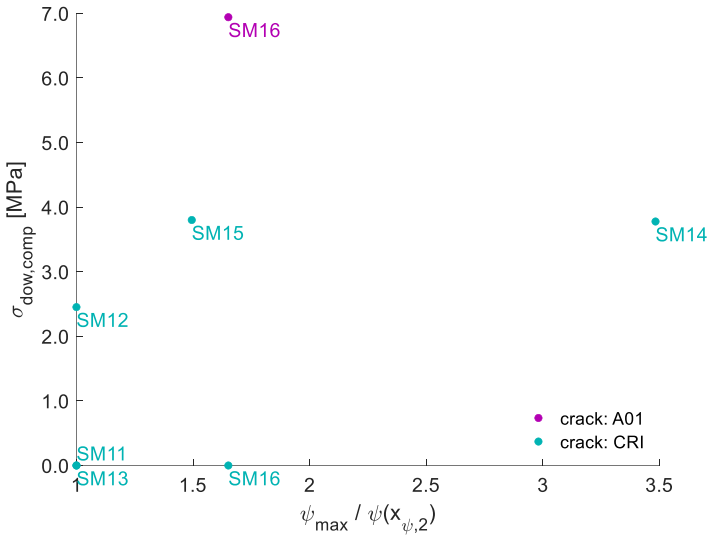

Figure 41 – Dowel action stresses according to Cavagnis et al. (2017) [3] compared to the ratio of the maximum rotation ψ_{max} to the rotation of the constant portion at x-coordinate $\psi(x_{\psi,2})$

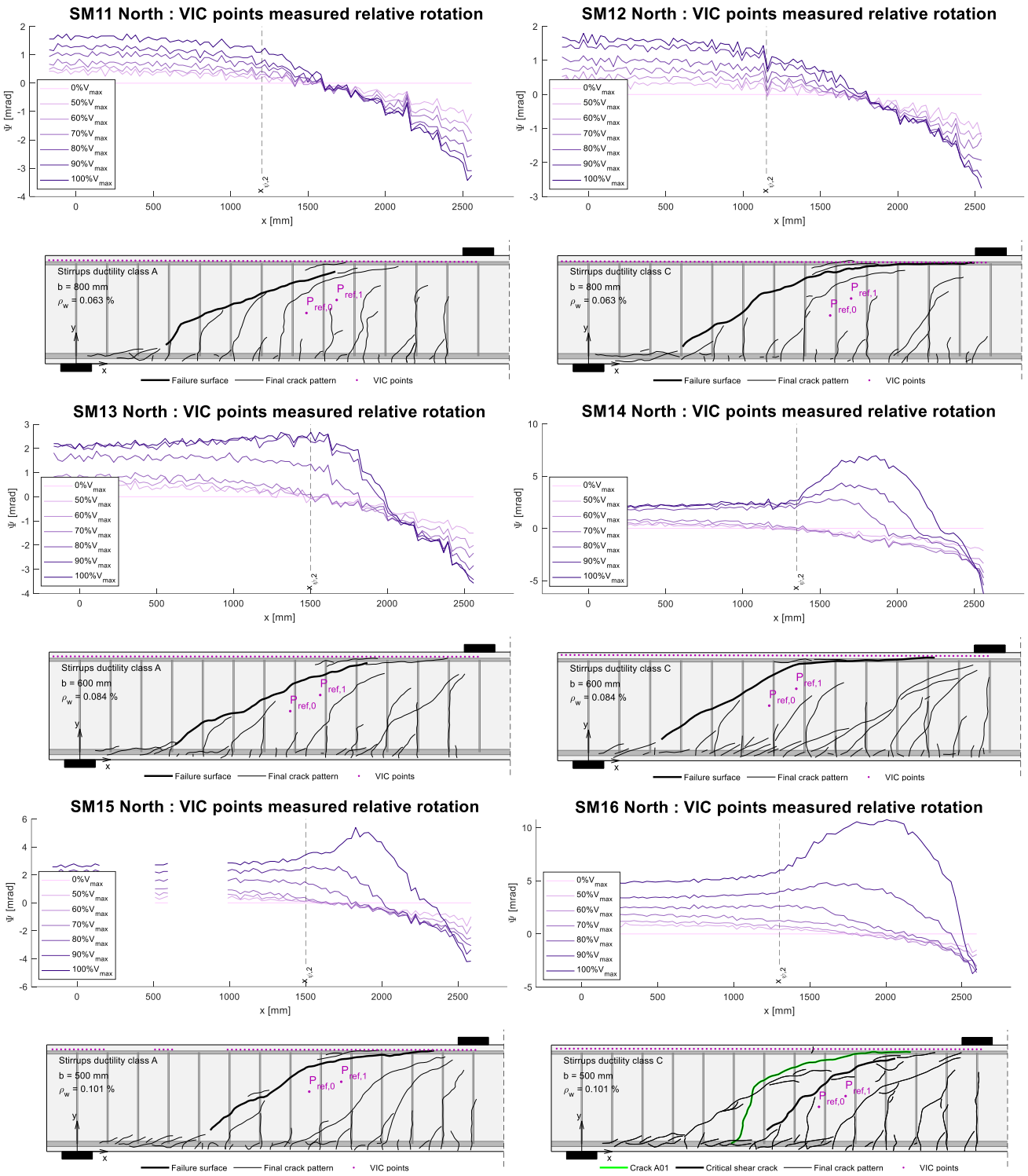

Figure 42 – Relative rotation of the compression chord along the beam compared to the reference points: critical crack (thick black), and crack A01 for specimen SM16 (green)

In conclusion, the concrete on either side of the failure crack do not behave as rigid bodies but form several articulations and local flexion occur. Multiple hypotheses valid for RC members without shear reinforcement are therefore challenged in the presence of stirrups. Crack kinematics predictions for the SM10 specimens based on a single propagation increment have failed due to the many degrees of freedom created by the presence of stirrups, which creates a highly variable behaviour even with small increments.

7.3 Kinematics prediction based on a load-propagation relationship

Chapter §7.2 highlighted the difficulty to predict the kinematics based on a single propagation increment. This section proposes instead to take a global view of the propagation by attempting to predict the horizontal crack opening u of the failure surface using the load-propagation empirical relationship in x-direction derived in chapter §6.

Indeed, this load-propagation relationship allows to calculate the tensed flexural reinforcements strain ε_s at the crack tip section previously exposed in relation (47) in chapter §7.2. Using Cavagnis' (2018) [8] equation (46), the horizontal crack opening u_s can be obtained and serve as a base value to obtain approximative kinematics predictions. It should be noted that this relationship is approximative for the SM10 specimens as seen in Figure 36 and Figure 37 of chapter §7.2.

The total horizontal crack opening along the crack has then been extrapolated linearly between the assumed value at the tensed flexural reinforcement $u_{s,predicted}$ and the null horizontal crack opening at the crack tip. This corresponds to Cavagnis' (2018) [8] hypothesis at load levels close to failure for the sum of all cracks tributary to the CSC. To obtain an estimation of the failure surface kinematics only, $u_{predicted}$ is kept constant from the height of the junction of the CSC (labeled crack in Figure 43) to the failure surface as illustrated in Figure 43. The complete results for all specimens are available in appendix §11.6.1.

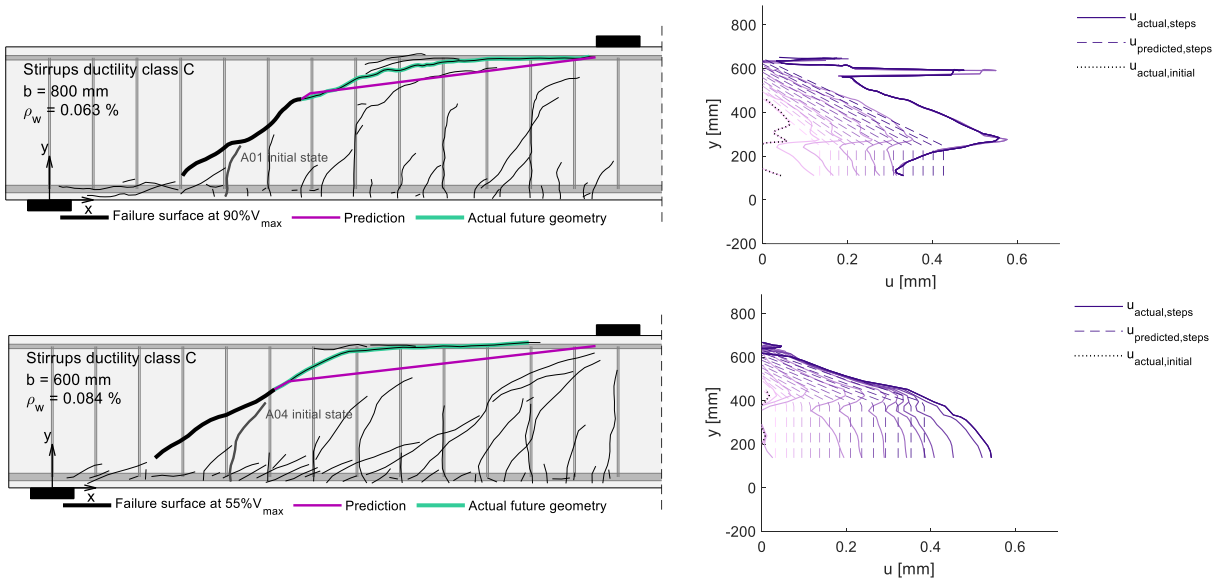

Figure 43 - SM12 (top) and SM14 (bottom) North: actual (continuous) and predicted (dashed) horizontal crack opening at every horizontal propagation step dH=100mm. The CSC is highlighted in dark grey.

The predictions for the vertical crack opening v are then obtained from the predicted horizontal crack opening assuming a rigid-body behaviour of the crack lips.

$$\psi_i = \frac{u_i}{y_{tip}-y_i} = \frac{v_i}{x_{tip}-x_i} \quad \rightarrow \quad v_i = \frac{u_i}{y_{tip}-y_i}(x_{tip}-x_i) \tag{59}$$

Figure 44 shows that the vertical crack opening predictions are very approximative. Indeed, the rigid-body hypothesis has already been challenged by the results in chapter §7.2. The complete vertical crack opening predictions for all specimens are available in appendix §11.6.2.

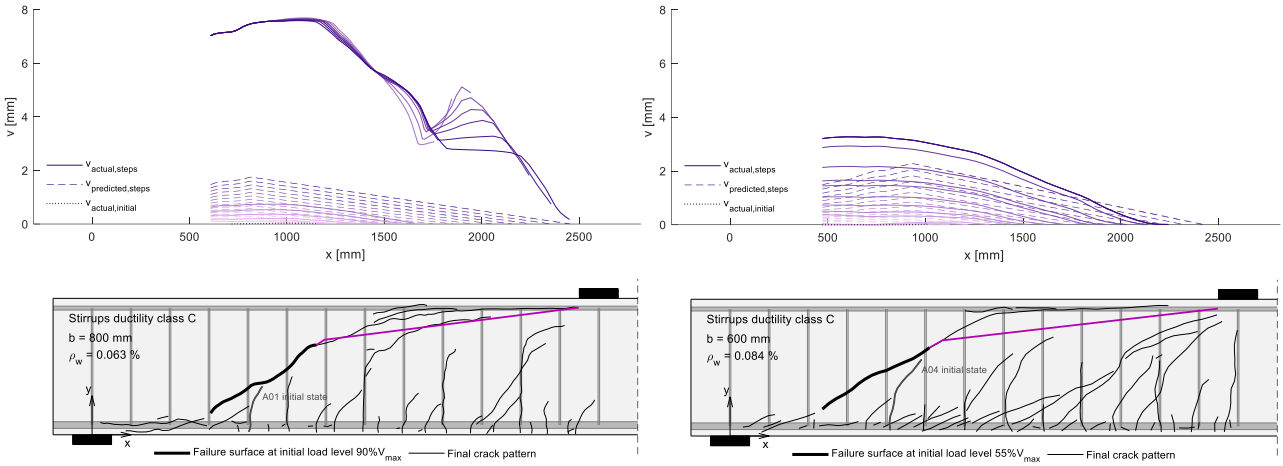

Figure 44 - SM12 (left) and SM14 (right) North : actual (continuous) and predicted (dashed) horizontal crack opening at every horizontal propagation step dH=100mm. The CSC is highlighted in dark grey.

These kinematics predictions for both horizontal and vertical crack openings follow the regularity of the load-propagation relationship developed in chapter §6 and only offer an approximation of the extremely variable actual behaviour. Although the order of magnitude and the general trend are generally respected, apart from special cases such as the SM12 specimen, the percentage of error remains high.

8 Crack criticality assessment

8.1 Crack criticality assessment based on STA analysis

8.1.1 STA method choices based on fiber optical measurements

Since FOM measurements are available for some longitudinal reinforcements and stirrups of the SM10 test series, calculation methods for dowel and stirrup action were compared in chapter §8.1.1.1 and §8.1.1.2 respectively. The methods giving the closest results to the FOM were then selected for the total STA calculation performed in chapter §8.1.2.

8.1.1.1 Comparison of dowel action calculation methods

The dowel action calculation methods of Cavagnis et al. (2017) [3] and Cavagnis et al. (2018) [8] have been compared against the available FOM data in the tensed flexural reinforcements of all SM10 specimens. The methodologies were described in chapter §2.4.3. The dowel action of the compressed flexural reinforcement can also be calculated if the crack intersects them, but they do not have FOM.

The shear force in the tensed flexural reinforcements is obtained using the mean values of the North and South bars equipped with optical fibers. The dowel action calculated corresponds to the absolute value of the local minimum of the shear force to the right of the CSC as illustrated in Figure 45. The results of the shear force in the flexural reinforcement for all specimens is found in appendix §11.2.

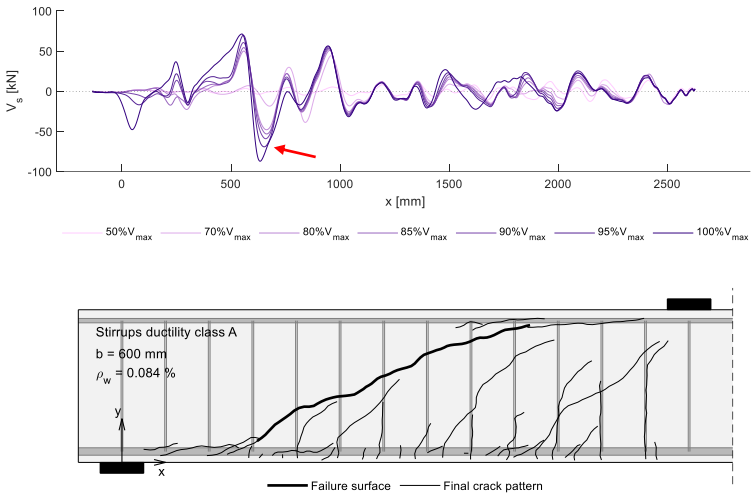

Figure 45 – SM13: shear force in the tensed flexural reinforcement calculated using FOM (mean values of both faces). The dowel action values considered are the absolute values of the local minimum of the shear force in the region of the CSC (highlighted in red)

It should be noted that the dowel action calculated using FOM are themselves subjected to error margins due for the most part to the actual position of the fibers inside the rebars, which depths can vary from around 10%. Furthermore, the CSC is not defined on the flexural reinforcements for the SM10 series because of its separation in multiple cracks at its lower end. A linear approximation of the first available points closest to the bottom surface of the beam is thus prolonged to find an approximation of the x-coordinate of the point at the height of the reinforcements.

The comparison of the two methods of Cavagnis et al. (2017) [3] and Cavagnis et al. (2018) [8] with the FOM values for all SM10 specimens is found in Figure 46.

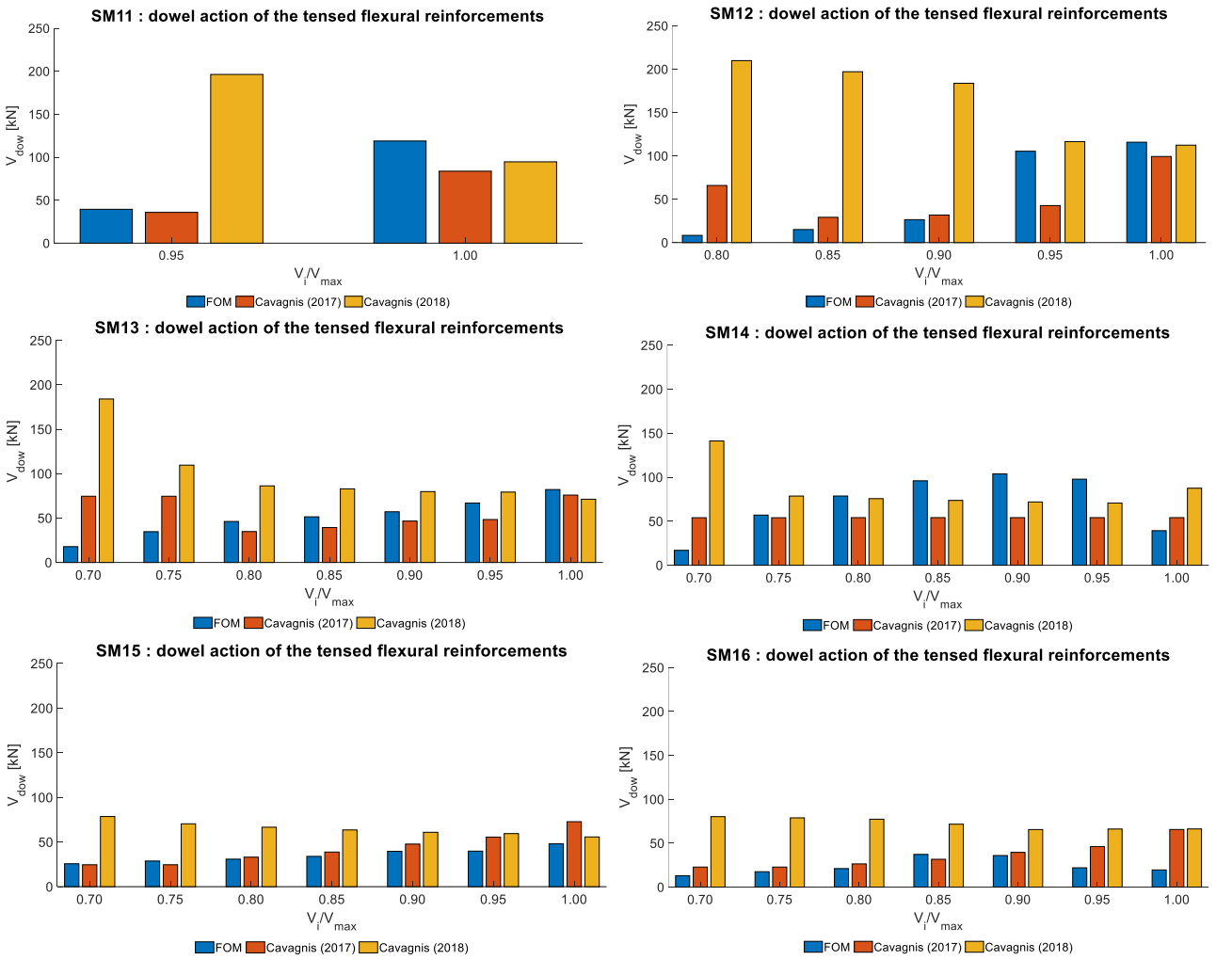

Figure 46 – Comparison of the dowel actions calculated by three methods: FOM measurements, Cavagnis (2017) [3] and Cavagnis (2018) [8]. The methods are described in chapter §2.4.3.

The dowel action at ultimate load with the method of Cavagnis et al. (2018) [8] is close to the FOM values. However, for lower load levels, its values are clearly higher. Indeed, the decaying factor $k_b = 0.063{\varepsilon_s}^{-1/4} \leq 1$ decreases with the load level and the calculated dowel action can only decrease as well. This is shown in Figure 46 apart from specimen SM14 at ultimate load. This could be due to the DIC measurements being taken slightly after failure for this specimen. Indeed, a decrease of the horizontal crack opening u at ultimate load is also visible in appendix §11.1.1 for SM14. The dowel action after Cavagnis et al. (2018) [8] decrease as the load increases, which is the opposite of the behavior observed with FOM for the SM10 specimens where the flexural reinforcement did not yield. The method of Cavagnis et al. (2018) [8] is not applicable in this case for load levels below the ultimate load.

Regarding the method of Cavagnis et al. (2017) [3], the chosen x-coordinate of the dowel action is approximative and does not to match exactly the position determined with FOM. The length of the dowelling crack assumed to be one stirrup's spacing is also approximative. The actual crack opening at the flexural reinforcements being unavailable, the crack opening at the closest point is used, which could underestimate the dowel action due to the theoretically smaller vertical crack opening, although it is not the case for specimens SM15 and SM16. The actual vertical crack openings are found in appendix §11.1.2.

Regarding specimen SM16 and to a lesser extent SM15, the relatively small values of the dowel action calculated using FOM are probably due to a more distributed cracking pattern for those specimens with the higher transversal reinforcement ratio, instead of a single major crack considered for both Cavagnis models. Figure 47 shows that the flexural reinforcements of SM16 are subjected to two shear peaks corresponding to the bottom of the two major cracks closer to the support, which mean that the dowel action of the tensed flexural reinforcement is relatively strongly activated at the intersection of several cracks and not only at the failure surface.

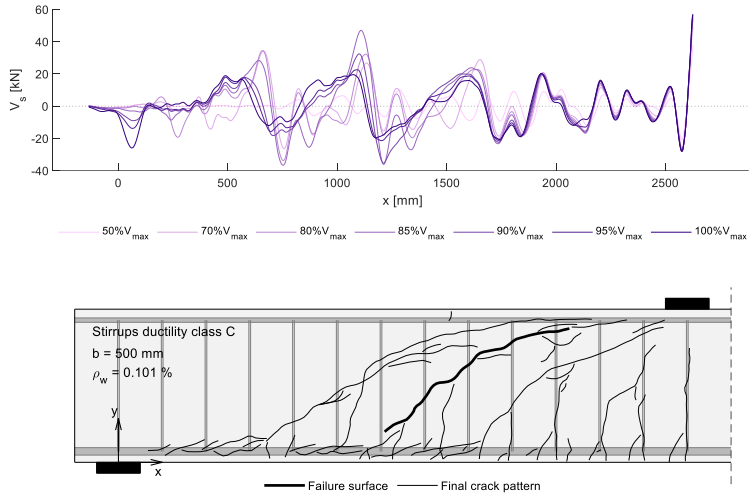

Figure 47 – SM16: shear force in the tensed flexural reinforcement calculated using FOM (mean values of both faces).

Overall, the method of Cavagnis et al. (2017) [3] using DIC measurements around the crack are generally close to the shear force calculated using FOM and this method was selected for the present study.

8.1.1.2 Comparison of shear reinforcements action calculation methods

Unlike longitudinal reinforcement, the stirrups of the SM10 specimens often yielded, and sometimes broke, before ultimate load. One of the drawbacks of the FOMs high accuracy is its sensitivity to the smallest local variation. For example, the irregularities in the bars caused by variations of the material properties and of the ribbed cross-section lead to strain concentrations. The stirrups FOM were particularly noisy near the optical fibres breaking point, or in the presence of significant transversal pressures as shown in Figure 48 (a). Such data must be post-processed, and outliers removal is recommended. (Galkovski et al. (2021) [10]) Median filtering was applied to reduce unrealistic spikes values generated by these disturbances, replacing every point of the signal by the median of the 10 neighboring points.

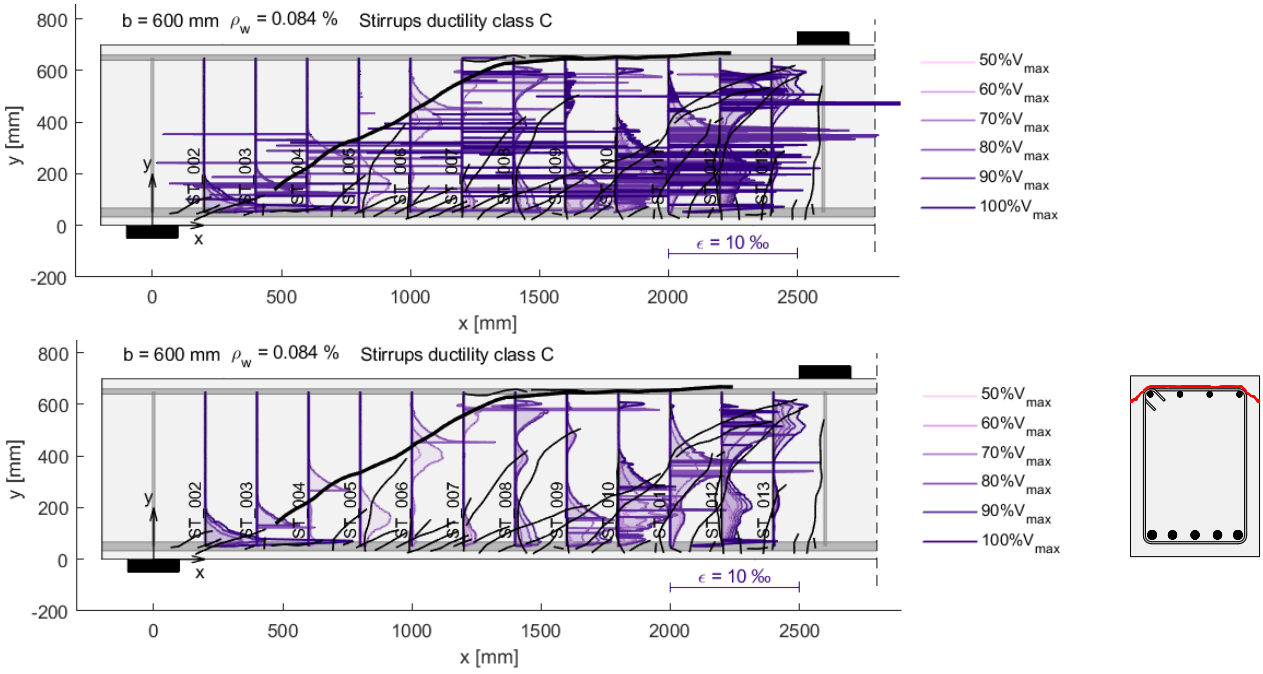

(a) (b)

Figure 48 – SM14 North: (a) FOM stirrups strains raw data (top) and with median filtering (bottom). (b) Possible fracture surface layout in the beam section in the quasi-horizontal portion

The optical fibers have a lower deformation capacity than that of the stirrups. To overcome this problem, recent developpements by Galkovski et al. (2021) [10] showed that different FOM reference steps can be set during loading in order to combine them and obtain a complete picture of the strain. The SM10 measurements had a single reference step at the beginning of loading, which only left usable measurements for the first portion of the curve up to $\varepsilon_{FOM} = 10 - 12‰$ as illustrated in Figure 49. The FOM strain at the failure surface intersection were plotted against the vertical crack opening measured with DIC. Only selected stirrups are represented due to missing data due to fibre breakage, low activated stirrups in regions where the failure crack probably only seemed to intercept the stirrups as shown in Figure 48 (b) and perturbated signals near the stirrups mandrels subjected to transversal pressure. SM11 and SM12 left no usable stirrups FOM data probably because of the brutal propagation and opening of the failure surface in those specimens with the lowest shear reinforcement ratio.

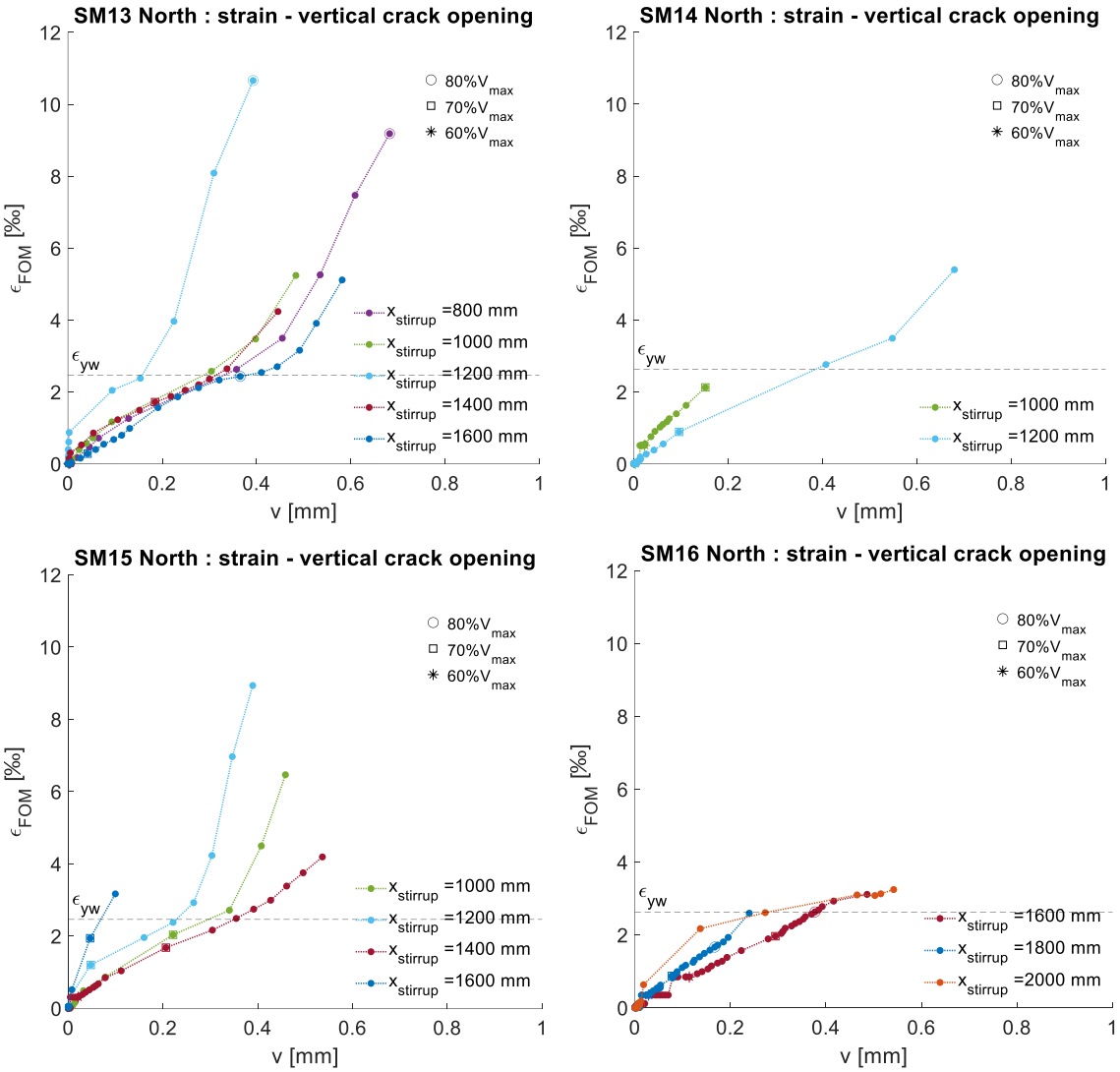

Figure 49 – Strains from FOM at the crack intersection for selected stirrups as a function of the vertical crack opening. Median filtering was applied on the FOM signal.

Figure 49 show that the strain as a function of the crack opening are relatively linear until the yield strain ε_{yw} is attained, then increases more sharply as the steel reached plastic behaviour.

The stresses derived using the shear reinforcement action calculation methods of Monney (2022) [14] and Marti (1998) [13] - Galkovski (2022) [9] have been compared against the available FOM data. The methodologies were described in chapter §2.4.6. The steel bilinear stress-strain law adopted by Campana et al. (2013) [2] and Monney (2022) [14] described in the same chapter has been implemented to obtain the stresses from the strains in the FOM. The comparison of the stresses of the two methods of Monney and Marti-Galkovski with the FOM values is found in Figure 50.

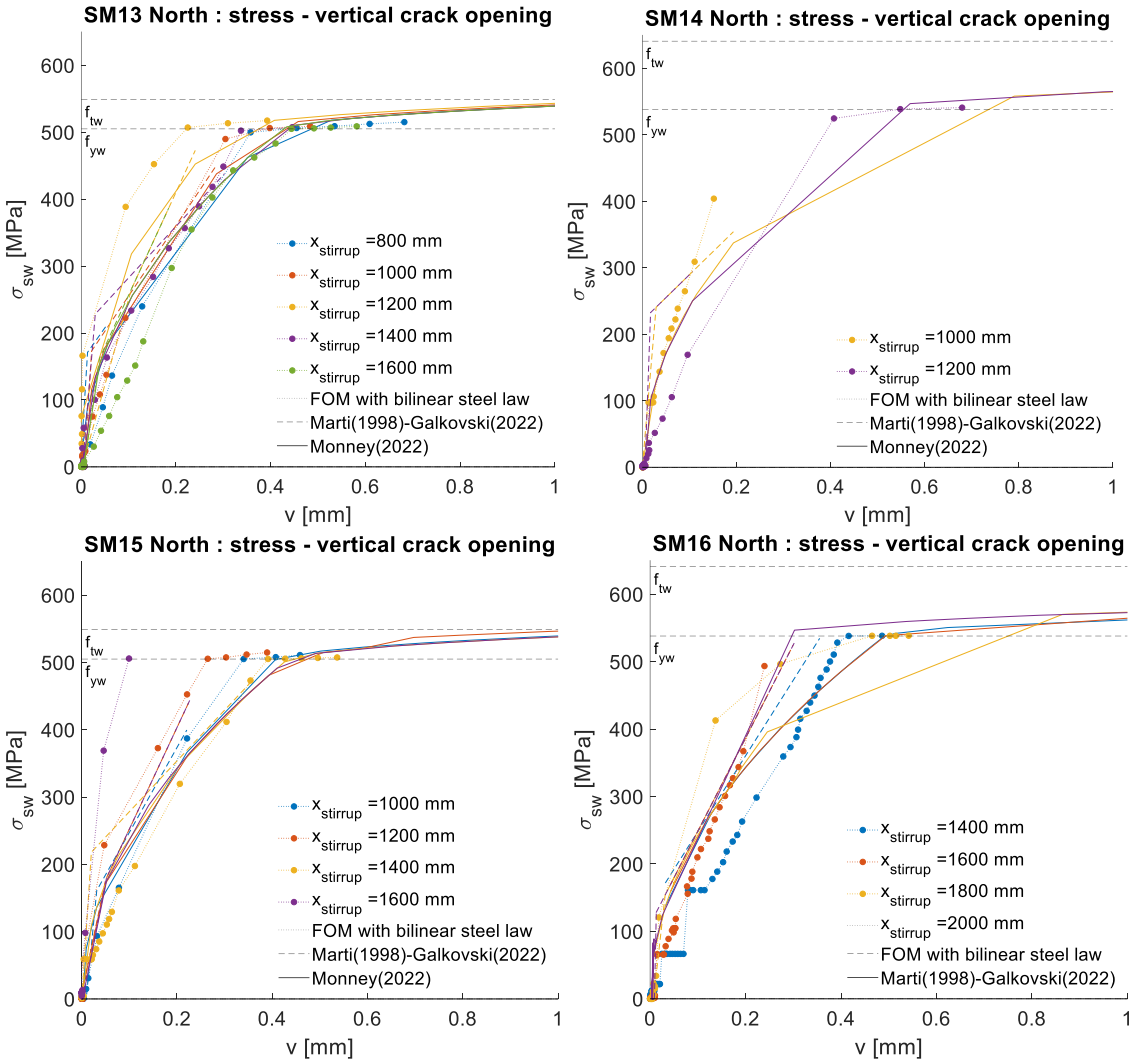

Figure 50 – Comparison of selected stirrups stress calculated by three methods: with a bilinear law from FOM strains at the crack intersection for selected stirrups with median filtering applied, after Monney (2022) [14] and after Marti (1998) [13] - Galkovski (2022) [9]. The methods are described in chapter §2.4.6.

Despite gaps between measurement points due to sudden jumps in crack opening during loading, Figure 50 shows that both methods give results that are relatively close to the FOM stresses. Marti-Galkovski's approach tends to slightly higher stress values than Monney's. The downside of Marti's approach is that it is reliably applicable until yield stress only. It should be coupled to a crack-opening to stress relation in the plastic domain to obtain a complete curve. Monney's method was selected for the present study due to its ability to capture both elastic and post-yield stress-strain behaviour.

8.1.2 Total STA evolution along the shear force

The STA described in chapter §2.4 have been implemented on the failure crack kinematics of the SM10 specimens with the methods chosen in chapter §8.1.1 for dowel and stirrups action. Figure 51 represents the calculated STA of the failure surface as a function of the actual measured load level. The mean values on both north and south faces of each specimen has been plotted. The total of all involved STA should ideally match the actual shear force applied during loading and follow the dashed line. Different initial load levels have been considered for each specimen depending on how late the failure crack develops.

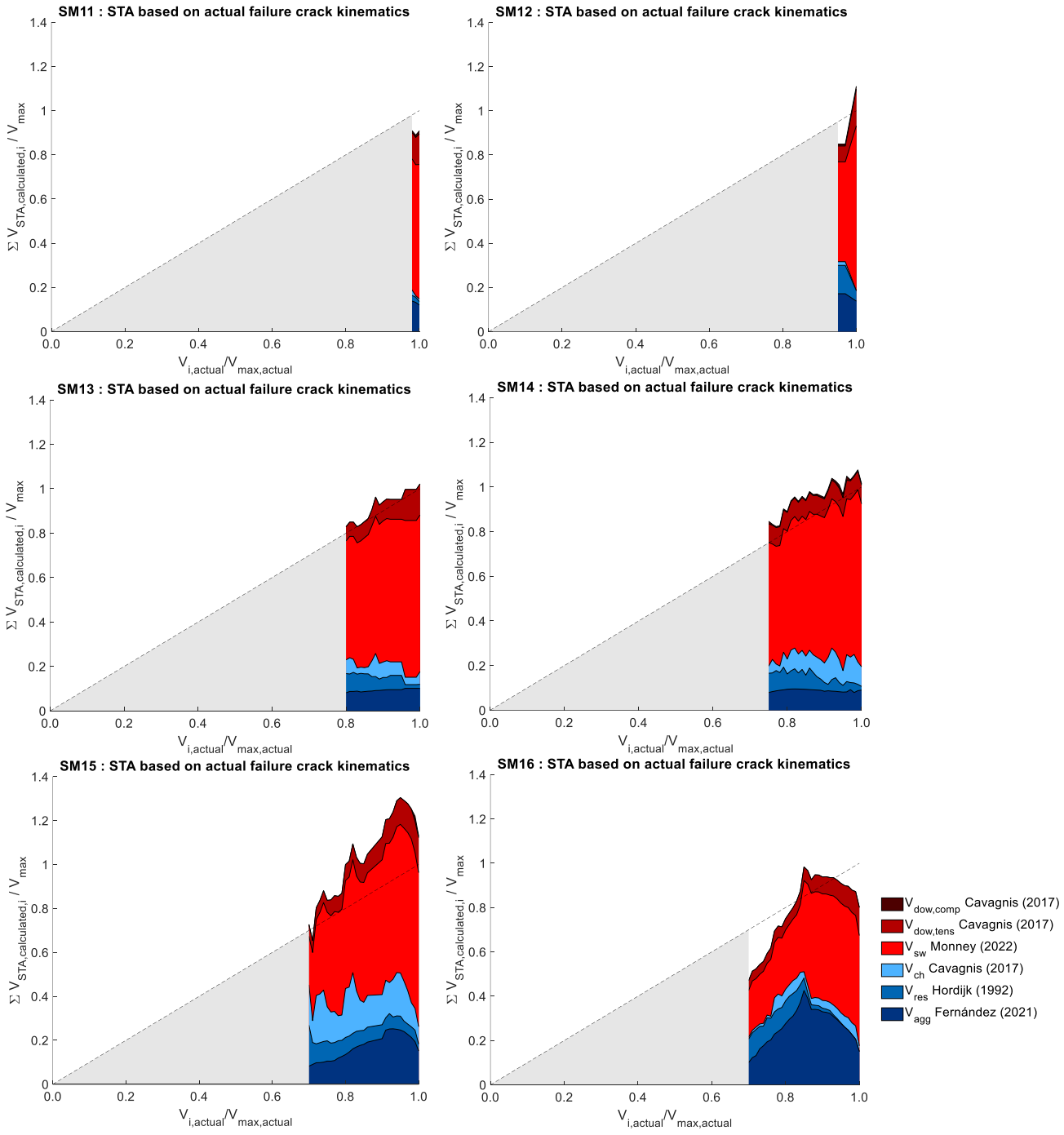

Figure 51 – SM10 (mean on both faces): calculated STA of the failure surface as a function of the actual measured load level. The greyed-out area represents the theoretical sum of the STA before DIC measurements of the failure crack are available.

Studying the evolution of the total STA could give information on the crack criticality. Indeed, when the calculated total STA starts to decrease as the actual shear force continues to augment, it means that the crack propagation becomes unstable and the specimen is therefore close to failure at this point. Figure 51 shows a decrease of the total STA for specimens SM15 at $95\%V_{max}$ and SM16 at $85\%V_{max}$. However, no such trend is observed for the other specimens. It is possible that the failure crack criticality is only observable on the total STA when its propagation is less brutal, that is with a sufficient shear reinforcement ratio. Indeed, SM15 and SM16 both have the highest shear reinforcement ratio ($\rho_w = 0.101\%$) of the SM10 series. Further STA analysis could be conducted on other specimens with higher shear reinforcement ratio to see if this is a reproducible trend and if the total STA can indeed give information on crack criticality. However, obtaining reliable predictions of the kinematics and concrete stress field to calculate the STA is challenging as stated in chapter §7. No answer to this question could be found in the present work. .

Figure 51 also gives information on the evolution of the contribution of each STA.

The dowel action of the tensed flexural reinforcements depends mainly on the location of the point where the crack intercepts the bars. Dowel action is limited if this point is located far from the support. (Cavagnis et al. (2017) [3]) This is indeed observed for specimen SM16 whose failure crack develops the farthest from the left support and has a lower dowel action relatively to other specimens. This action increases with crack opening before decreasing after the flexural reinforcements yield and deform. (López et al. (2021) [1]) As the flexural reinforcements of the SM10 specimens did not yield, dowel action is relatively important and showed a slight increase until rupture.

The dowel action of the compressed flexural reinforcements only occurs when the crack intercepts them on the North or South face or both and is negligible. Indeed, when the failure surface is close to the top surface of the beam, it is likely that the actual position of the crack bypasses the stirrups and never actually crosses the compressed reinforcements, or the stirrups as previously seen in Figure 48 (b). The surface crack measured with DIC does not necessarily correspond to the crack intercepting the stirrups, which can lead to errors and probably to an overestimation of the actual crack opening.

The contribution of the compressed chord is strongly influenced by the thickness of the compressed chord and shape of the critical crack. (Monserrat et al. (2021) [1]) It is defined by the crack tip at each load level, which makes it sensitive to the chosen criterium of $w_{min} = err_{DIC}$. In slender members with a CSC whose origin is far from the support, its contribution is limited as no direct strut between the load and the support can form. (Cavagnis et al. (2017) [3]) Figure 51 shows a small compressed chord contribution for SM16, whose failure crack origin is the farthest from the support, but also for SM11 and SM12 whose measurements are only possible very close to ultimate load. This could be due to the principal compressive strain inclination that becomes almost horizontal close to the ultimate load. (Cavagnis et al. (2017) [3]) A diminution of the compressed chord action right before ultimate load is indeed observed on most specimens. SM14 does not follow that trend and has a non-negligible compressed chord action despite its North face crack being very close to the top surface. This is compensated by its lower South face crack.

It is important to note that the accuracy of the DIC strain field is not guaranteed due to its calculation being very sensitive to noise, especially close to crack lips and surface limits. To obtain a more visually representative concrete strain field in Figure 52, the statistical outliers have been removed. Outliers are defined as values that are more than three scaled median absolute deviations (MAD) from the median. They correspond to the high strains calculated on the points neighboring cracks. The complete results for all SM10 specimens are illustrated in appendix §11.8.

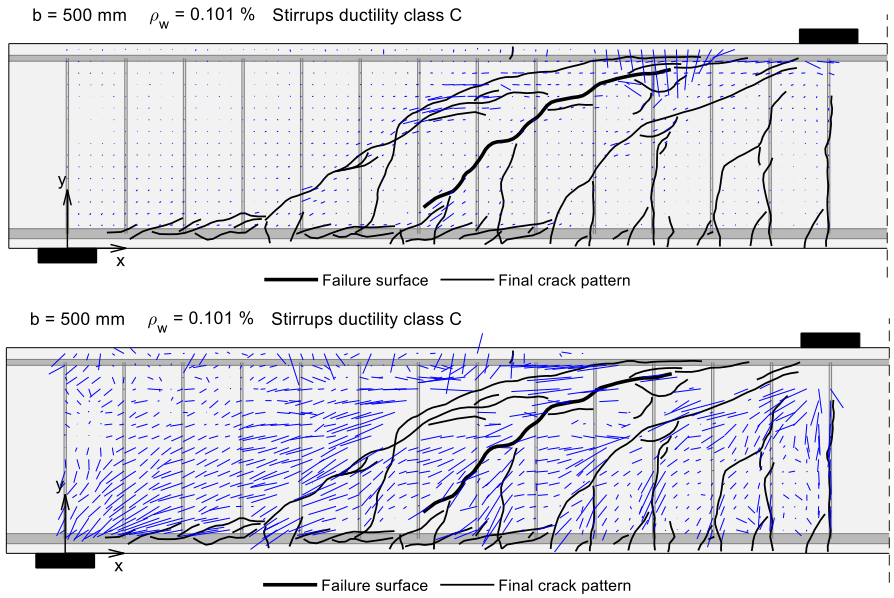

Figure 52 - SM16 North: DIC concrete strain field ε_2 at ultimate load, with (top) and without (bottom) statistical outliers

In RC members with shear reinforcements, the stirrups contribution is usually governing. (Monserrat et al. (2021) [1]) The shape of the failure surface and kinematics determines the stirrups activated and their amount of shear carried. Here again, the crack tip definition has an effect by potentially modifying the number of activated stirrups. Figure 51 shows that the stirrups action is smaller for SM16 relatively to the other stirrups. The vertical failure crack opening is not smaller than those of the other specimen, as shown in appendix §11.1.2, but the failure crack is shorter and intercepts less stirrups. It is likely that the stirrups intercepted by the two other major cracks of SM16 are also very activated. Indeed, in RC members with sufficient shear reinforcement ratio which SM16 barely has, the shear strength is not governed by the formation of a single crack localizing strains, but by concrete crushing and stirrups yielding. The stress field is more distributed, and several smaller cracks develop. (Fernández (2021) [7]) The surface crack opening detected with DIC is probably larger than the crack opening intersecting the stirrups and leads to an overestimation of the stirrups action. The stirrups considered to be activated for dowel action were removed, which lead to the diminution of the stirrups action as the load increases, which is particularly visible in Figure 51 for SM15 and SM16.

Aggregate interlock depends on crack geometry, location, and kinematics. It is particularly activated when crack slip occurs the most, usually in steeper crack portions. (Cavagnis et al. (2017) [3]) This is visible in Figure 53 as the tangential stress and normal compressive stress occur the most in the inclined portion of the failure crack. On the contrary, the quasi-horizontal segment of the failure crack almost does not contribute to the aggregate interlock action, although some perturbations at higher load levels are visible for some specimens like SM15. The complete results for all specimens are displayed in appendix §11.9.1.

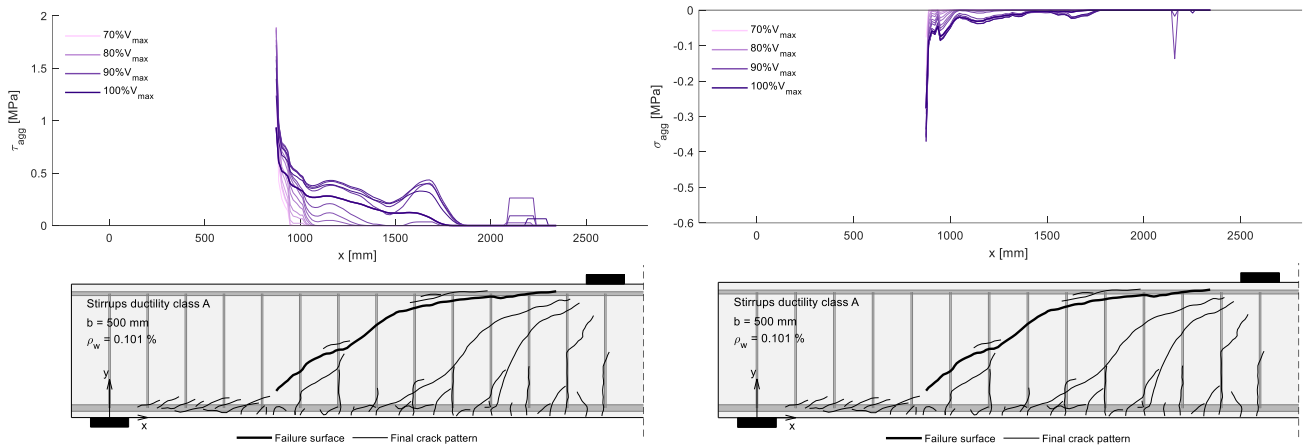

Figure 53 - SM15 North : aggregate interlock tangential stress (left) and normal stress (right) along the crack

Aggregate interlock action is often significant, particularly when the crack is steep and the crack opening low. (Cavagnis et al. (2018) [8]) Aggregate interlock decreases as the crack opening augments. This is visible in Figure 51 except for SM13 and SM14 where this action stays approximately constant. In the case of the specimens with the highest shear reinforcement ratio SM15 and SM16, where it tends to augment up to 90-95% of the ultimate load before decreasing. Aggregate interlock share is particularly important in SM15 and SM16 whose quasi-vertical segment is relatively steeper and geometrically less smooth than other specimens. Aggregate interlock contribution can vary depending on the smoothing parameter chosen for crack kinematics, as well as the minimal crack opening considered ($err_{DIC} = 0.01\ mm$).

The contribution of the residual tensile strength of concrete is most relevant for low crack openings, thus mainly in the quasi-horizontal segment of the crack as seen in Figure 54. (Cavagnis et al. (2017) [3]) The complete results of the concrete residual tensile stress along the failure surface for all specimens are displayed in appendix §11.9.2. The action of the residual tensile strength of concrete is generally not significant. (Monserrat et al. (2021) [1]) It diminishes with the load level as the crack opening augments, as seen for all specimens in Figure 51. However, the action of the residual tensile strength is extremely sensitive to the minimal crack opening considered, which was set for this action only to the maximal DIC error for each specimen. This leaves room for interpretation in the calculation of the residual tensile strength of concrete and compromises its validity. As for aggregate interlock, the smoothing parameter chosen for crack kinematics also plays a more limited role.

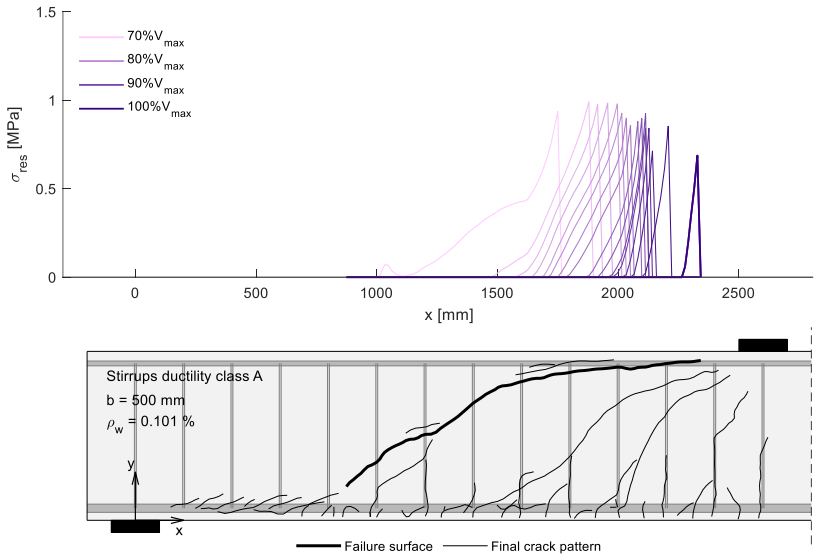

Figure 54 - SM15 North: concrete residual tensile strength normal stress along the crack

Even though the minimal crack opening considered for aggregate interlock and residual tensile strength of concrete has to be carefully selected, the shear force calculated with the total of the shear transfer action $\sum V_{STA,calculated}$ statistically follows quite well the actual load applied V_{actual} on the six SM10 specimens, as seen in Figure 55.

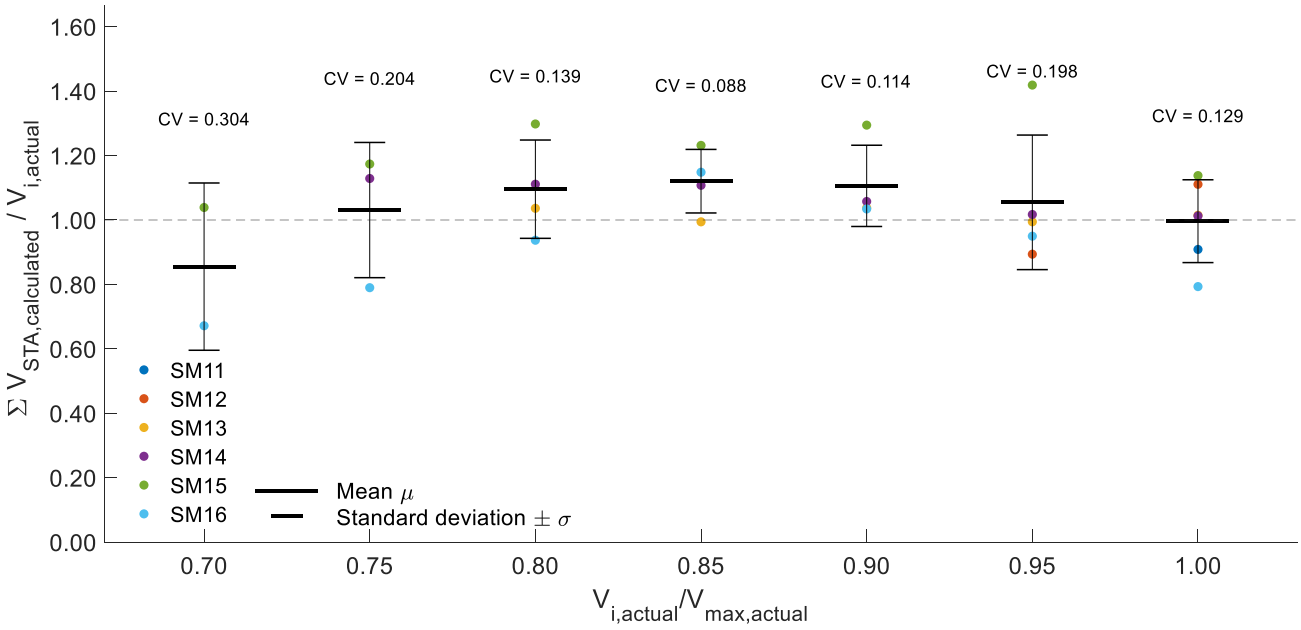

Figure 55 - SM10 (mean on both faces): statistical variability of the total calculated shear transfer actions of the failure surface as a function of the actual measured load level

The experimental results of Campana et al. (2013) [2], Cavagnis et al. (2017) [3] and Cavagnis et al. (2018) [8] showed that the relative contribution of each STA can be highly variable depending on the geometry and kinematics of the CSC. However, their sum, the total shear capacity, is relatively constant for different CSC location. This phenomenon can explain the high variability of the failure surface even for similar concrete members. It has indeed been observed on the SM10 specimens in Figure 51 that shows how variable each individual STA can be across load levels and specimens and Figure 55 that reveals how the STA sum correlates relatively well with the applied load.

8.2 Crack criticality assessment based on a load-propagation relationship

An attempt to predict the ultimate load has been conducted using the load-propagation empirical relationship of the failure surface in x-direction derived in chapter §6. Figure 56 shows the actual and predicted crack tip propagation of the failure surface in the y-axis from an initial load state displayed in Table 10. The actual crack tip propagation is defined as the last crack point where the opening is above the DIC measurement error $err_{DIC} = 0.01\ mm$. Due to the formation of delamination cracks caused by dowel action of the compressed longitudinal reinforcements, the DIC failure crack definition sometimes stops before the loading plate edge that all failure surfaces ultimately reached after failure. This phenomenon explains the gap between the actual crack tip propagation and the measured ultimate load $V_{max,actual}$ in Figure 56.

The predicted ultimate load $V_{max,predicted}$ is defined as the load where the crack tip reaches the x-coordinate of the loading plate edge. The bilinear law explained in chapter §5 was implemented to predict the failure crack geometry.

The complete results for all SM10 specimens can be found in appendix §11.7.

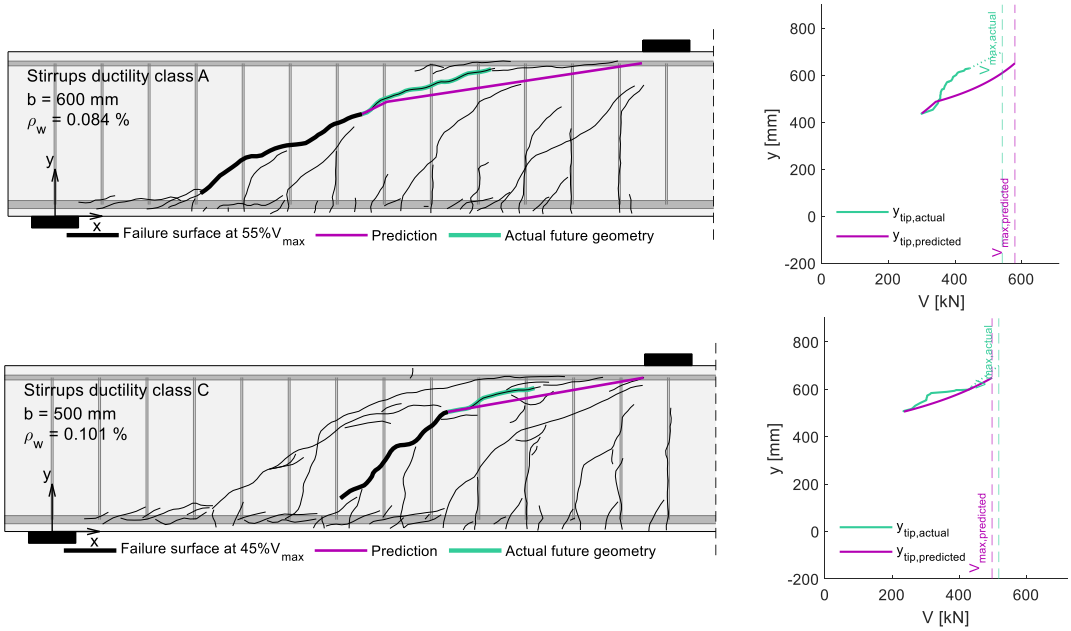

Figure 56 - SM13 (top) and SM16 (bottom) North: actual (green) and predicted (purple) vertical failure crack tip coordinate as a function of the load.

Table 10 – Actual ultimate load and predicted ultimate load based on the load-propagation empirical relationship of the failure surface in x-direction derived in chapter §6.

Specimen	SM11	SM12	SM13	SM14	SM15	SM16
$V_{initial}$ [kN]	545	537	298	354	206	233
$V_{max,actual}$ [kN]	605	597	542	644	457	518
$V_{max,predicted}$ [kN]	608	607	580	654	601	498
$\frac{V_{max,actual}}{V_{max,predicted}}$	100%	98%	93%	98%	76%	104%

Table 10 contains the ratio $V_{max,actual}/V_{max,predicted}$ for the load-propagation relationship. Although most predictions show under 5% difference with the actual ultimate load, this is not the case for SM15 shown in Figure 57. No apparent reason has been found to explain the difference calculated on this specimen. This casts doubt on the validity of the experimental load-propagation relationship, which as discussed in chapter §6 is based on a rather small test sample and is probably highly subjected to the variability of experimental strength.

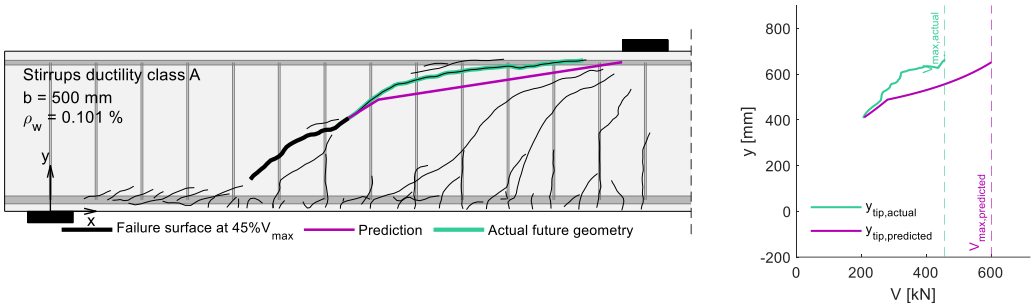

Figure 57 – SM15 North: actual (green) and predicted (purple) vertical failure crack tip coordinate as a function of the load.

9 Limitations of nonlinear finite element analysis in beams with low shear reinforcement ratio

This section aims to understand NLFEA limitations in RC elements with localised cracking, such as the SM10 and SM00 specimens with low shear reinforcement ratio described in chapter §3. NLFEA consider a continuous medium and perfect bound between concrete and reinforcements, which do not correspond to the real cracked state of concrete. NLFEA is in practice generally applied to RC elements with well-distributed and sufficient steel reinforcements, so that smeared cracking can occur. These elements are often prestressed and non-rectangular, such as I- or T-shaped beams for example. The SM10 specimens are unusual cases with which difficulties are likely to be encountered when calculating their shear strength using NLFEA.

9.1 Modeling and material laws

The SM10 and SM00 specimens were analysed using A 2D non-linear finite element modelling program named jconc. It was developed at the Structural Concrete Laboratory IBETON (EPFL) by Dr Miguel Fernández Ruiz and enhanced by Dr Olivier Burdet.

The program considers 1D steel reinforcement bars bearing no transversal load or bending moment with perfect bound assumed. Steel can be modelled with elastic-plastic material behaviour with or without hardening as displayed in Figure 58 (a) depending on the jconc version used.

NLFEA calculations have not been conducted for specimens with ductility class A stirrups due to the elastic-plastic material law being too unrealistic for steel that breaks at low strain. Only the specimens containing ductility class C stirrups with properties listed in Table 11 have been analysed. The other steel types properties are found in chapter §3. The concrete compressive strength considered was the mean value on all specimens, $f_c = 50.0\ MPa$ for the SM10 series and $f_c = 40.5\ MPa$ for SM00 respectively. For both test series, the concrete Young modulus was set as $E_c = 38700\ MPa$.

Table 11 - SM10 and SM00 : material properties of the ductility class C stirrups

Stirrups material properties	Ductility class	f_{yw}	f_{tw}	ε_{uw}	E_{sw}	E_{hard}
SM10 Ø 8mm	C	538 MPa	641 MPa	9.0%	189507 MPa	1182 MPa
SM00 Ø 6mm	C	516 MPa	608 MPa	7.5%	200000 MPa	1270 MPa

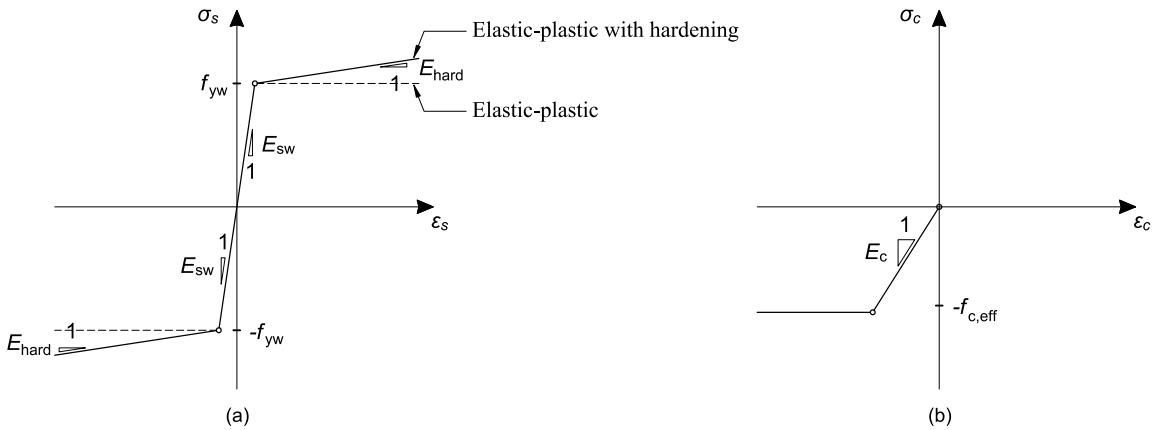

Figure 58 – Material constitutive laws adopted in jconc NLFEA : (a) steel reinforcements; (b) concrete

Concrete is a quasi-brittle material with a low tensile strength that makes it susceptible to cracks. Adding steel reinforcements to concrete greatly enhances its strength and ductility for various structural applications. However, the deforming reinforcement induce tensile strains in the surrounding bounded concrete, causing smeared cracking. The concrete compressive strength therefore needs to be reduced as a consequence of material softening caused by imposed transversal strains.

Vecchio and Collins (1986) [24] proposed within the Modified Compression Field Theory (MCFT) one of the most used expressions of the concrete compression-softening law with a softening factor η_ε applied on the concrete compressive strength f_c:

$$\eta_\varepsilon = \frac{1}{0.8 + 170 \cdot \varepsilon_1} \leq 1.0 \qquad (60)$$

Jconc considers the concrete effective compressive strength $f_{c,eff}$ as a function of the softening factor according to MCFT. The 2D concrete elements can only bear compressive strength as displayed in Figure 58. Furthermore, jconc considers the concrete as a continuous medium and no aggregate interlock is taken in account.

Vecchio and Collins (1986) [24] semiempirical relation (60) accounts for the cracked state of concrete, but do not consider the various failures modes (concrete crushing, spalling or sliding) sketched in Figure 59. Knowing the governing failure mechanism is crucial for analyzing the strength of a RC element. (Niketić F. (2017) [19]) The SM10 specimens were typically subjected to a sliding failure mechanism.

Self-weight is also not considered in jconc, but its share is negligible compared to the ultimate load. The reaction at the left support caused by the self-weight of the beam was 25.1 kN for SM12, 18.5 kN for SM14 and 15.6 kN for SM16, which amount to maximum 4% of the actual ultimate load.

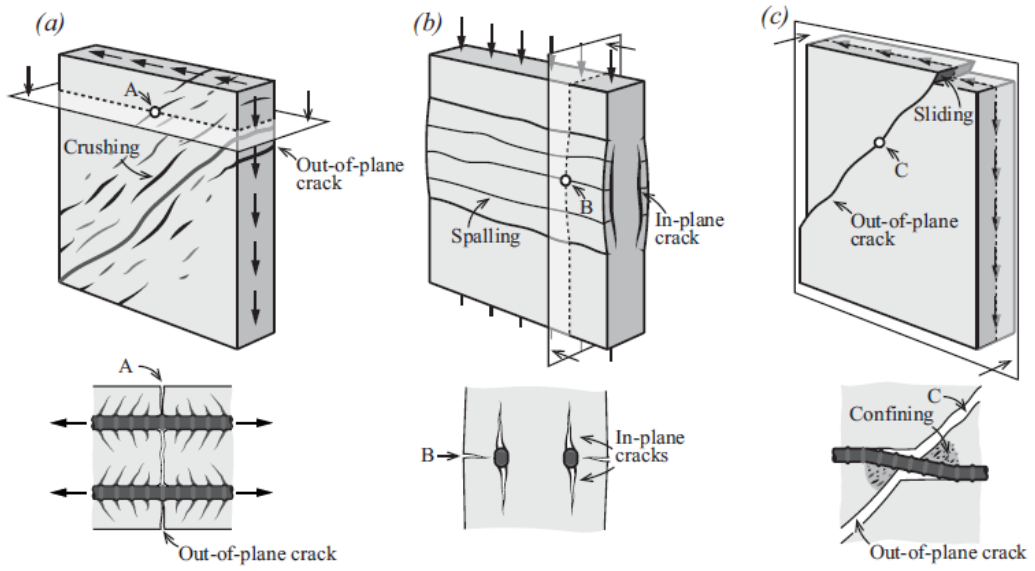

Figure 59 – Failure mechanism of reinforced concrete panels: (a) concrete crushing; (b) concrete cover spalling; (c) concrete sliding. Niketić (2017) [19]

Niketić (2017) [19] stated in his PhD thesis the influence of FE size on NLFEA results, with smaller FE leading to lower shear strength regardless of the shear reinforcement ratio. He recommended a maximum element size so that two concrete triangles could fit in the stirrups spacing. Skewed FE and local mesh refinement should be avoided if possible.

The three different meshes in Figure 60 and Figure 61, respectively for SM10 and SM00 specimens, have been analysed in the present study. Two of them, (a) and (b), are based on a rectangular grid adapted to the reinforcements position, and the last one, (c), is automatically generated by iMesh, a program that optimizes the triangle elements to make them as equilateral as possible. To avoid a small number of FE over the section's height and very slender concrete cover elements, a minimum of four triangle elements have been placed between each stirrup for the rectangular grid mesh (a) and (b).

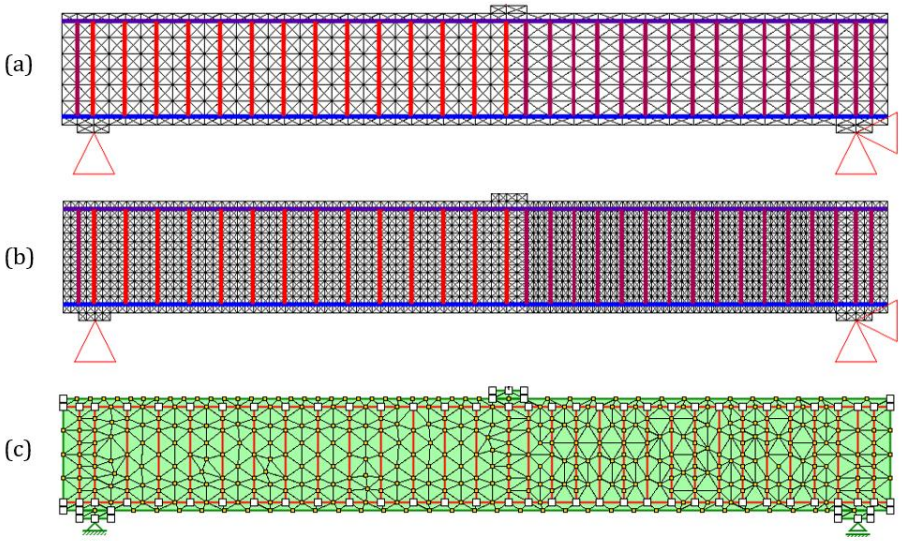

Figure 60 – SM10: (a) Original mesh e/s=0.50; (b) denser mesh e/s=0.25; (c) iMesh mesh

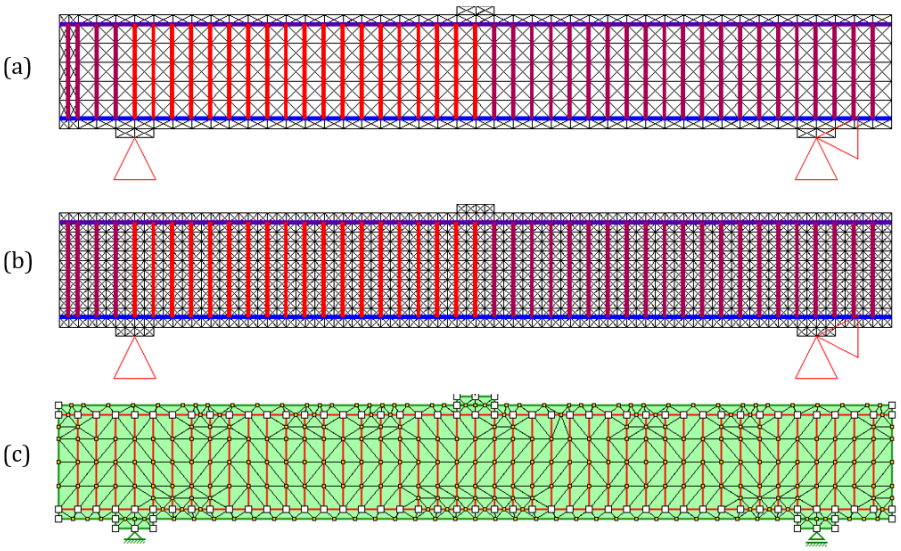

Figure 61 – SM00: (a) Original mesh e/s=1.00; (b) denser mesh e/s=0.50; (c) iMesh mesh

9.2 Results

9.2.1 SM10 and SM00 specimens

The NLFEA calculated shear strength of the SM10 and SM00 specimens with class C stirrups are listed in Table 12. Different programs and jconc versions have been compared, such as jconcc and iMesh without considering steel hardening, as well as jconc1.10 and EvalS with consideration of the steel hardening. The NLFEA calculated shear strength $V_{max,NLFEM}$ corresponds to the highest shear force applied with a precision of ± 5 kN leading to numerical convergence of 250 iterations.

Table 12 – Sectional shear strength calculated using jconc $V_{max,NLFEA}$ and measured maximal shear force $V_{max,actual}$ with $V_{max,actual}/V_{max,NLFEA}$ ratio in red.

Specimen			SM12	SM14	SM16	SM02	SM04
Shear reinforcement ratio ρ_w			0.063 %	0.084 %	0.101 %	0.113%	0.113%
Width b_w [mm]			800	600	500	250	250
Anchorage type			-	-	-	Head	Bend
Measured maximal shear force $V_{max,actual}$ [kN]			597	644	518	286	269
Calculated shear strength $V_{max,NLFEA}$ [kN]	Elastic-plastic steel law	jconcc original mesh	843 0.71	728 0.88	660 0.78	290 0.99	290 0.93
		jconcc denser mesh	737 0.81	623 1.03	587 0.88	250 1.14	250 1.08
		iMesh mesh	847 0.71	710 0.91	613 0.85	298 0.96	298 0.90
	Elastic-plastic steel law with hardening	jconc1.10 original mesh	847 0.71	733 0.88	664 0.78	290 0.99	290 0.93
		EvalS original mesh	845 0.71	721 0.89	660 0.78	285 1.00	285 0.94

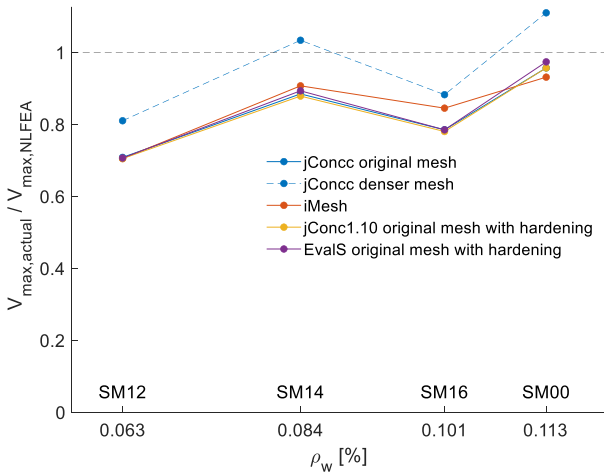

Figure 62 – Actual over NLFEA calculated shear strength ratio as a function of the shear reinforcement ratio. The mean value of $V_{max,actual}$ of SM02 and SM04 was considered for the SM00 model.

Figure 62 graphically represent the ratio of the actual ultimate load measured during experiments $V_{max,actual}$ to the NLFEA calculated shear strength $V_{max,NLFEM}$. Overall, NLFEA results overestimate the shear strength, especially for specimens with lower shear reinforcement ratios.

The sawtooth shape of this Figure 62 curves is due to the experimental variability of $V_{max,actual}$ visible in the actual measured normalized ultimate load in Figure 63. The ultimate load measured for SM14 is likely on the higher side of the statistically expected range, when that of SM16 is on the lower side. The curves should theoretically be positively correlated in Figure 62. The calculated shear strength using

jconc usually present more accurate results for RC beams with a higher shear reinforcement ratio at least above the minimal value $\rho_{w,min} = 0.1\%$ required by SIA 262 standard (2013).

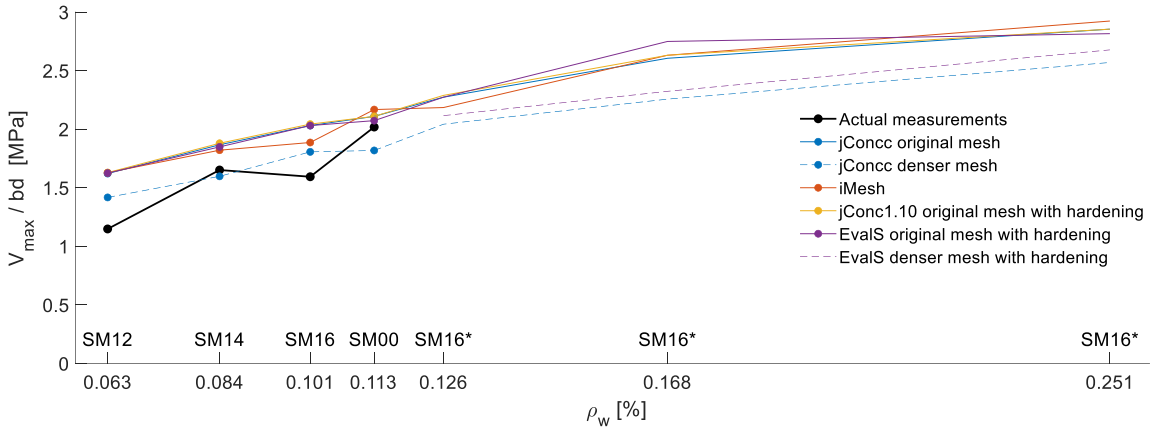

Figure 63 – Actual and NLFEA calculated shear strength normalized by width and statical height of the specimens as a function of the shear reinforcement ratio

Figure 63 shows the normalized shear strength for the SM10 and SM00 ductility class C specimens. Dummy variants of SM16 specimens with decreasing section width were created to showcase higher shear reinforcement ratios even if no measured shear strength is available for comparison. The longitudinal reinforcement ratio was kept identical, as was the case for the SM10 series. The difference between the results of the original and denser mesh remains approximately constant for higher shear reinforcement ratios.

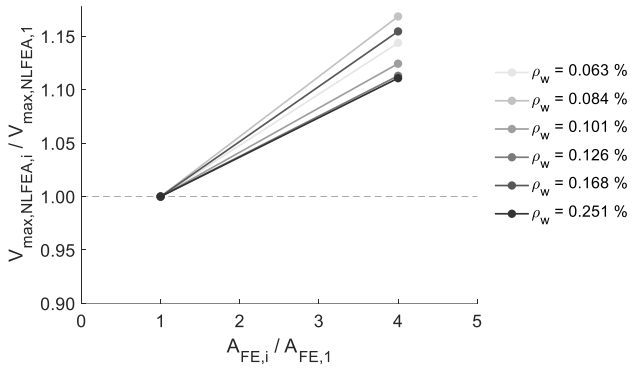

Figure 64 - jconcc mesh size sensitivity for varying shear reinforcement ratios

These results show that the most sensitive parameter for the studied specimens is the mesh, particularly the mesh size. Indeed, different programs gave very similar results for identical meshes. The approximatively equilateral mesh generated by iMesh resulted in similar results than the original mesh, except for SM16 where it is closer to the denser mesh. The strength augmentation linked to steel hardening consideration is very limited for the original mesh, though seemingly more visible with the denser mesh. As observed by Niketić (2017) [19] on a I-shaped beam under beam under four-point-bending, Figure 64 shows that the denser mesh consistently gives lower NLFEA calculated shear strengths.

However, concrete damage localisation has been frequently found in the tested models. Localisation is a known problem of non-linear finite elements and can cause a numerical convergence problem. For instance, concrete cover spalling has been detected for the original mesh of specimens with a shear reinforcement ratio higher than $\rho_w = 0.1\%$. The longitudinal reinforcements geometry forces slender concrete elements in the concrete cover of the original mesh, which could exacerbate this issue. For the denser mesh and specimen SM12 and SM14, the lowest concrete softening factor was encountered in

the compression struts next to the left support. The different governing failure mechanism complicates the comparison between specimens and meshes.

Another concrete damage localisation seen in Figure 65 also seemed to occur in a vertical section next to the loading plate, although it is never the minimal softening factor. This could be due to the lack of longitudinal reinforcement distributed over the height of the section, which are in present in practice but not on the SM10 and SM00 experiments. NLFEA failure due to concrete localisation could also explain the small influence of steel hardening consideration obtained in the calculated shear strength.

Figure 65 also highlight localisation along the mesh diagonal starting at the bottom of the stirrups. It becomes more pronounced for increasing shear reinforcement ratios and decreasing mesh element sizes. Although the denser mesh overall leads to more smeared stress and damage distribution, it is not always guaranteed to reduce localisation problems as seen for specimen SM16* with $\rho_w = 0.251\%$. It shows than in addition to the importance of the FE size choice, the mesh orientation can also influence NLFEA results. This could have resulted in lower calculated shear strength due to stress and damage localisation in the concrete elements along the preferential fracture planes. This could explain the remaining gap between the original and denser mesh results of Figure 63 even for higher shear reinforcement ratios. Indeed, Niketić F. (2017) [19] showed that NLFEA results stability depends on the failure mechanism.

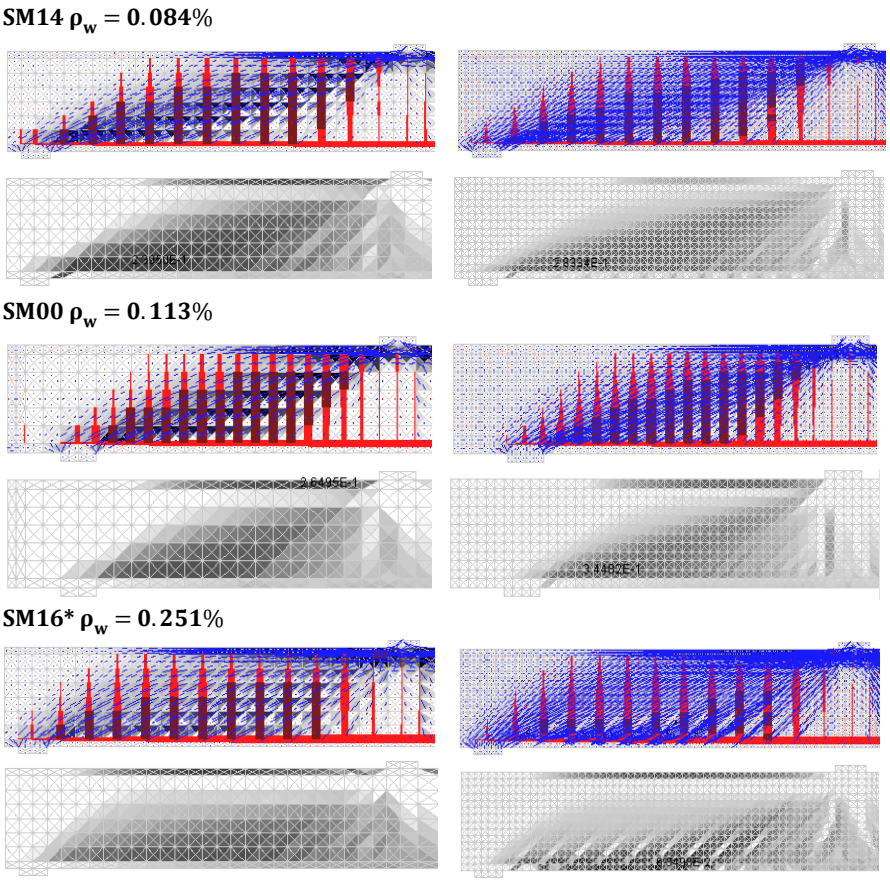

Figure 65 - Jconcc stress field and concrete softening factor with original mesh (a) and denser mesh (b)

When comparing the jconc stress fields and softening factor distributions with the actual cracking pattern in Figure 66, a clear analogy cannot be observed. The DIC strain field in Figure 67 shows that it is actually disturbed by the cracking pattern, as the most significant compressive strains are located above the cracks and oriented parallel to them. Rupf (2014) [22] indeed stated that NLFEA was not suitable to beams which comprise large crack openings, and that such cases should consider an adapted stress field around the discontinuities.

The NLFEA stress field and damage pattern is smeared with the most intense concrete compressive stress located and oriented along the diagonal between the loading plate and the support.

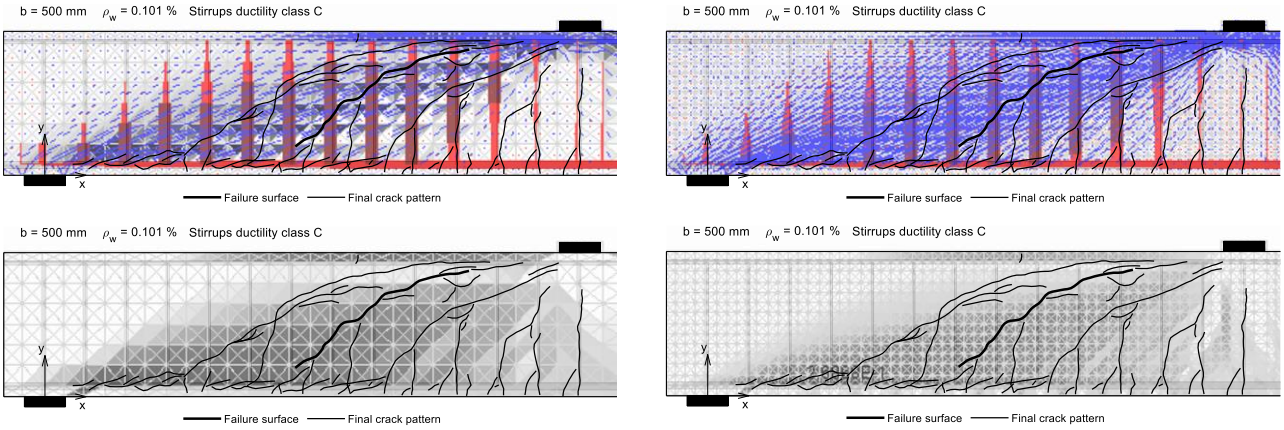

Figure 66 - SM16: jConcc stress field and concrete softening factor for the original mesh (a) and denser mesh (b)

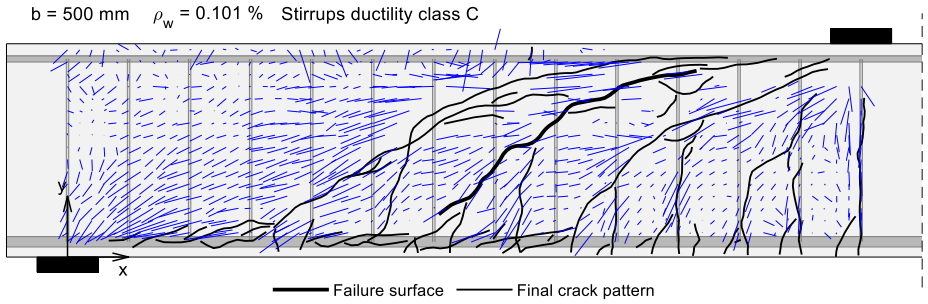

Figure 67 - SM16 North: DIC concrete strain field

The jconc stirrups strain can also be compared to the FOM actual measurements in Figure 68 on which median filtering was applied (see chapter §8.1.1.2). The difference is striking, even if most FOM measurements are lost approaching ultimate load. NLFEA strains are distributed over the whole height of the stirrups with maximal values at the bottom, while stirrups are actually activated only when a crack intersects them. If the specimens had a perfect smeared cracking with very low spacing, the actual strains would actually come closer to the jconc calculated ones. This becomes the case when the shear reinforcement ratio is higher.

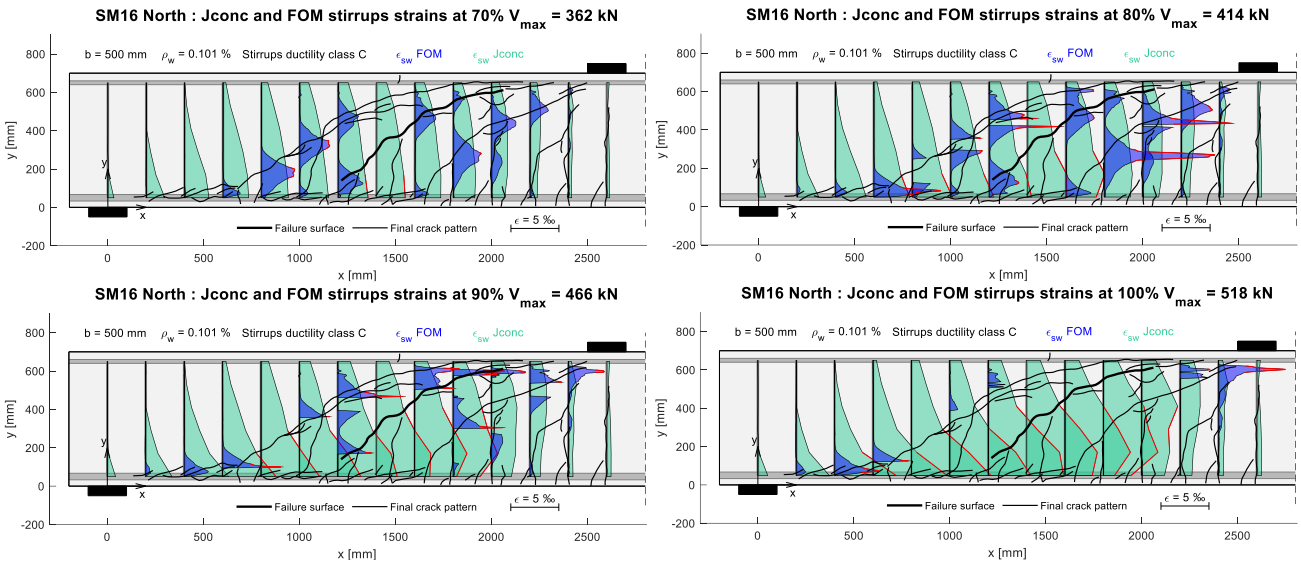

Figure 68 – SM16 North: Comparison between jconc strains with original mesh and FOM strains with median filtering applied. The values over yield strain are highlighted in red.

Highlighting such major differences between NLFEA stress fields and strains and the actual measurements allow for a better comprehension of the calculated shear strength error. The real rupture does not occur due to concrete crushing in the compressions struts considered by the model, but rather by stirrups and aggregate interlock rupture inside the failure crack. The force transmission mechanism considered in NLFEA clearly differs from reality.

Dowel action is another element not considered with NLFEA. However, the FOM calculated values of the dowel action of the longitudinal reinforcements displayed in Table 13 show that its contribution at ultimate load amounts to up to almost 20%$V_{max,actual}$ for specimens with a lower shear reinforcement ratio. On the other hand, the stirrups dowel action was not significant up to optical fiber rupture. NLFEA tends to overestimate the shear strength, even without accounting for dowel action.

Table 13 - Dowel action of the tensed flexural reinforcement at the failure surface based on FOM at ultimate load V_D [kN]

SM11	SM12	SM13	SM14	SM15	SM16
119	116	82	39	48	20

Niketić F. (2017) [19] drew attention to the possibility of obtaining unrealistically low concrete softening factors η_ε on concrete elements with no adjacent rebars. The tensile strength of concrete elements is not considered in jconc, which can lead to exaggerated deformations. This phenomenon could explain the higher instances of localisation for the denser mesh in Figure 65. Niketić advised to control them by smearing the reinforcement so that every concrete element is adjacent to a bar element.

In an attempt to improve NLFEA results by reducing the occurrence of localisation, new models have been derived from the SM00 with original and denser mesh. A first variation was created by removing the concrete cover to avoid numerical divergence caused by its delamination. A second variation was modelled with smeared stirrups according to the recommendation of Niketić F. (2017) [19].

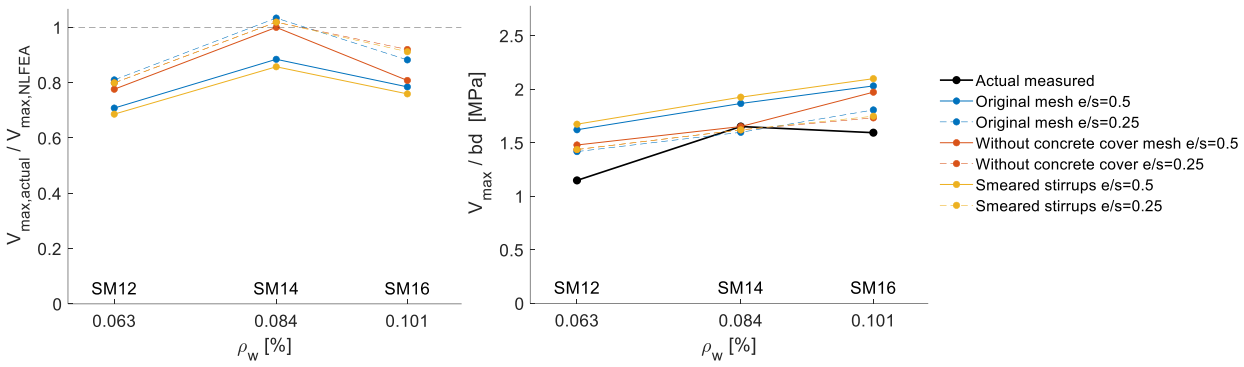

Figure 69 – SM10 with or without concrete cover and smeared stirrups: actual to NLFEA calculated shear strength ratio (left) and NLFEA calculated shear strength normalized by width and statical height of the specimen (right)

Figure 69 shows that the calculated NLFEA strength is systematically lower for the models without concrete covers with both mesh sizes. If the top localisation due to concrete cover spalling disappeared, as seen in Figure 70, the 50mm concrete cover probably contributes non-negligibly in the case of the SM10 specimens as it constitutes 15% of the total section height of 700mm, leading to a lower calculated shear strength.

Smearing the stirrups did not have a significant effect on the results, even if Figure 70 (b) shows that it reduced the denser mesh localisation between the stirrups. This confirms that the issue of uncontrolled concrete FE between the stirrups was not governing in the original models, and that the failure occurred by crushing of the concrete next to the support.

Without concrete cover

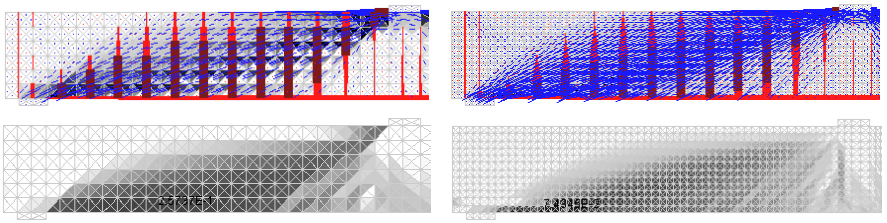

(a) (b)

Smeared rebars

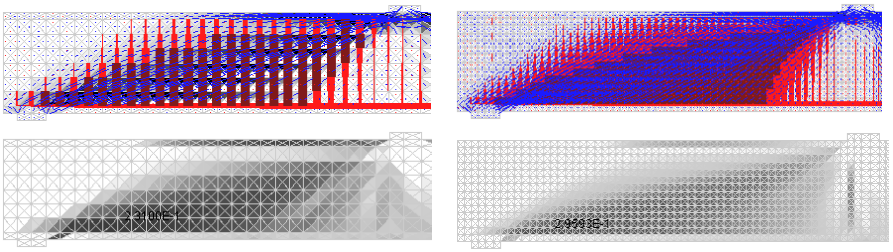

(a) (b)

Figure 70 – SM14: jconc stress field and concrete softening factor with original mesh (a) and denser mesh (b)

9.2.2 Comparison with usual practical cases

In practice, NLFEA such as jconc are often used for prestressed sections. Figure 71 shows that adding horizontal compressive stress on the specimen SM10 results in a convergence of the calculated NLFEA shear strength of both mesh sizes, as expected in literature for most usual NLFEA cases. (Niketić F. (2017) [19])

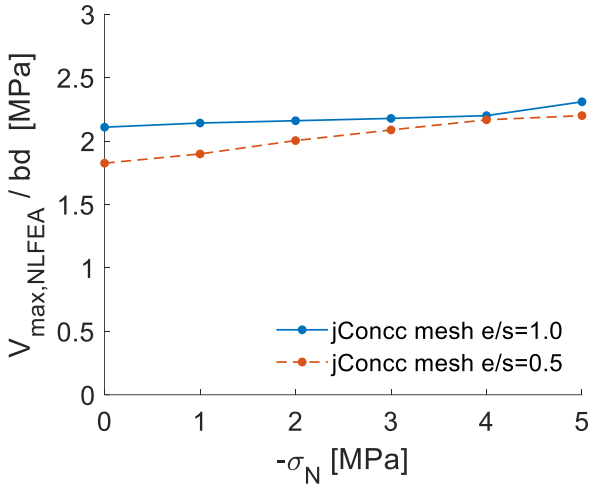

Figure 71 – SM00 prestressed: NLFEA calculated shear strength normalized by width and statical height of the specimen

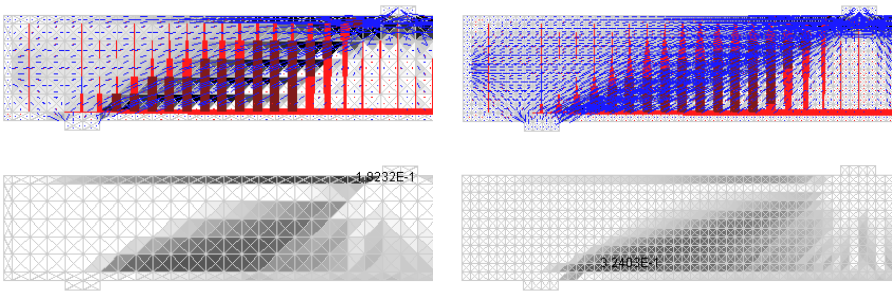

(a) (b)

Figure 72 – SM00 with prestressing: jconc stress field and concrete softening factor with original mesh (a) and denser mesh (b)

In a second phase, the geometry of specimen SM00 has been modified as illustrated in Figure 73 to include flanges of different width ($1 \leq b_{tot}/b_w \leq 3$) to test its influence on mesh size sensitivity.

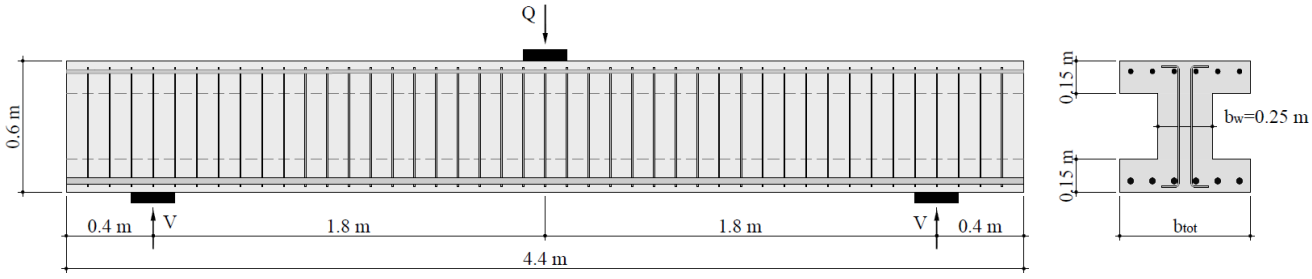

Figure 73 - SM00 with flanges : geometry and reinforcements layout

However, it should be noted that the flanges height is constrained to match the original mesh grid, which results in an unrealistic I-shaped section. The web is composed of only 6 triangle FE in the original mesh, when about 10 FE would be advised to obtain reliable results. This could influence the calculated shear strength and lead to the increasing difference between the two meshes in Figure 74, as opposed to the trend discovered with prestressing in Figure 71.

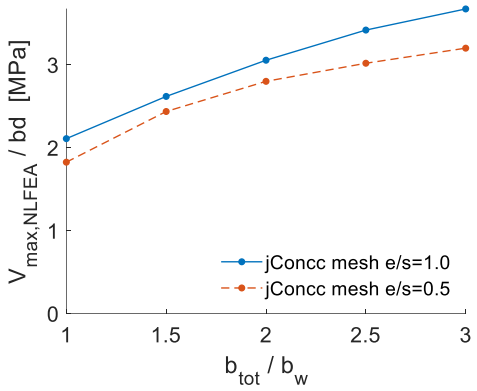

Figure 74 – SM00 with flanges: NLFEA calculated shear strength normalized by width and statical height of the specimen

Delamination between the web and the bottom flanges is observed for the denser mesh. The original mesh has an unrealistic damage pattern (Figure 75), which suggest that the FE size could be too large for this modified geometry.

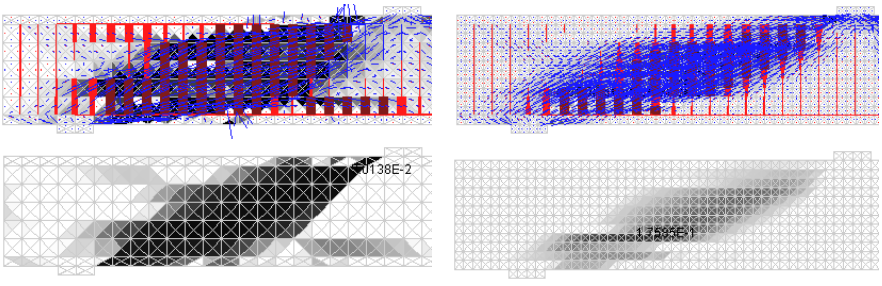

(a) (b)

Figure 75 - SM00 with flanges: jconc stress field and concrete softening factor with original mesh (a) and denser mesh (b)

10 Conclusions

10.1 Crack kinematics predictions

Despite several attempts, obtaining reliable predictions of the failure crack kinematics in RC members with shear reinforcements has proven unsuccessful in the present work and the question remains open.

The failure crack rotation increment used in the method presented by Hugo Nick in his Master thesis (2023) [17] proved difficult to predict as it presents a high variability. An average constant rotation increment was calculated from the kinematics measurements between an initial load level and the ultimate load, but no link between the values obtained and the characteristics of the specimens or crack shapes could be found. The kinematics predictions obtained with the calculated constant rotation increment did not correspond to the actual kinematics distribution along the crack, whether with a large or small propagation increment.

In a second attempt to predict the failure surface kinematics, a single horizontal propagation increment was applied to the crack tip in a given initial state. To avoid the need to determine the crack rotation, which has been unsuccessful, relations on the horizontal crack opening u have been derived to predict the kinematics after a single propagation increment.

However, the predicted kinematics obtained didn't match either. Indeed, the presence of secondary cracks, particularly the connected ones, strongly influence the failure surface kinematics and create a complicated deformation scheme. The study of the rotation of the compressed chord relative to an uncracked concrete portion below the CSC strongly challenged the rigid-body hypothesis. Although valid in the case of RC members without shear reinforcements, the presence of stirrups seems to invalidate this hypothesis. Indeed, the portion of the concrete compressed chord above the CSC quasi-horizontal portion is subjected to local flexural and shear deformations. A bulging in the relative rotation curves started to occur on some specimens as the load progresses. This could be due to the formation of delamination cracks around the compressed flexural reinforcement and could be used as an indicator of imminent failure.

The kinematics study concluded that the concrete on either side of the failure crack do not behave as rigid bodies but form several articulations with local flexion. The many degrees of freedom created by the presence of stirrups results in a highly variable behaviour that is difficult to predict even with a relatively small propagation increment. Multiple hypotheses valid for RC members without shear reinforcement are therefore challenged in the presence of stirrups, even with low shear reinforcement ratios.

Despite the differences in behaviour noted, the linear profile of the sum of the horizontal crack opening for the cracks tributary to the CSC presented by Cavagnis et al. (2018) [8] for RC members without shear reinforcement is still approximately observed for the SM10 specimens with low shear reinforcement ratios.

10.2 Criticality assessment

Studying the STA revealed a high sensitivity of the residual tensile strength of concrete after Hordijk (1992) [12] to the minimal crack width considered, and by extension the DIC error. This was also the case to a lesser extent for aggregate interlock after Fernández (2021) [7]. This parameter should be carefully selected, and further research could be conducted to better understand its application for the residual tensile strength of concrete in different cases.

Even though the individual STA show variability across load levels and specimens, the statistical analysis of the STA sum of the failure cracks of all SM10 specimens demonstrates that it follows the applied load relatively closely.

The evolution of the total STA along the load for the two specimens with the highest shear reinforcement ratio showed that the STA sum reached a maximum around 90% of the ultimate load before decreasing mostly due to the decay of the aggregate interlock action and the concrete residual tensile strength of concrete. This could indicate that the crack propagation becomes unstable at this point. The crack criticality could theoretically be predicted if reliable kinematics predictions were available but obtaining such prediction has been proven challenging in the present project.

The STA sum of other specimens however increased almost monotonically until failure. It is possible that the failure crack criticality is only observable on the total STA when its propagation is less brutal, that is with a sufficient shear reinforcement ratio. Further STA analysis could be conducted on other specimens with higher shear reinforcement ratio to see if this is a reproducible trend and if the total STA can indeed give information on crack criticality.

The FOM in the rebars were used to compare the STA models considered for dowel action and stirrups contribution. However, it should be noted that the resulting strain data is highly detailed but very noise-sensitive if the rebars yield, which was the case for several stirrups in the SM10 specimens. The stirrups measurements were often lost before ultimate load.

10.3 Load-propagation empirical relationship

An approximately linear relationship has been found between the coordinate of the failure crack tip in the direction perpendicular to the load (x-direction) and the ratio of the bending moment calculated in the section located at the crack tip M_{tip} to the cracking moment $M_{cracking}$. This trend has been detected on both tests sets SM10 and SM00. The slopes of the linear relationship seem to be proportional to the square of the shear reinforcement ratio. Despite the variability on the actual crack propagation, the proposed load-propagation empirical law offers an estimation that captures the general trend. However, since these observations are based on RC beams with shear reinforcements transversely loaded by a fixed-point force, it is possible that the validity of the load-propagation relationship is limited to the specific experimental conditions of the SM10 and SM00 series.

An attempt to predict the ultimate load has been conducted using this load-propagation empirical relationship. Although most predictions show under 5% difference with the actual ultimate load, this was not the case for one specimen, with no apparent reason to explain the difference calculated on this specimen, casting doubt on the validity of this approach that is based on a rather small test sample and is probably highly subjected to the variability of experimental strength.

10.4 Nonlinear finite element modeling

NLFEA have also been used to predict the ultimate load of the SM10 and SM00 specimens. Overall, NLFEA results overestimate the shear strength, especially for specimens with lower shear reinforcement ratios. The analysis demonstrated that the most sensitive parameter influencing the calculated shear strength is the mesh, particularly the mesh size. A denser mesh consistently gives lower NLFEA shear strengths for the tested specimens.

Localised concrete damage causing a numerical convergence problem was a recurring occurrence in the different models tested. This is a known problem of non-linear finite elements. Indeed, concrete cover spalling has been detected, as well as damage localisation in the concrete between stirrups along straight mesh diagonals. It showed than in addition to the importance of the FE size choice, the mesh orientation can also influence NLFEA results. Although the denser mesh overall lead to more smeared stresses and damage distribution, it did not always guarantee to reduce localisation problems, especially if straight fracture planes can occur in a regular grid mesh configuration. A more random mesh pattern, such as the one generated by iMesh is more suitable to this regard.

In addition, major differences have been highlighted between NLFEA stress fields and strains and the actual measurements. Indeed, the real rupture do not occur due to concrete crushing in the compressions struts considered by the model, but rather by stirrups and aggregate interlock rupture inside the failure crack. The force transmission mechanism considered in NLFEA clearly differs from reality. NLFEA strains are distributed over the whole height of the stirrups with maximal values at the bottom, while stirrups are actually activated only when a crack intersects them. If the specimens had a perfect smeared cracking with very low spacing, the actual strains would actually come closer to the NLFEA calculated ones. Those observations allow for a better comprehension of the calculated shear strength error of NLFEA analysis for RC members subjected to localised cracking. The differences between NLFEA results and actual measurements could stem from several causes, such as the neglected concrete tensile strength, the perfect bound considered between concrete and reinforcements, or RC treated as a continuous medium.

In all cases, mesh sensitivity analysis is crucial in NLFEA. Its importance could be overlooked by inexperienced users, and critical reconsideration of NLFEA results is necessary to prevent errors. This is especially true with RC structures that are outside of the common type studied with NLFEA, that is in practice often non-rectangular prestressed sections with sufficient shear reinforcements. The localised cracking of SM10 specimens is one of the worst application case possible for NLFEA. The results may considerably differ from the actual ultimate load, as observed in the present study, and should be analysed with a critical mind.

11 Appendixes

11.1 Failure surface actual kinematics

11.1.1 Horizontal crack opening u

The actual kinematics have been represented for each specimen from 70% to 100% of the ultimate load with a load level spacing of 2%.

Stirrups ductility class A

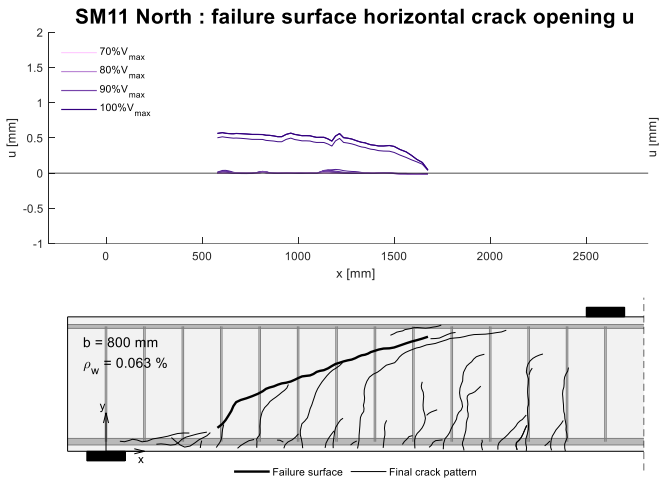

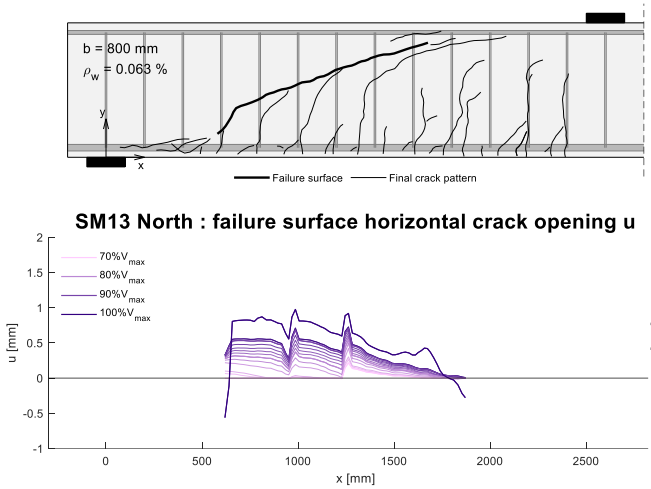

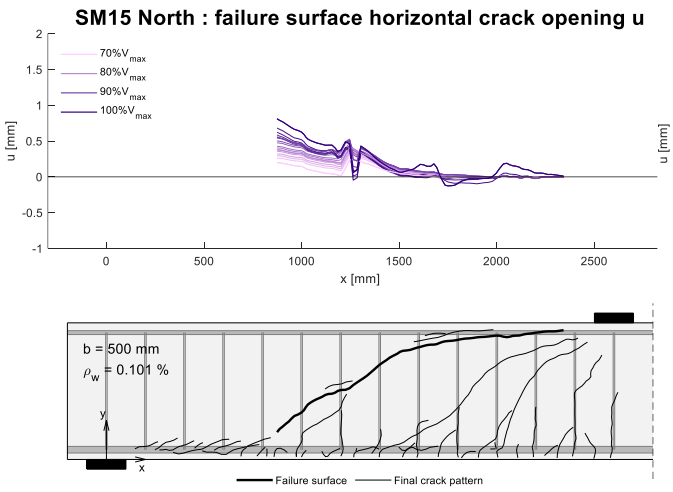

Stirrups ductility class C

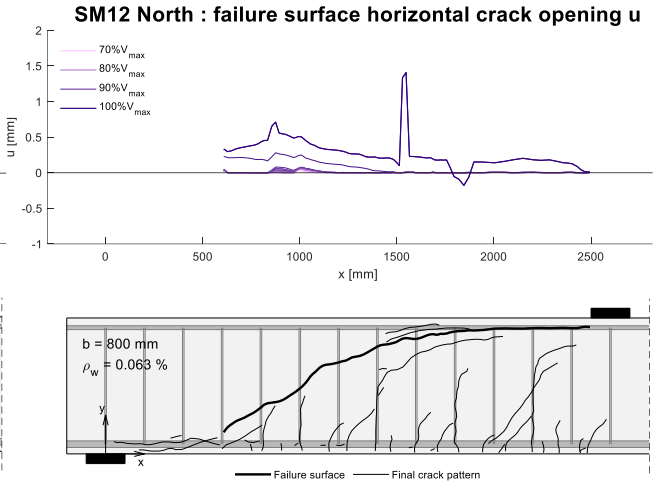

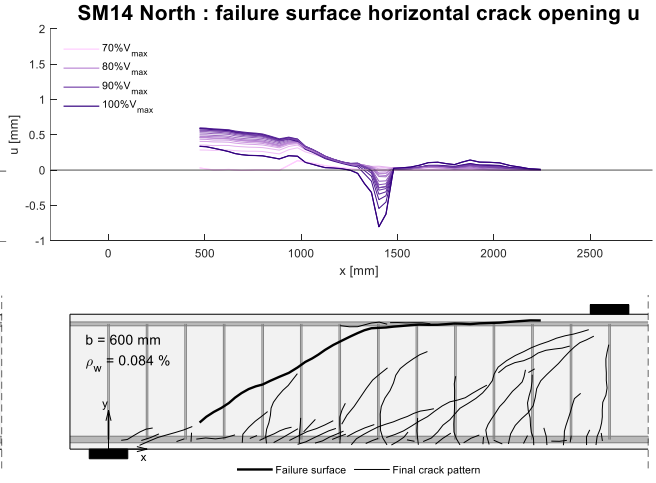

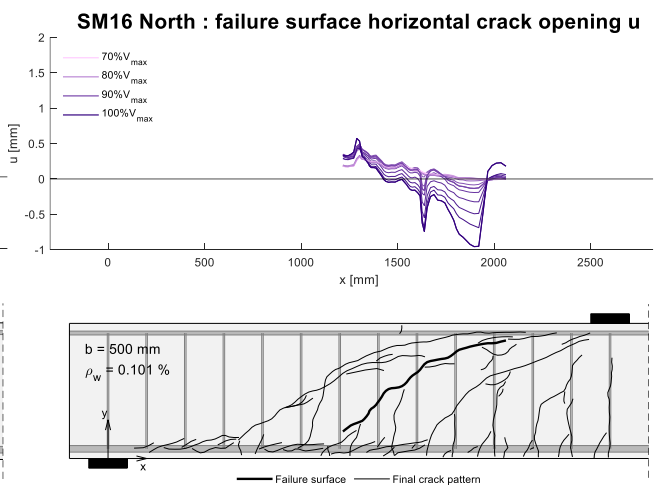

11.1.2 Vertical crack opening v

The actual kinematics have been represented for each specimen from 70% to 100% of the ultimate load with a load level spacing of 2%.

Stirrups ductility class A

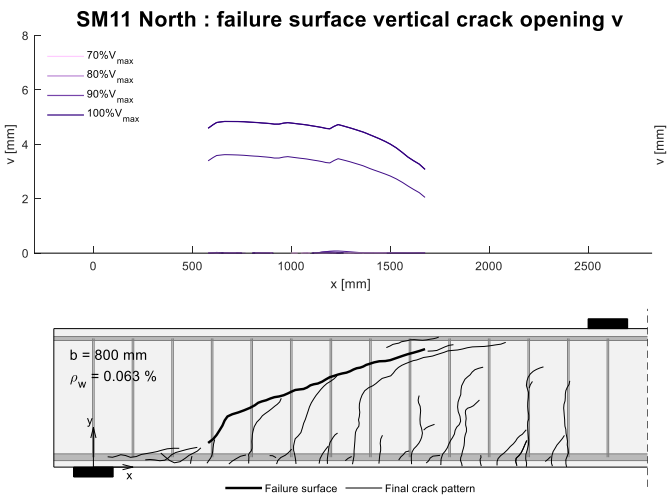

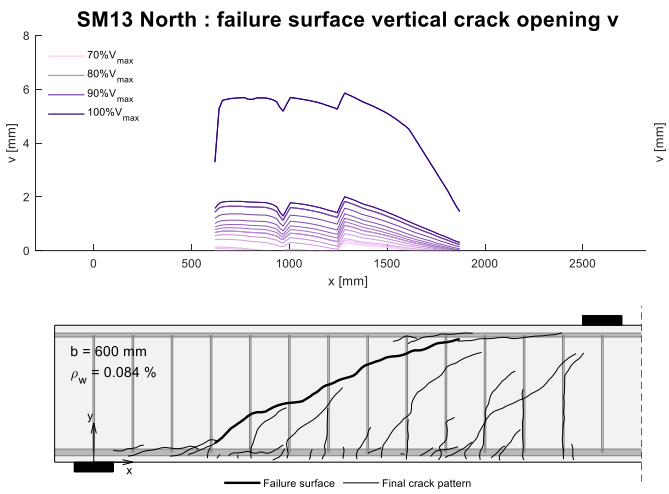

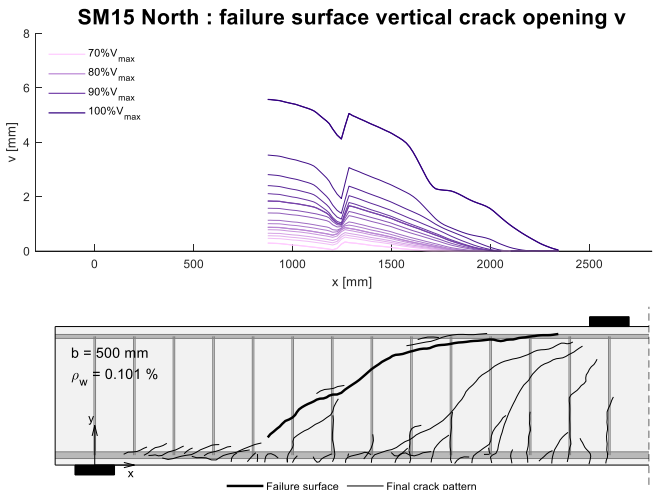

Stirrups ductility class C

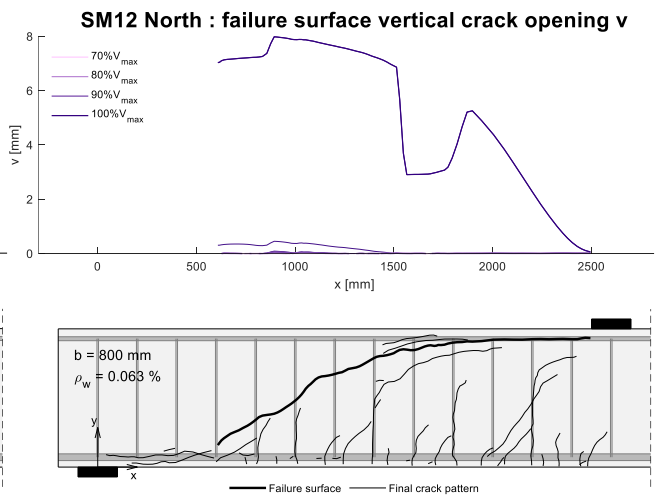

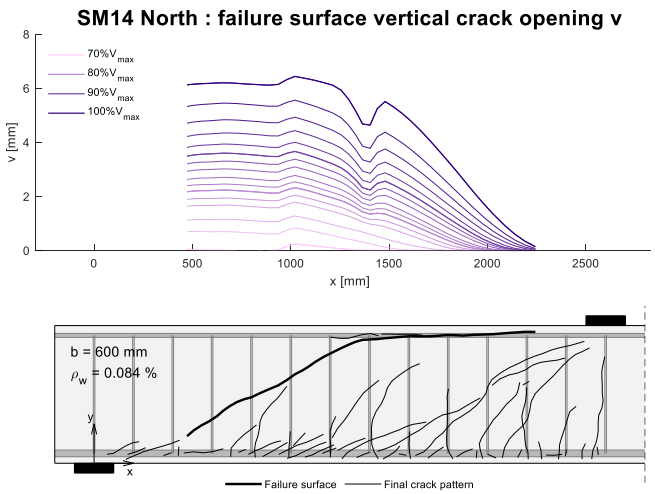

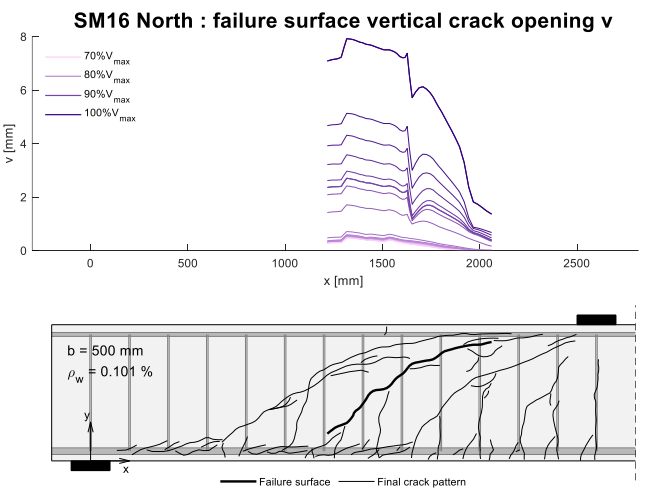

11.1.3 Crack opening w

The actual kinematics have been represented for each specimen from 70% to 100% of the ultimate load with a load level spacing of 2%.

Stirrups ductility class A

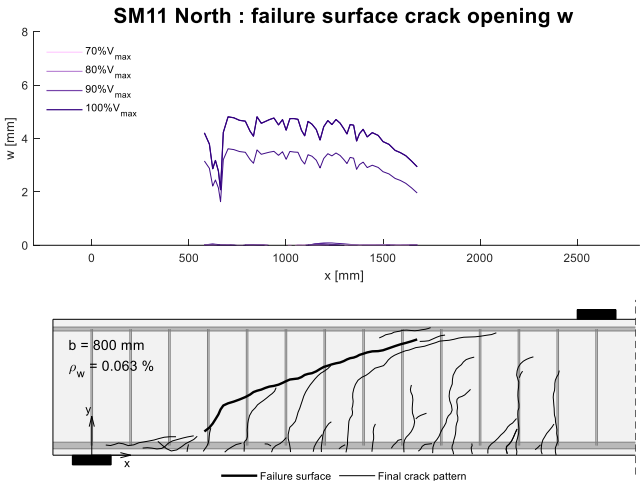

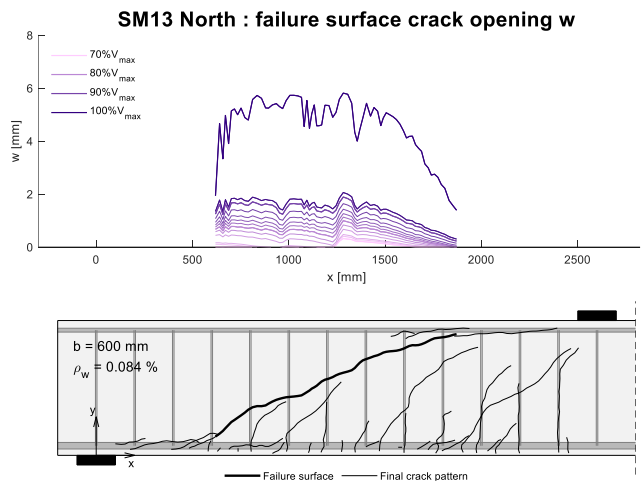

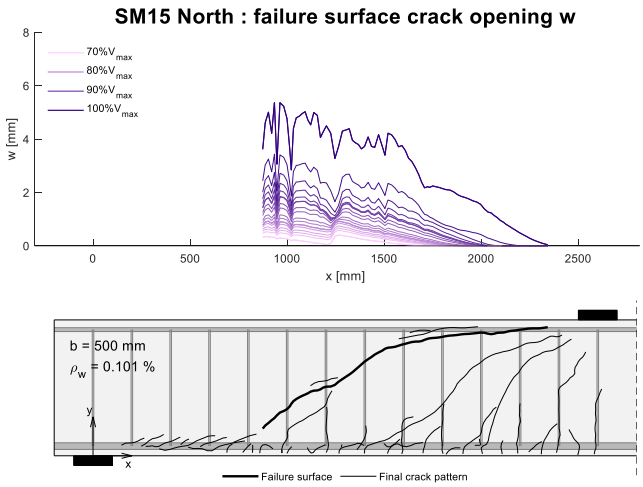

Stirrups ductility class C

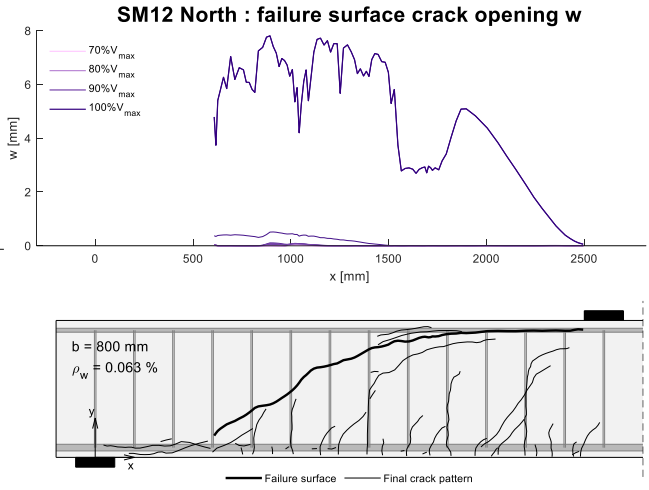

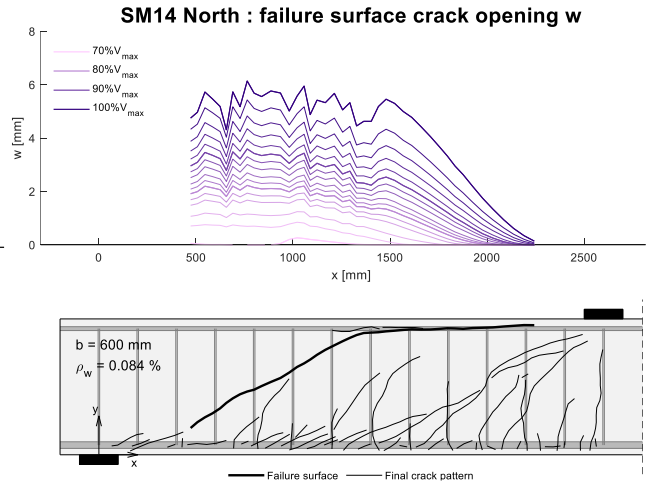

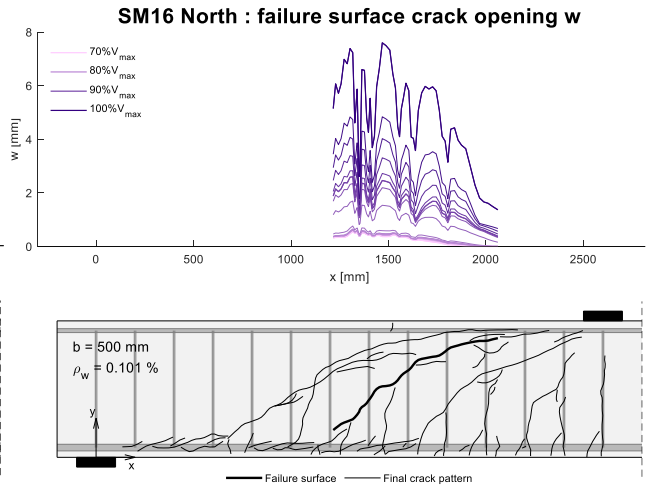

11.1.4 Crack slip s

The actual kinematics have been represented for each specimen from 70% to 100% of the ultimate load with a load level spacing of 2%.

Stirrups ductility class A

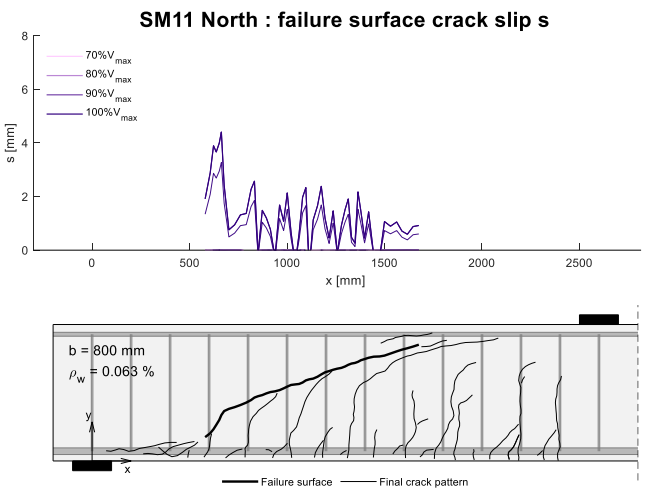

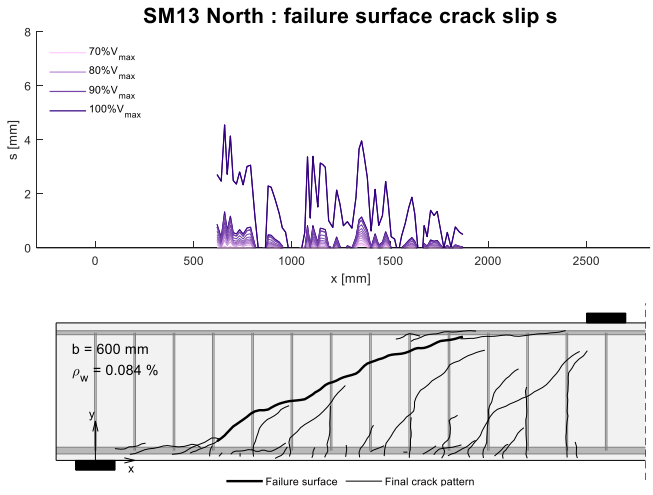

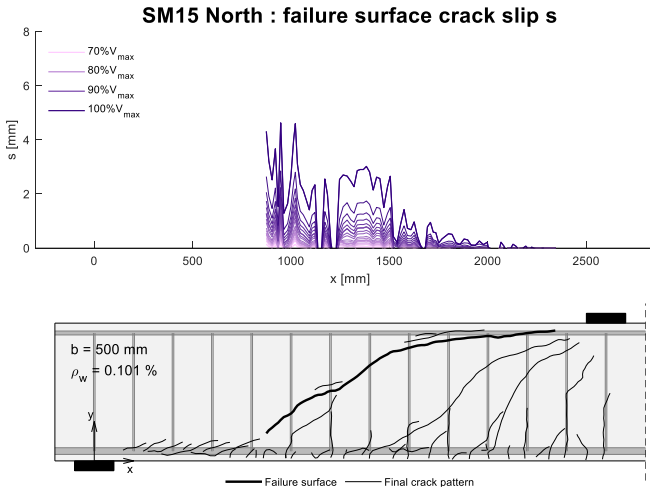

Stirrups ductility class C

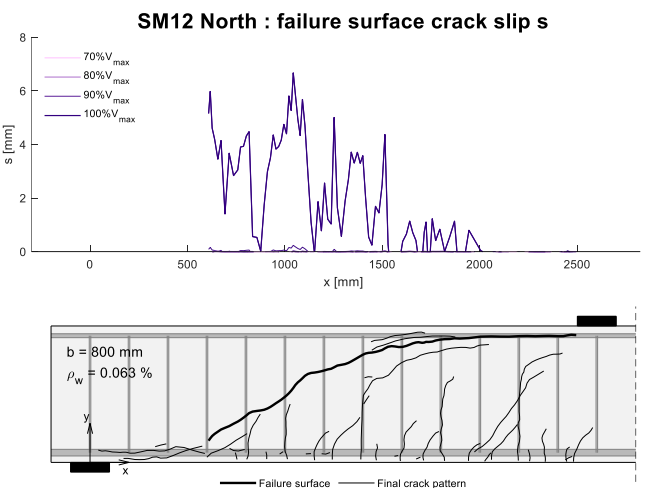

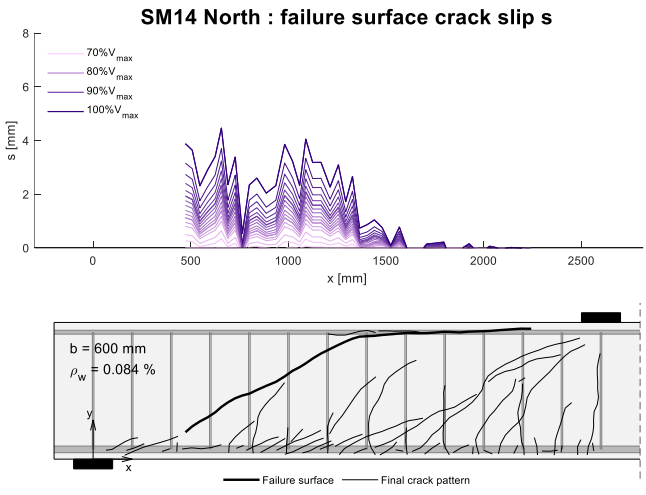

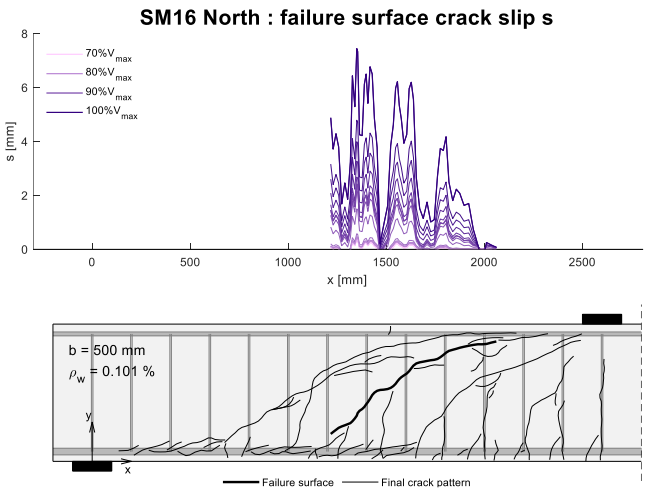

11.2 FOM calculated shear force in the tensed flexural reinforcement

Stirrups ductility class A

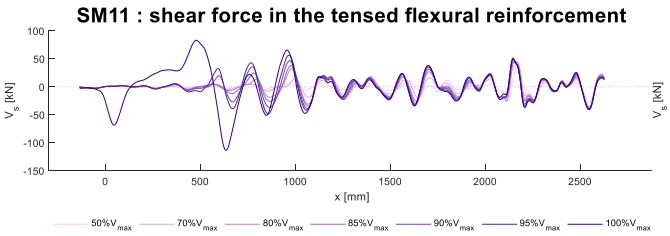

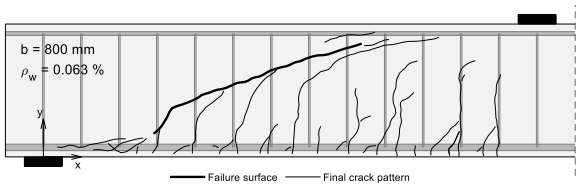

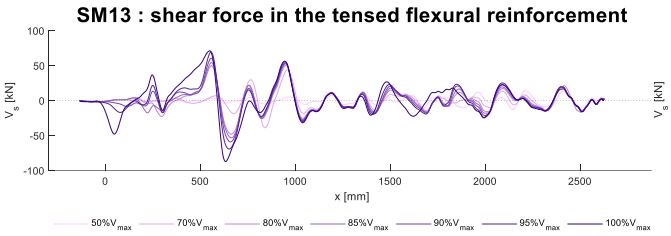

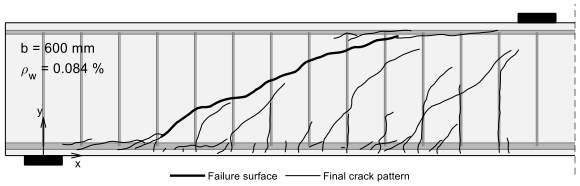

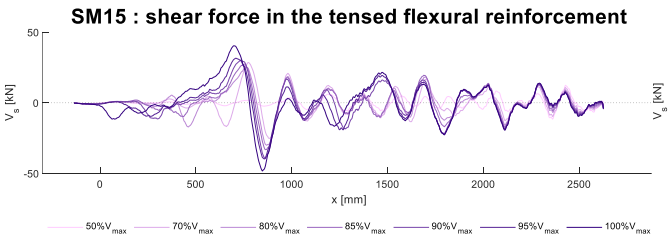

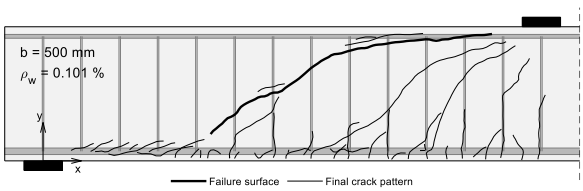

Stirrups ductility class C

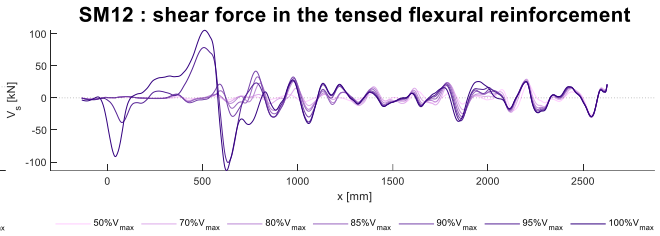

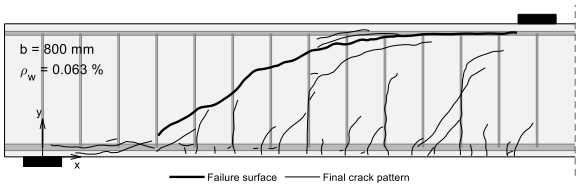

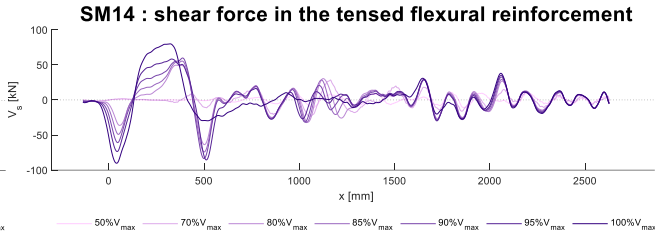

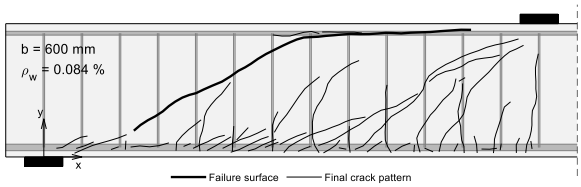

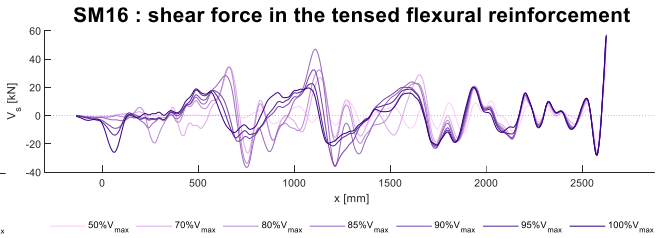

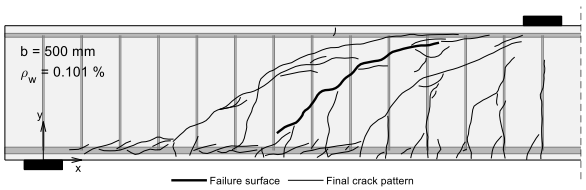

11.3 FOM stirrups strain

With median filtering applied.

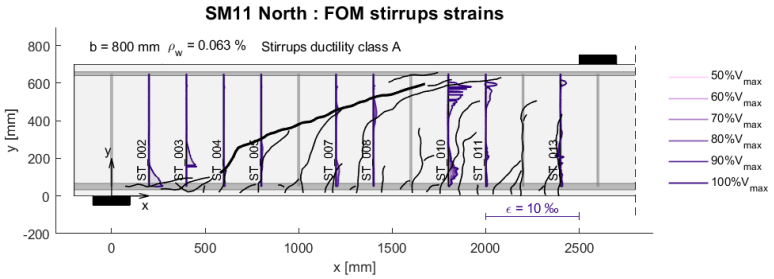

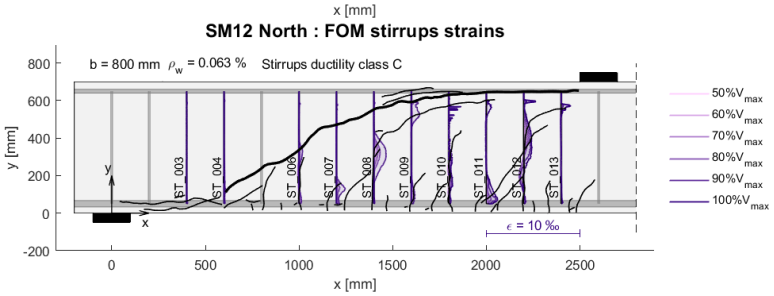

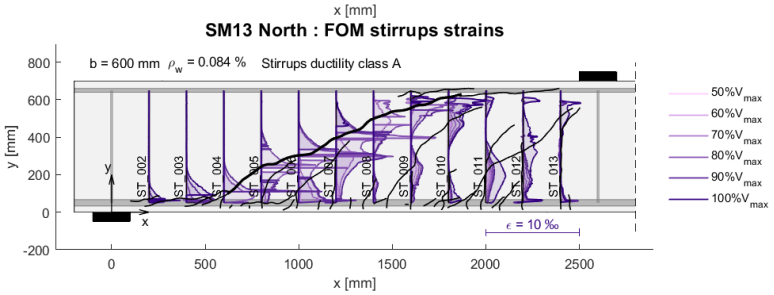

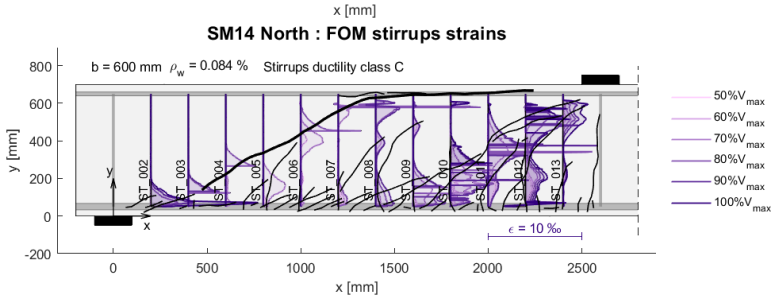

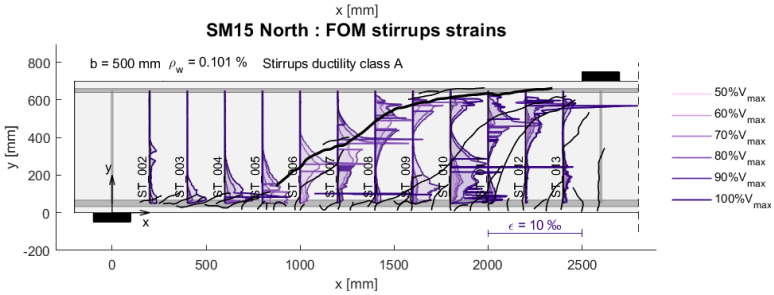

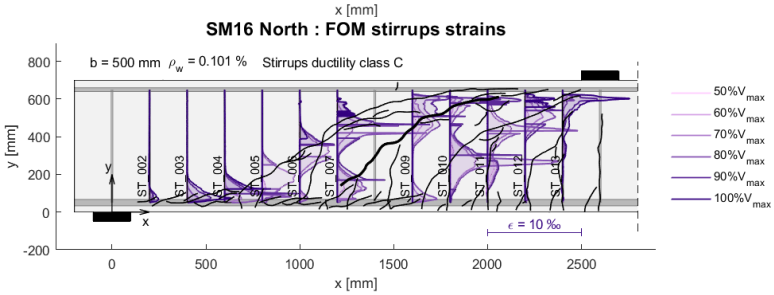

11.4 Crack rotation and rotation increment during propagation

Crack rotation at each horizontal propagation increment dH is represented hereafter with a smooth parameter of 0.1 to enhance the readability of the results.

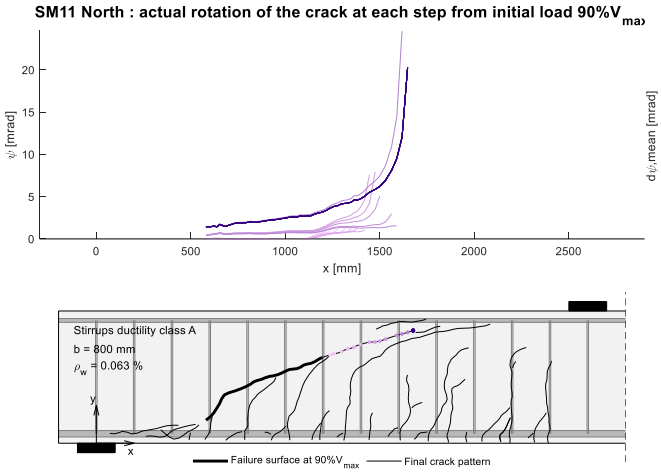

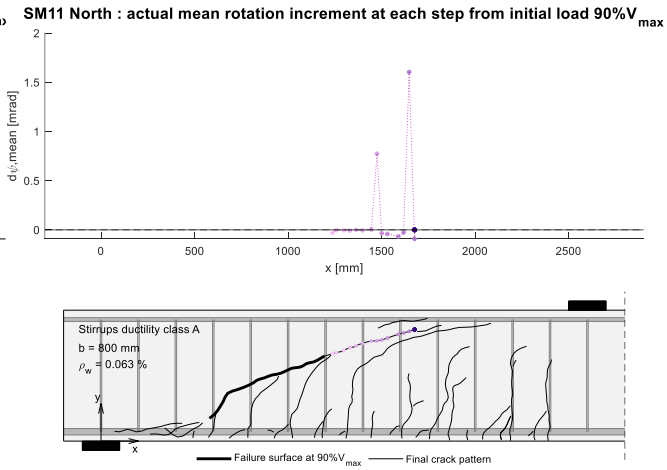

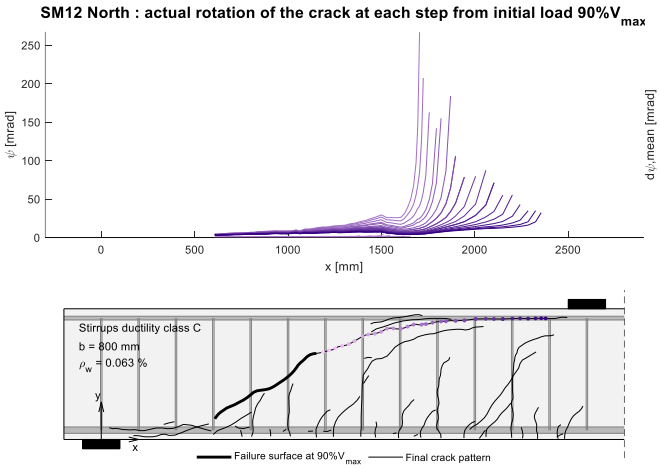

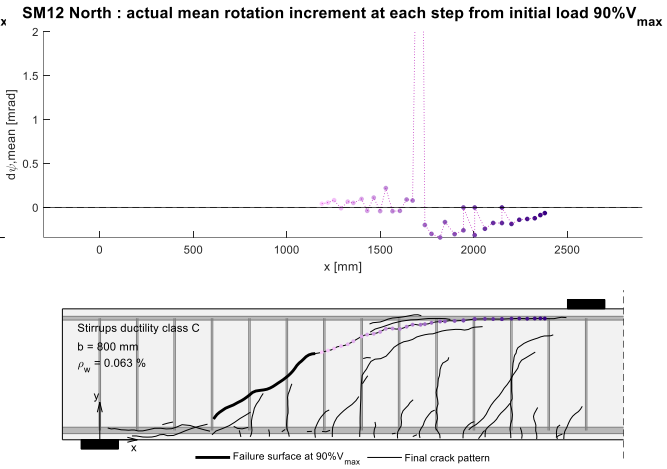

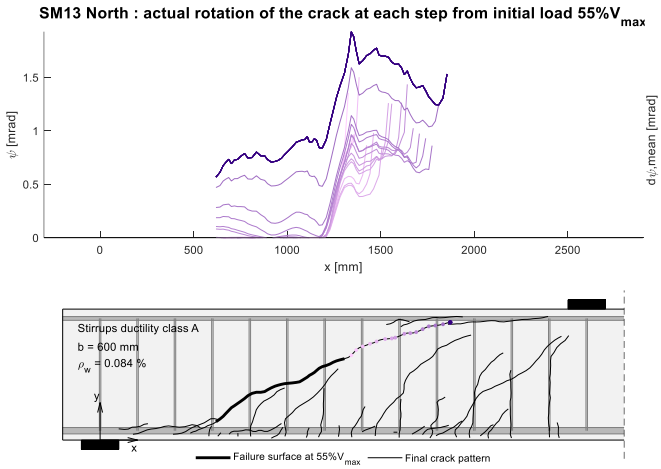

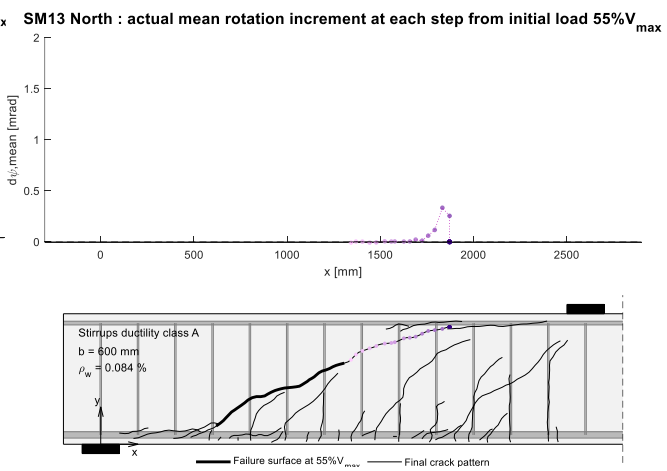

SM14 North : actual rotation of the crack at each step from initial load 55%V_{max}

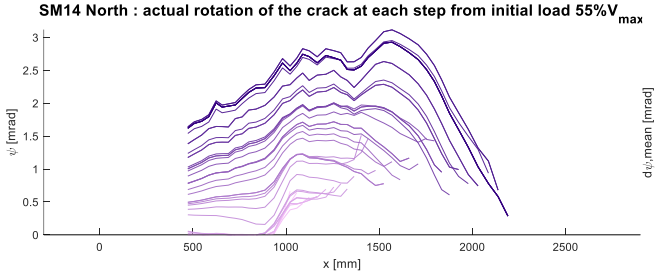

SM14 North : actual mean rotation increment at each step from initial load 55%V_{max}

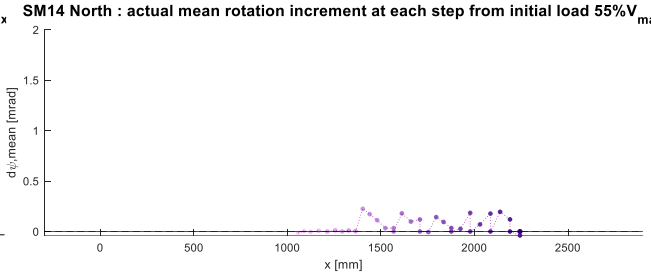

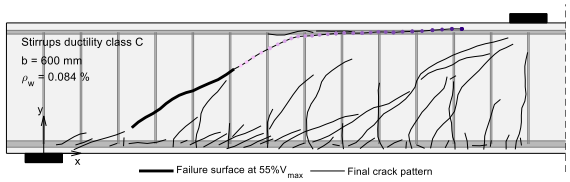

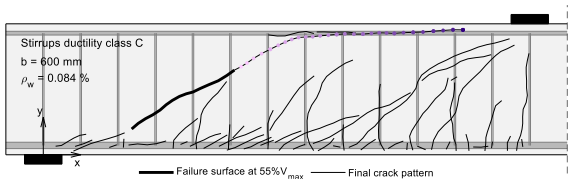

SM15 North : actual rotation of the crack at each step from initial load 45%V_{max}

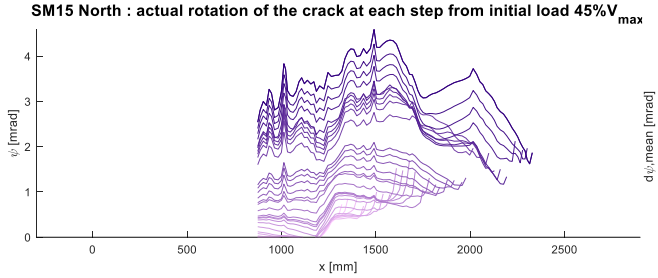

SM15 North : actual mean rotation increment at each step from initial load 45%V_{max}

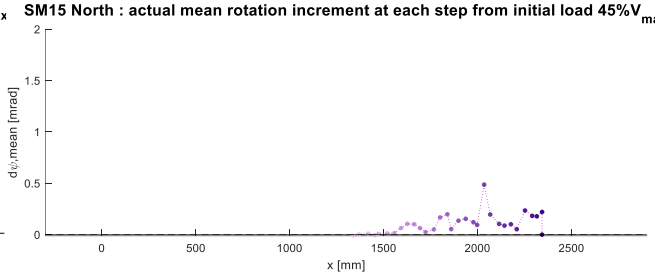

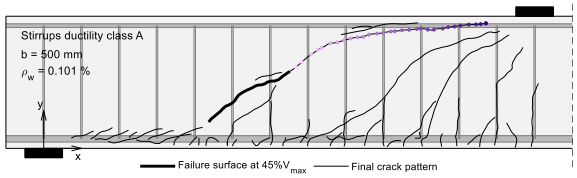

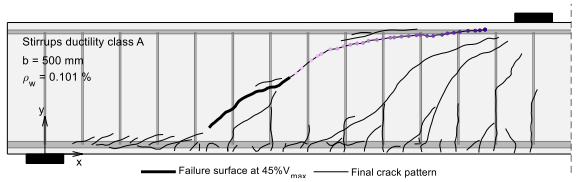

SM16 North : actual rotation of the crack at each step from initial load 45%V_{max}

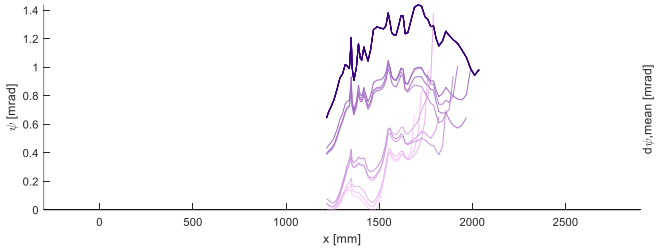

SM16 North : actual mean rotation increment at each step from initial load 45%V_{max}

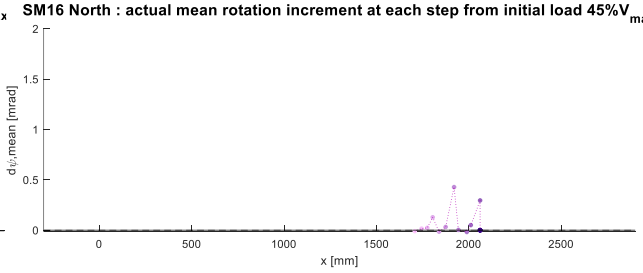

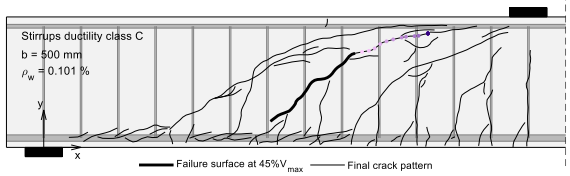

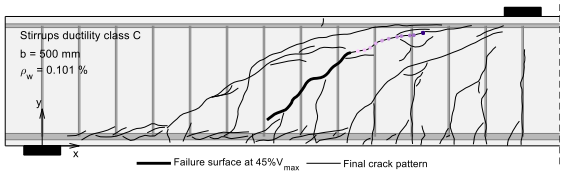

11.5 Multiple crack: sum of the horizontal crack openings

SM11 North : actual horizontal crack opening u at 96 % V_{max}

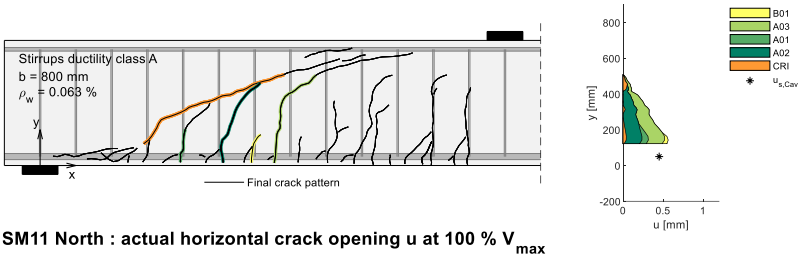

SM11 North : actual horizontal crack opening u at 100 % V_{max}

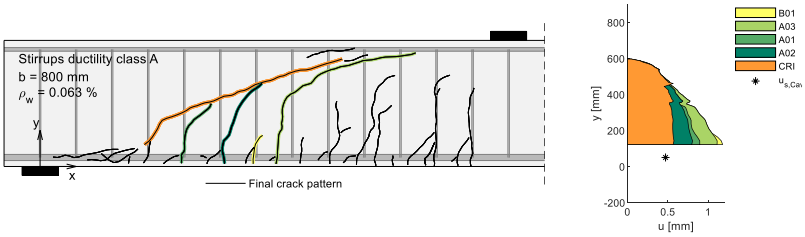

SM12 North : actual horizontal crack opening u at 80 % V_{max}

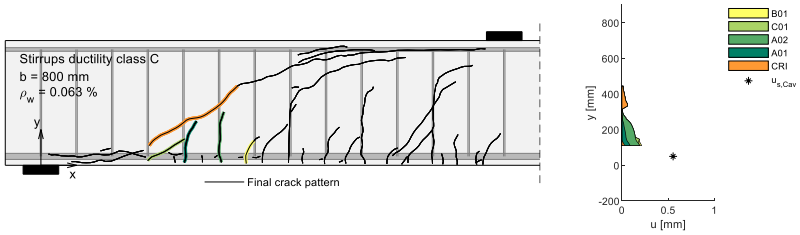

SM12 North : actual horizontal crack opening u at 100 % V_{max}

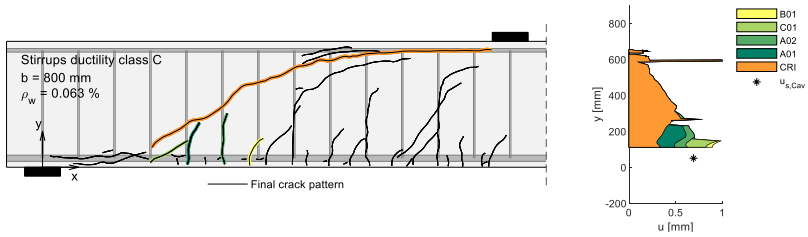

SM13 North : actual horizontal crack opening u at 80 % V_{max}

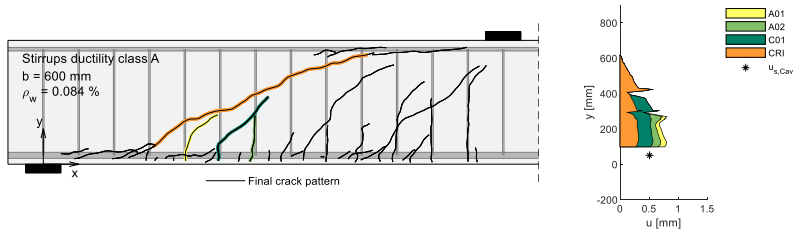

SM13 North : actual horizontal crack opening u at 100 % V_{max}

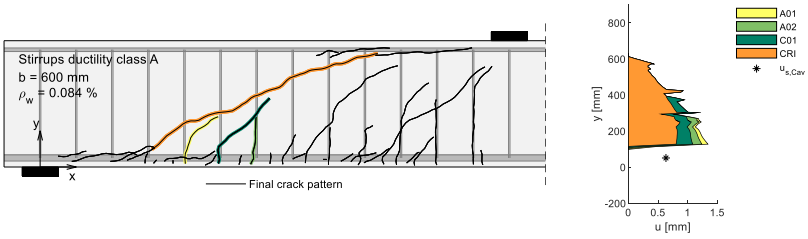

SM14 North : actual horizontal crack opening u at 80 % V_{max}

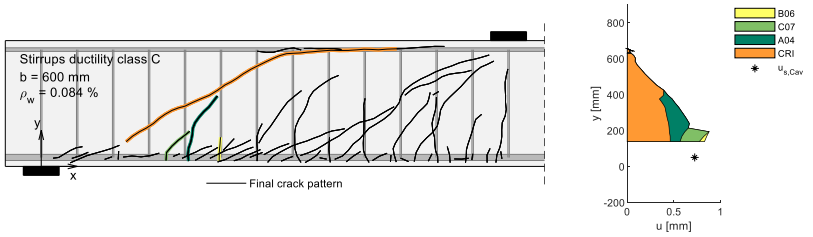

SM14 North : actual horizontal crack opening u at 100 % V_{max}

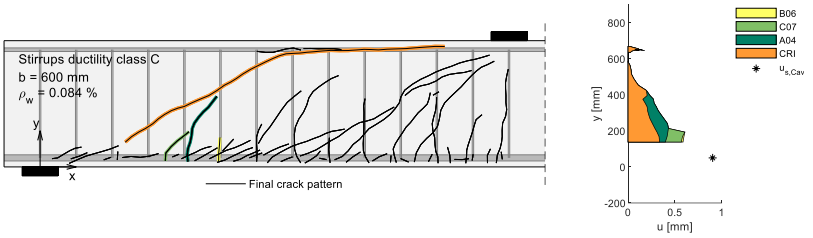

SM15 North : actual horizontal crack opening u at 80 % V_{max}

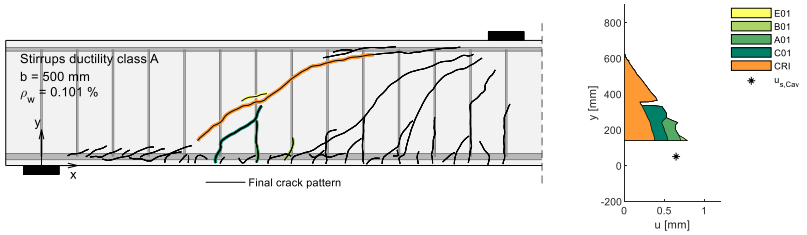

SM15 North : actual horizontal crack opening u at 100 % V_{max}

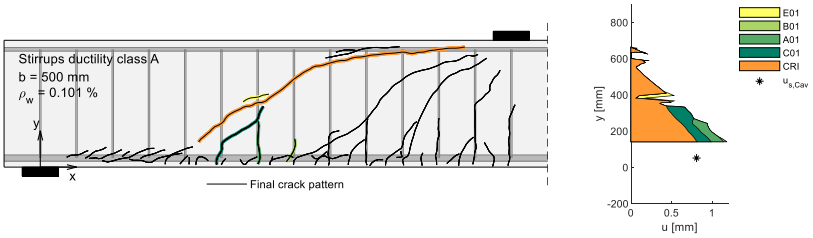

SM16 North : actual horizontal crack opening u at 80 % V_{max}

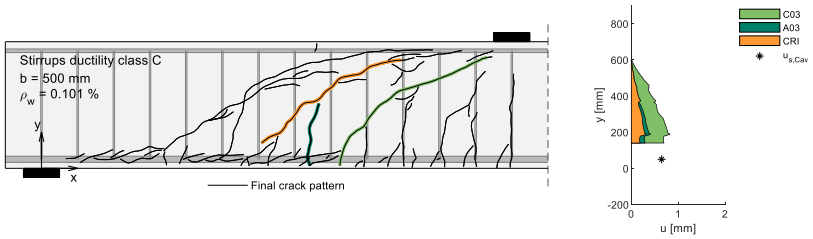

SM16 North : actual horizontal crack opening u at 100 % V_{max}

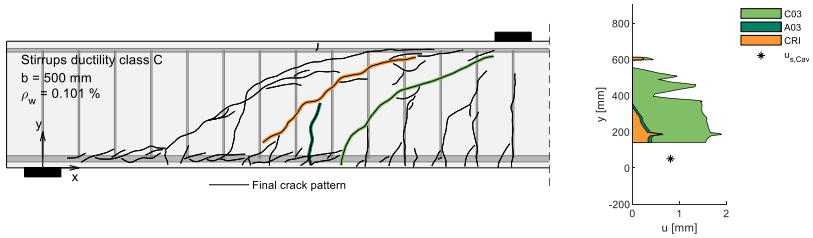

11.6 Kinematics predictions based on a load-propagation relationship

11.6.1 Horizontal crack opening u

SM11 North : failure crack actual and predicted horizontal crack opening at each step

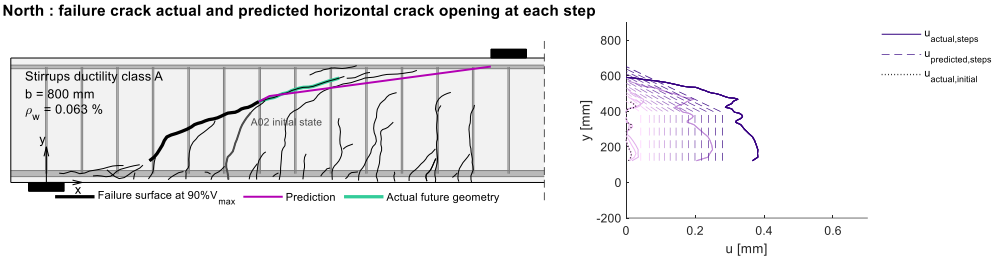

SM12 North : failure crack actual and predicted horizontal crack opening at each step

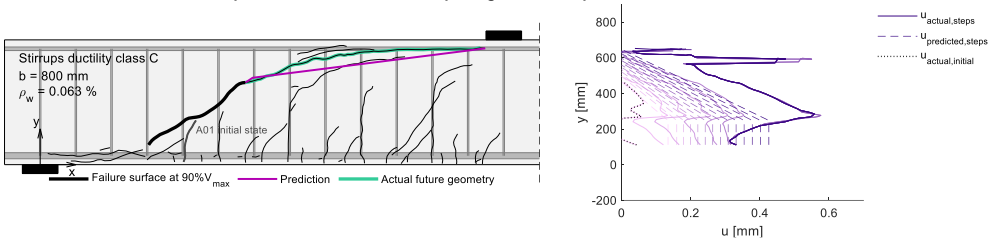

SM13 North : failure crack actual and predicted horizontal crack opening at each step

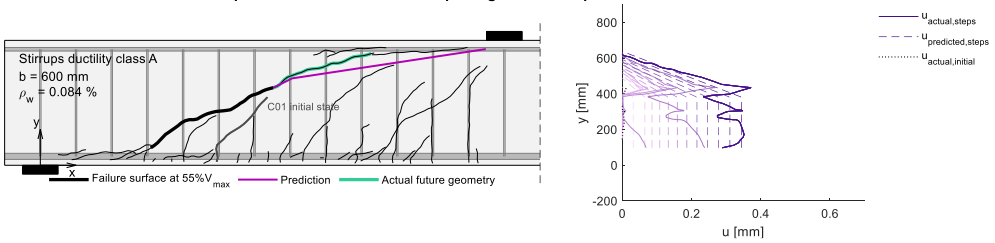

SM14 North : failure crack actual and predicted horizontal crack opening at each step

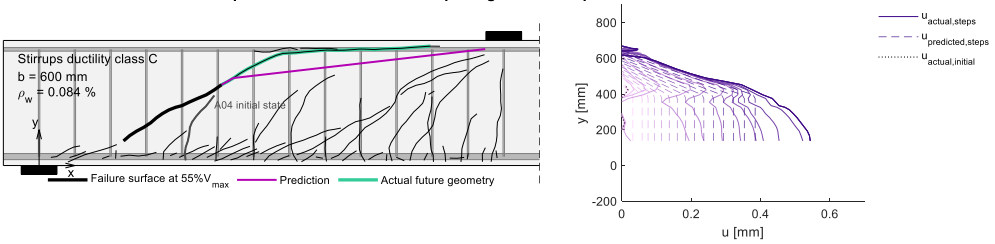

SM15 North : failure crack actual and predicted horizontal crack opening at each step

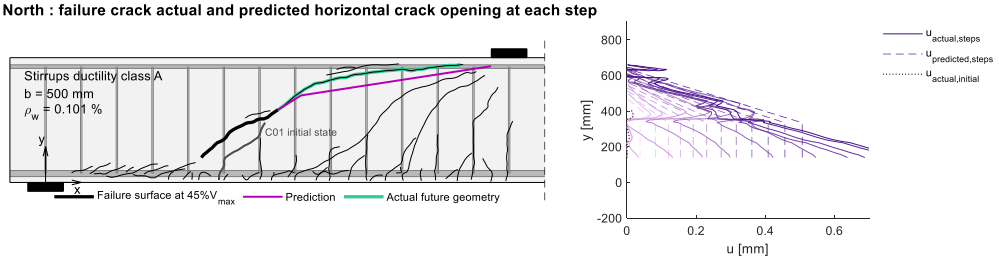

SM16 North : failure crack actual and predicted horizontal crack opening at each step

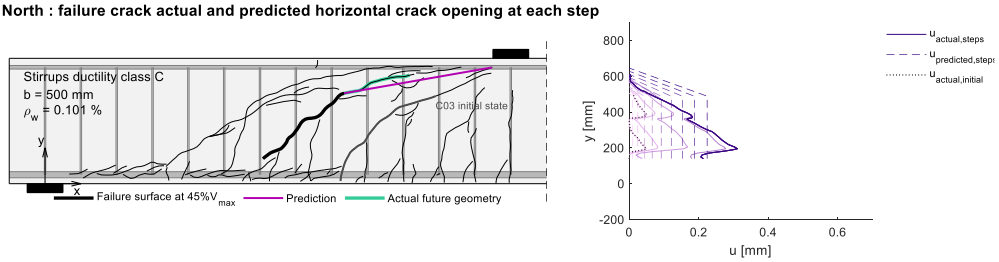

11.6.2 Vertical crack opening v

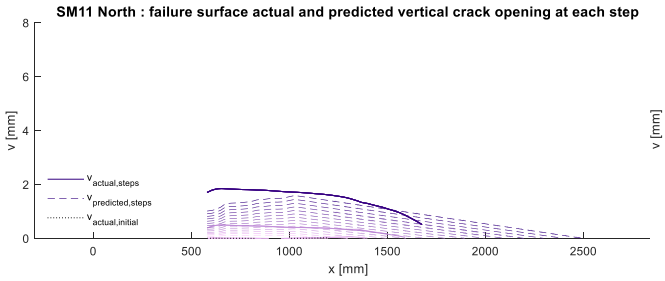

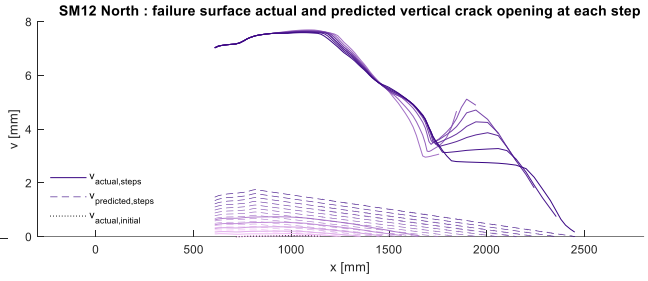

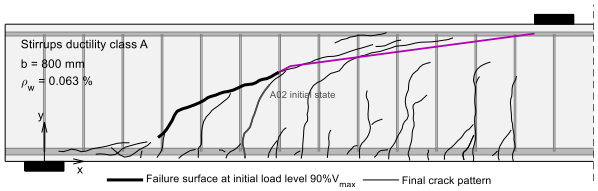

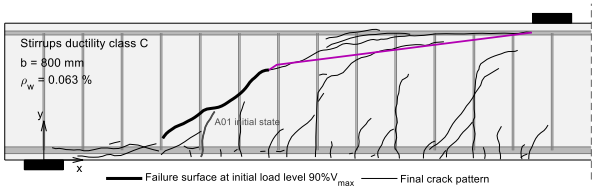

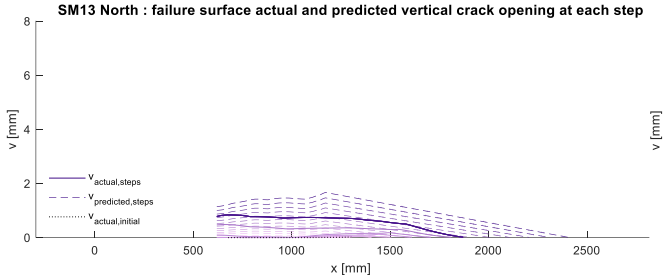

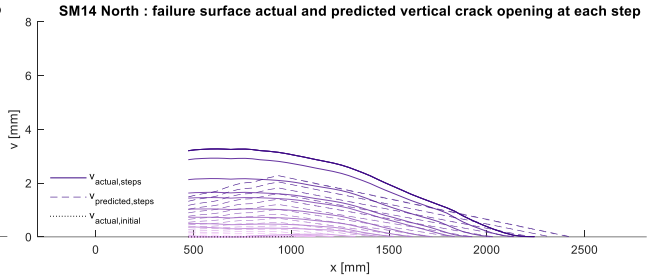

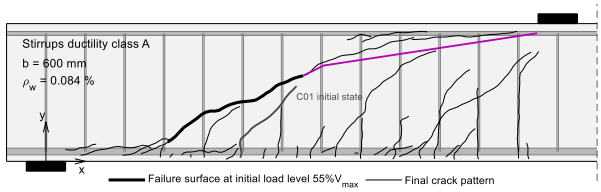

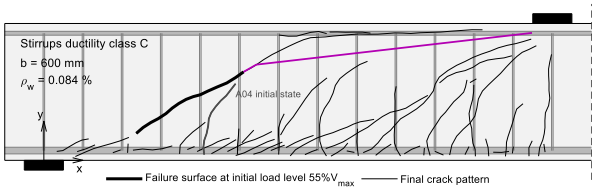

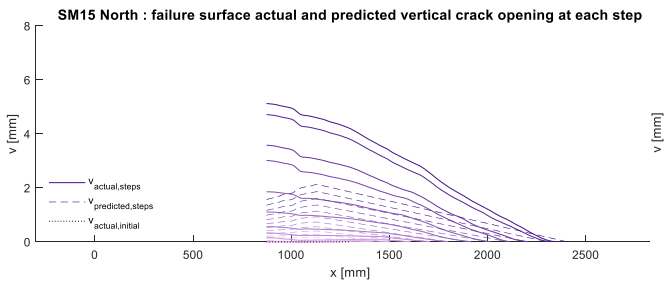

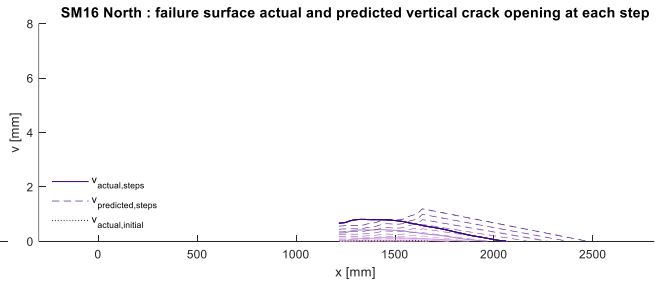

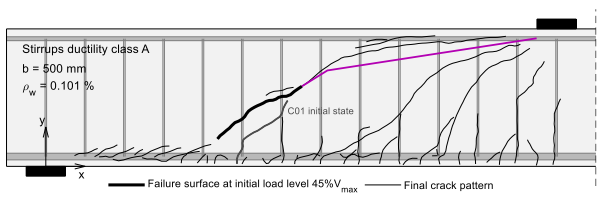

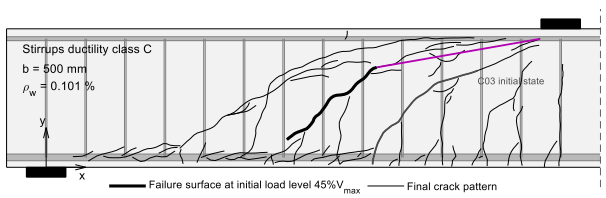

11.7 Predicted ultimate load based on a load-propagation relationship

SM11 North : failure crack propagation prediction

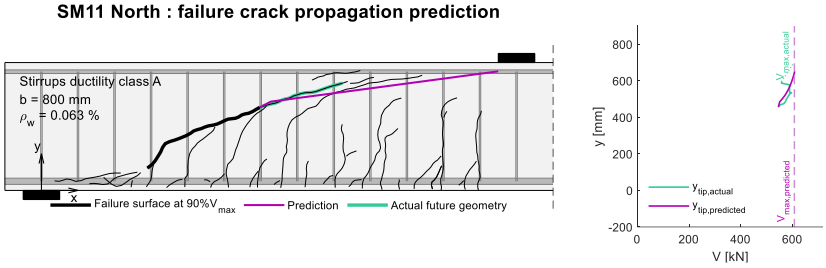

SM12 North : failure crack propagation prediction

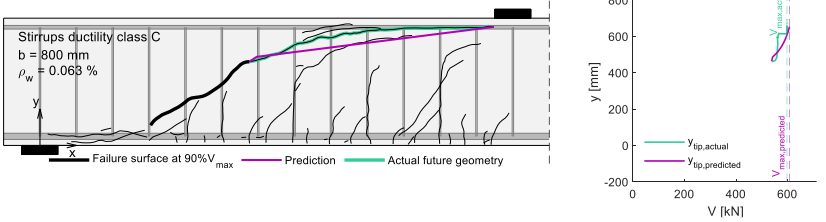

SM13 North : failure crack propagation prediction

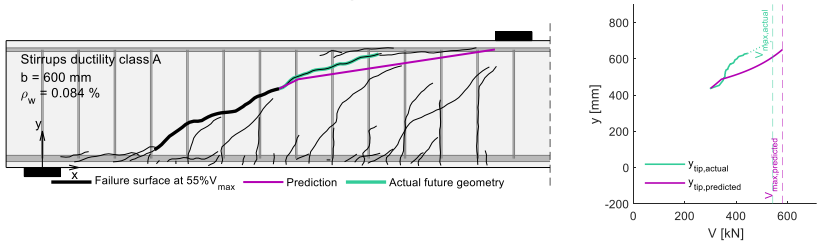

SM14 North : failure crack propagation prediction

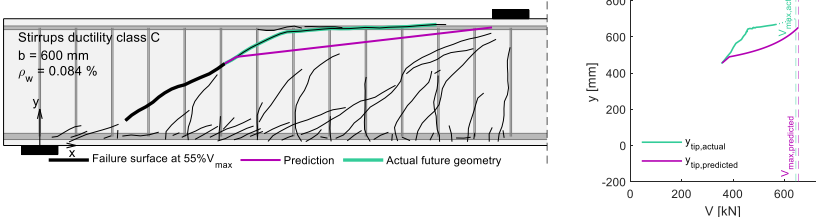

SM15 North : failure crack propagation prediction

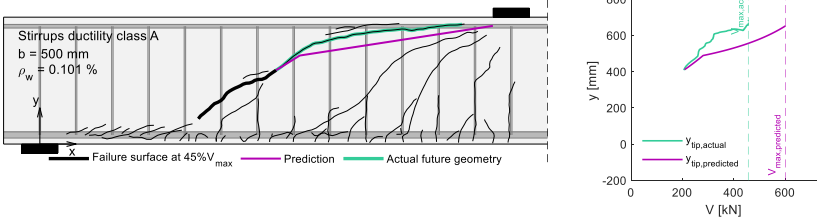

SM16 North : failure crack propagation prediction

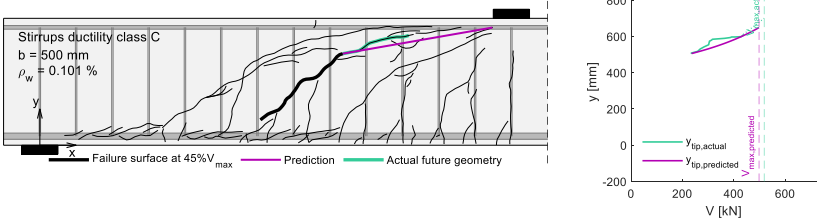

11.8 DIC concrete strain field without statistical outliers

SM11 North : concrete strain field at ultimate load

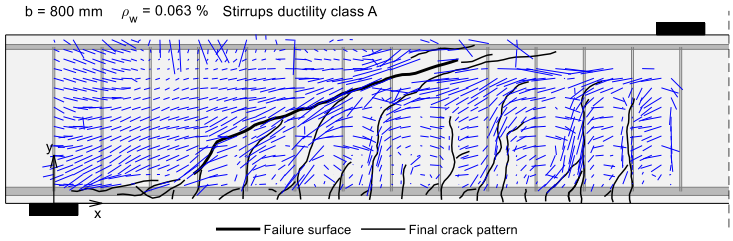

SM12 North : concrete strain field at ultimate load

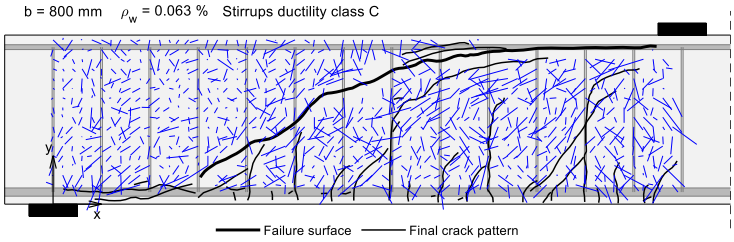

SM13 North : concrete strain field at ultimate load

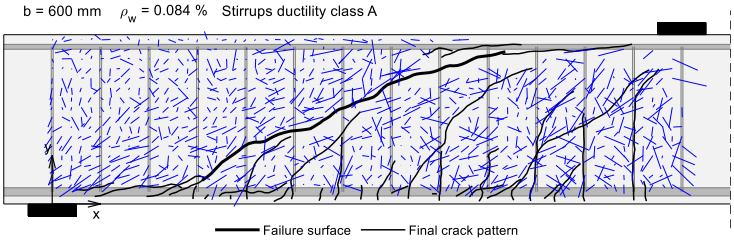

SM14 North : concrete strain field at ultimate load

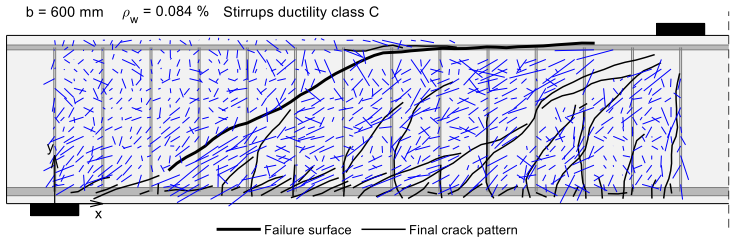

SM15 North : concrete strain field at ultimate load

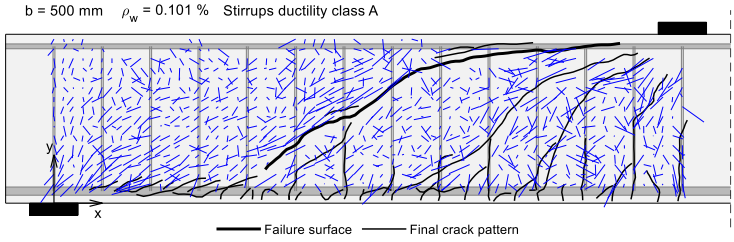

SM16 North : concrete strain field at ultimate load

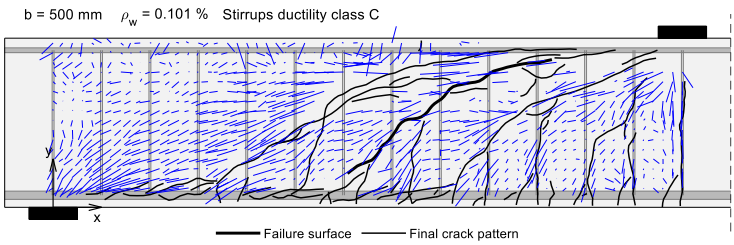

11.9 STA along the failure surface

11.9.1 Aggregate interlock stresses

11.9.1.1 Tangential stress

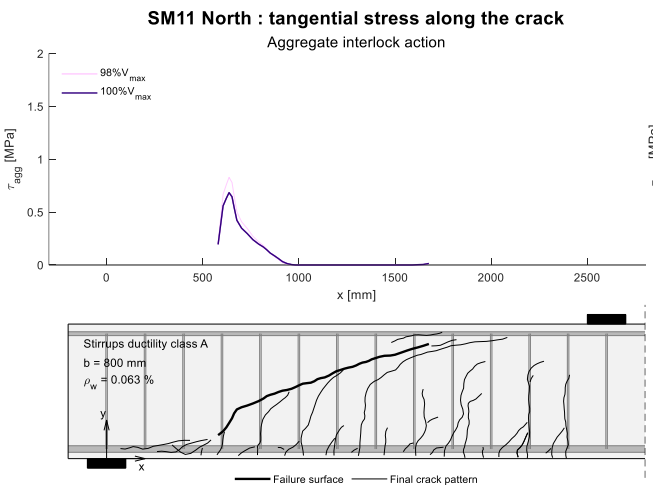

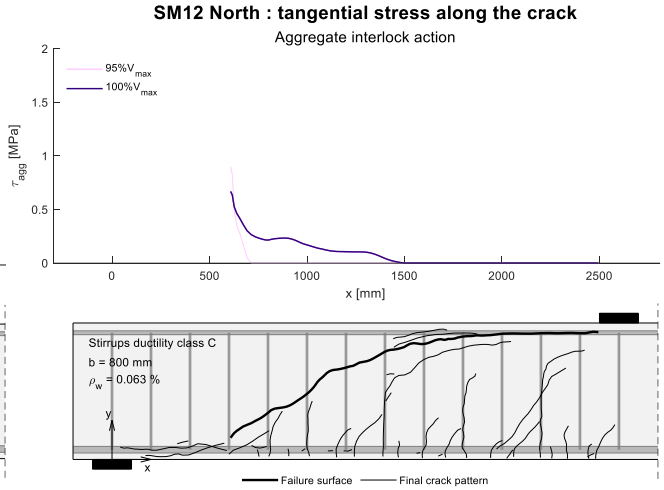

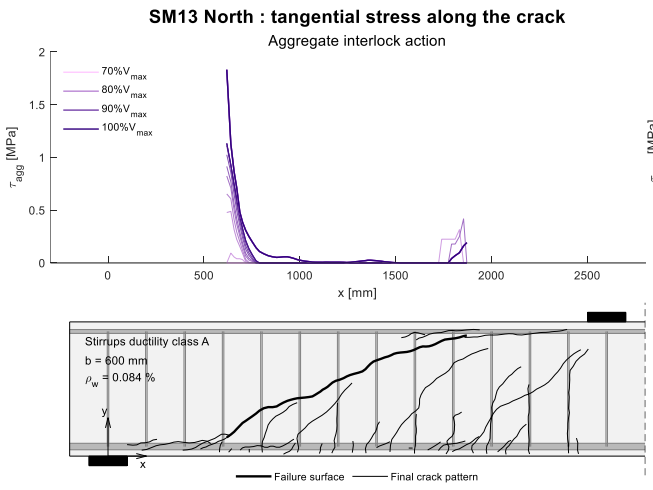

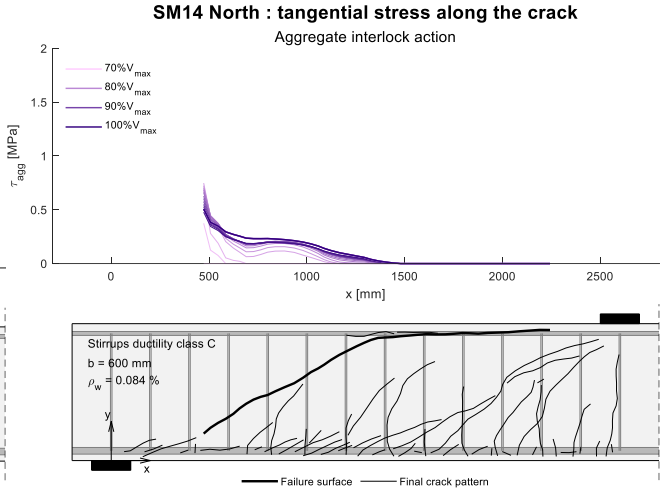

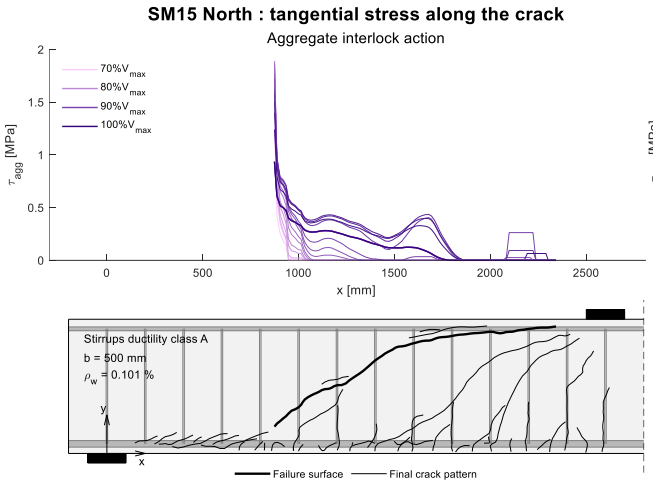

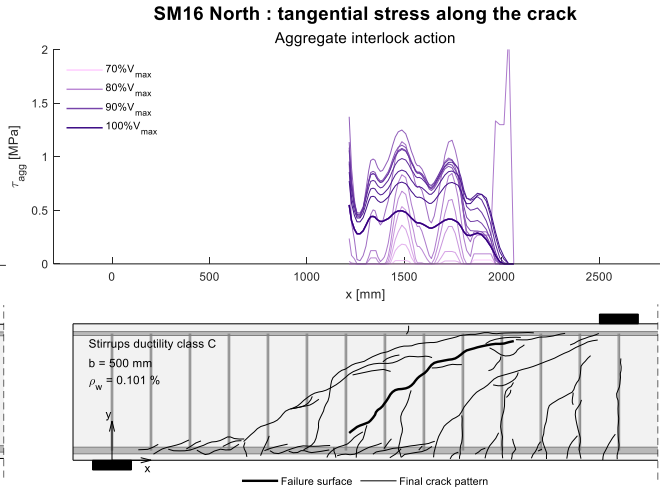

11.9.1.2 Normal stress

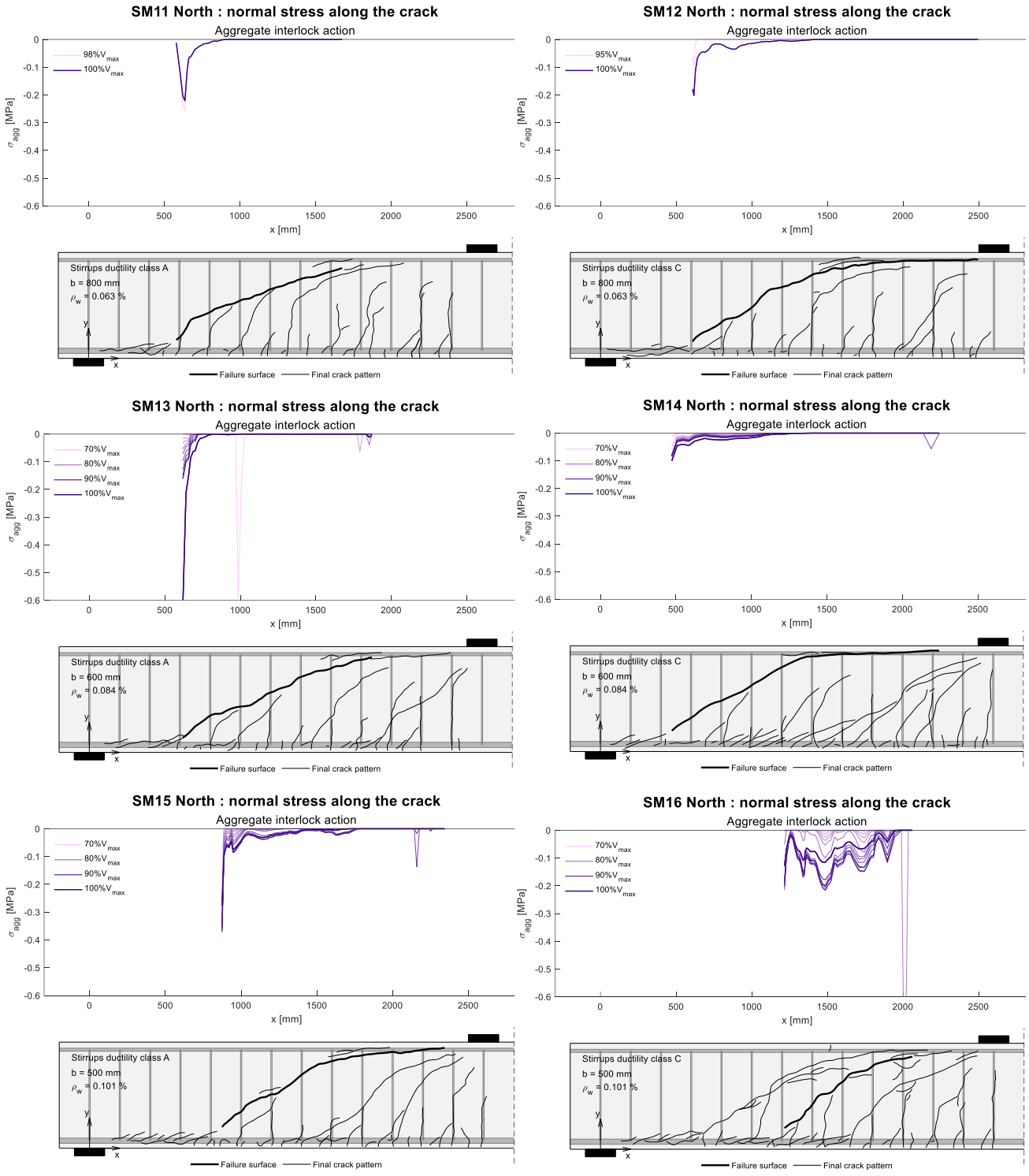

11.9.2 Concrete residual tensile strength stresses

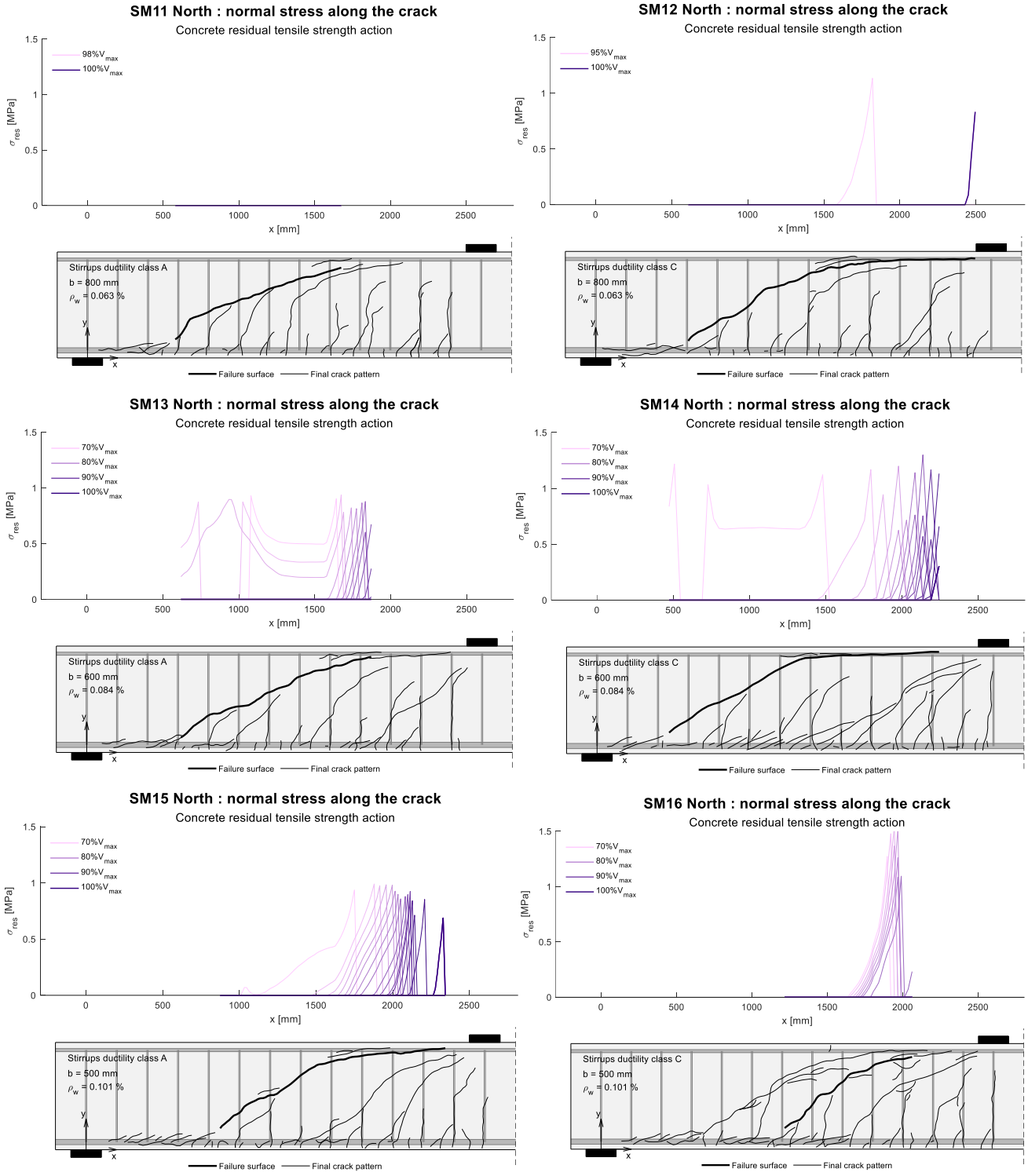

11.10 NLFEA results for elastic-plastic stress-strain steel law

11.10.1 Jconc stress field and softening factor

Original mesh

SM12 North : cracking pattern and Jconc stresses at ultimate load

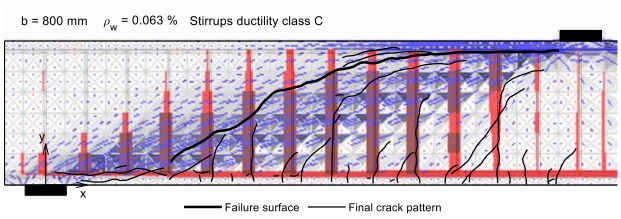

SM12 North : cracking pattern and Jconc η_2 at ultimate load

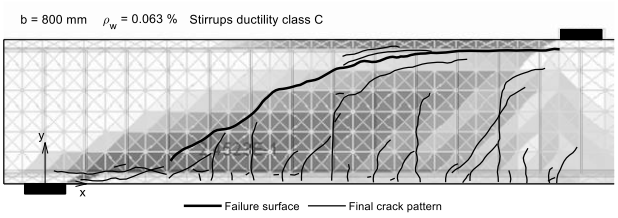

SM14 North : cracking pattern and Jconc stresses at ultimate load

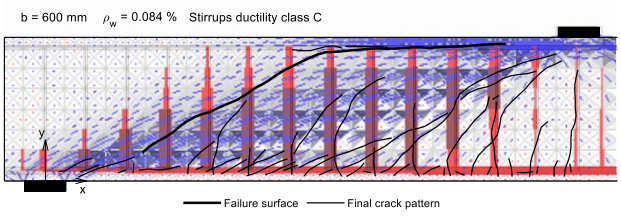

SM14 North : cracking pattern and Jconc η_2 at ultimate load

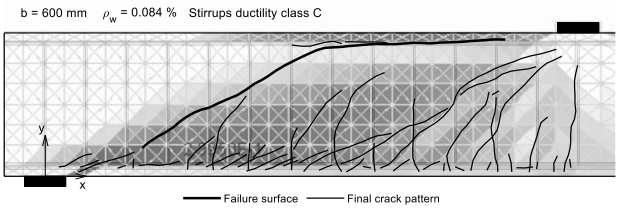

SM16 North : cracking pattern and Jconc stresses at ultimate load

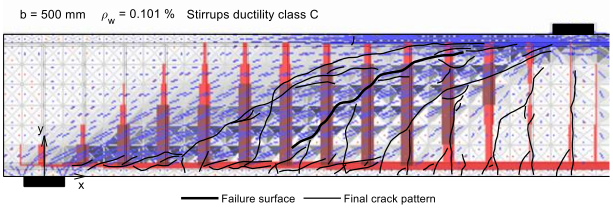

SM16 North : cracking pattern and Jconc η_2 at ultimate load

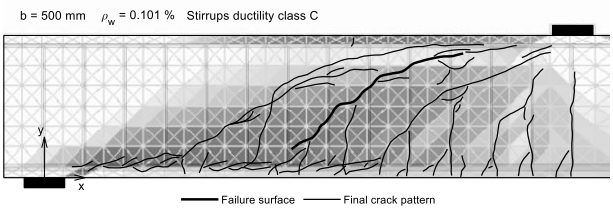

Denser mesh

SM12 North : cracking pattern and Jconc stresses at ultimate load

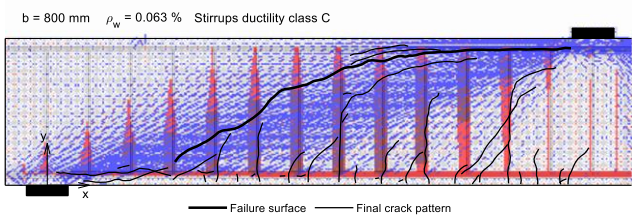

SM12 North : cracking pattern and Jconc η_2 at ultimate load

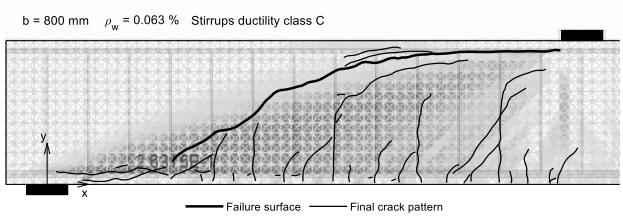

SM14 North : cracking pattern and Jconc stresses at ultimate load

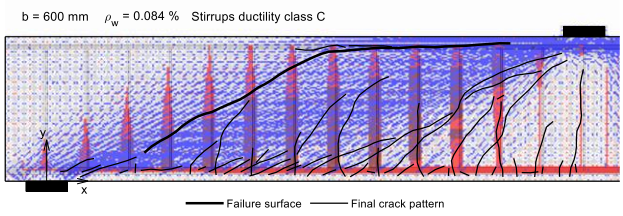

SM14 North : cracking pattern and Jconc η_2 at ultimate load

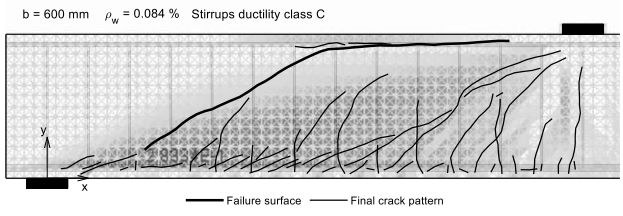

SM16 North : cracking pattern and Jconc stresses at ultimate load

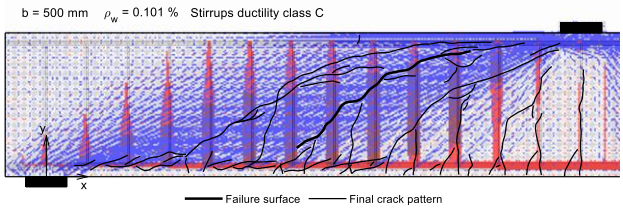

SM16 North : cracking pattern and Jconc η_2 at ultimate load

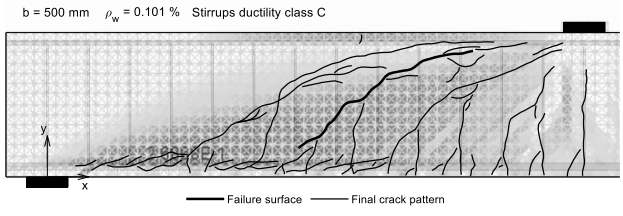

11.10.2 Jconc versus FOM stirrups strain comparison

SM12 North : Jconc and FOM stirrups strains at 70% V_{max} = 418 kN

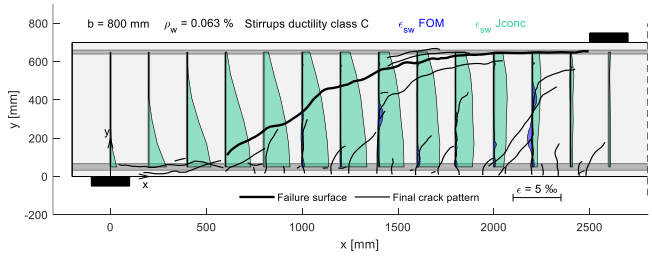

SM12 North : Jconc and FOM stirrups strains at 80% V_{max} = 478 kN

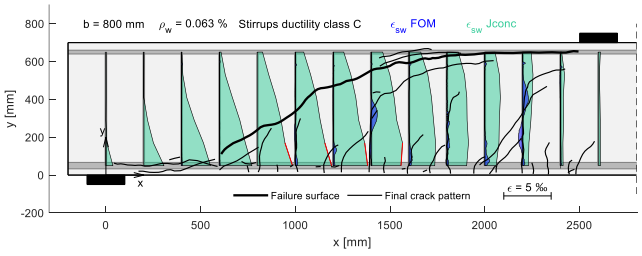

SM12 North : Jconc and FOM stirrups strains at 90% V_{max} = 538 kN

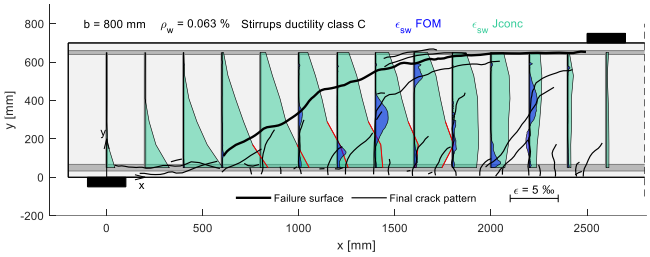

SM12 North : Jconc and FOM stirrups strains at 100% V_{max} = 597 kN

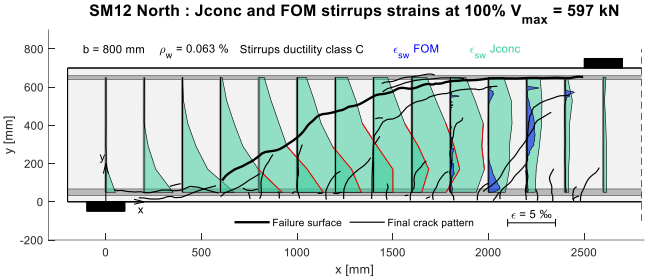

SM14 North : Jconc and FOM stirrups strains at 70% V_{max} = 451 kN

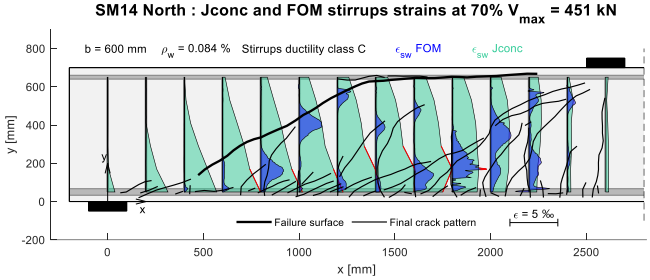

SM14 North : Jconc and FOM stirrups strains at 80% V_{max} = 515 kN

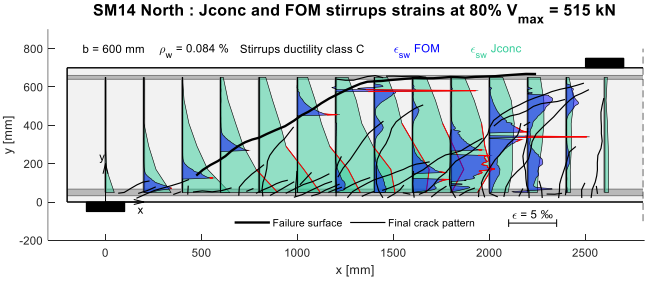

SM14 North : Jconc and FOM stirrups strains at 90% V_{max} = 580 kN

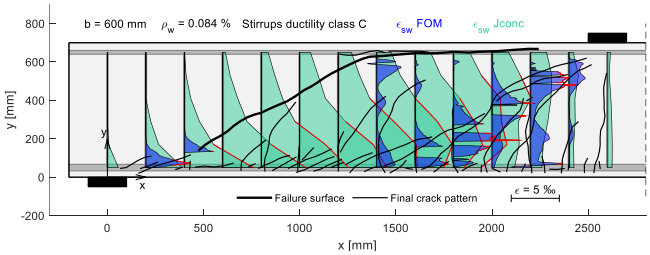

SM14 North : Jconc and FOM stirrups strains at 100% V_{max} = 644 kN

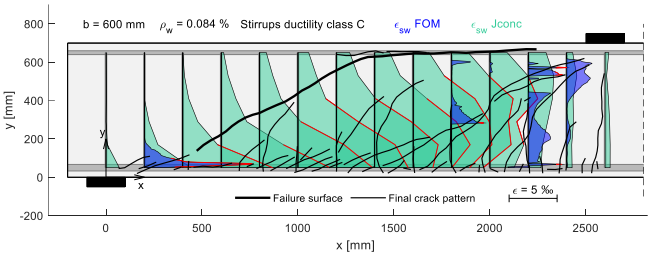

SM16 North : Jconc and FOM stirrups strains at 70% V_{max} = 362 kN

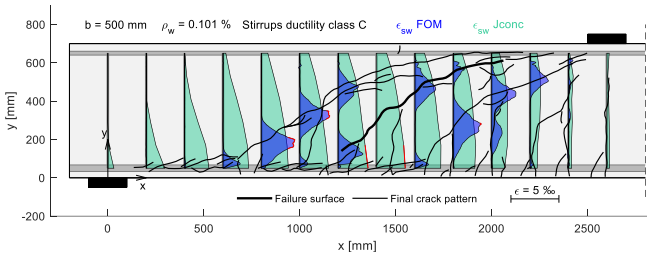

SM16 North : Jconc and FOM stirrups strains at 80% V_{max} = 414 kN

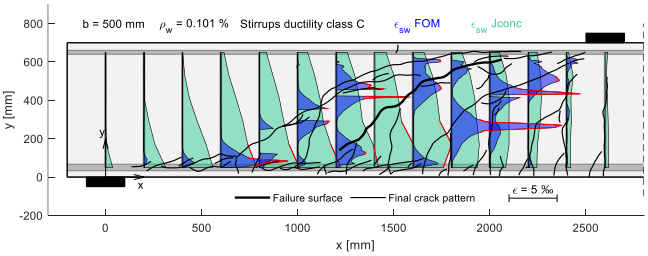

SM16 North : Jconc and FOM stirrups strains at 90% V_{max} = 466 kN

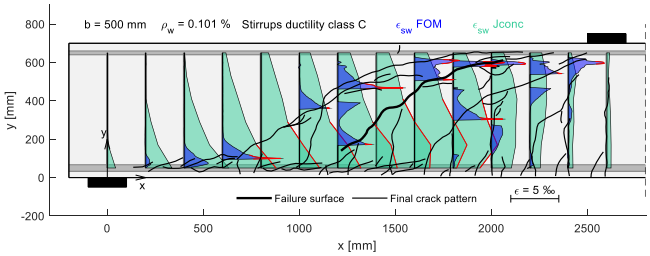

SM16 North : Jconc and FOM stirrups strains at 100% V_{max} = 518 kN

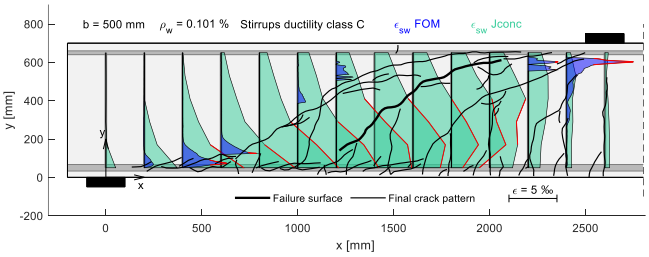

11.11 Planning

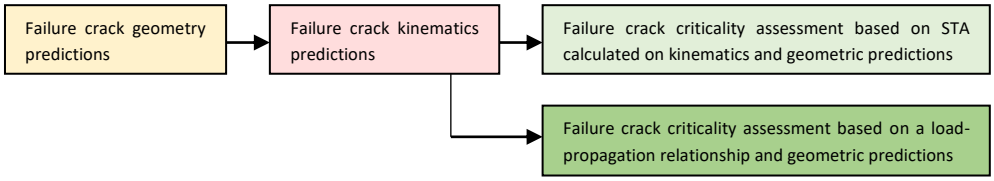

Limitations of nonlinear finite element analysis in beams with low shear reinforcement ratio

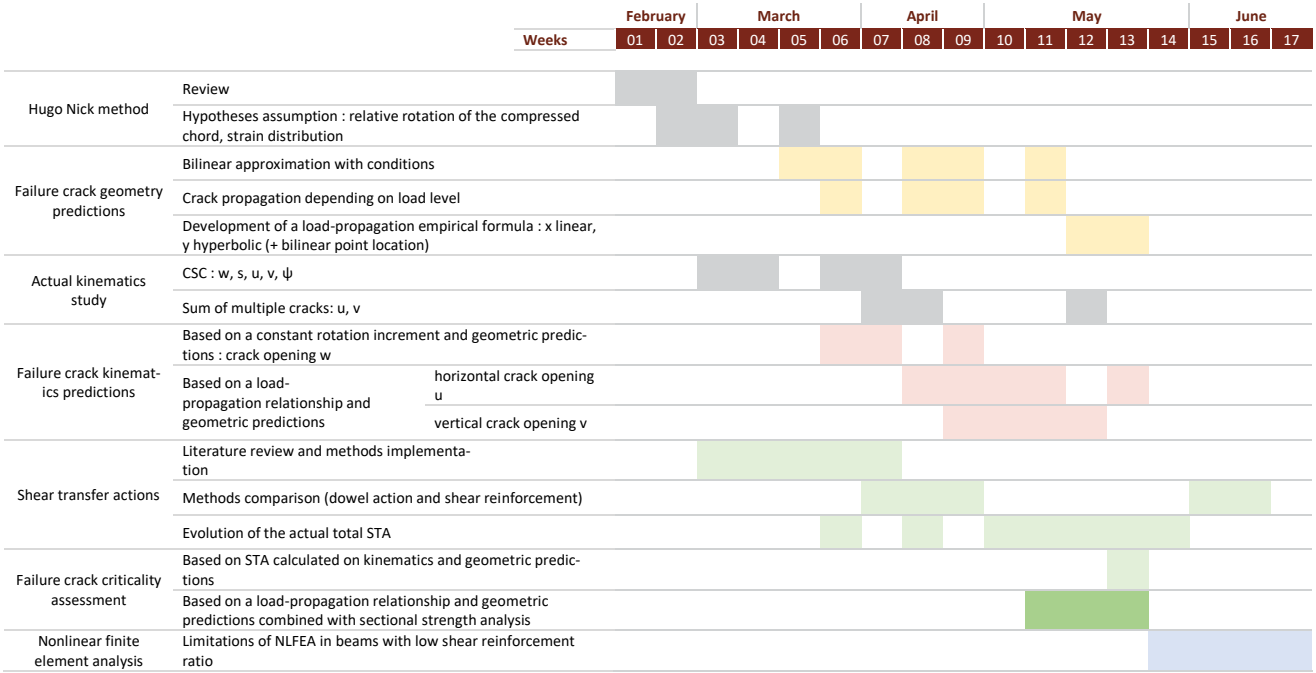

12 Notation

The main symbols and nomenclature used in the present report are as follows:

$A_{c,eff}$	effective concrete area
A_s	flexural reinforcements area
E_c	concrete Young modulus
E_{hard}	steel hardening modulus
E_s	flexural reinforcement Young modulus
E_{sw}	stirrups Young modulus
G_F	Fracture energy of concrete
I	moment of inertia
L_i	distance between the measured crack point i and the center of rotation
M	bending moment
$M_{cracking}$	cracking bending moment
M_s	flexural reinforcement bending moment
M_{tip}	bending moment a the crack tip section
V	shear force
V_{agg}	aggregate interlock vertical force
V_{ca}	cantilever action vertical force
V_{cc}	compression chord vertical force
V_D	dowel action vertical force
V_{max}	ultimate load
V_R	shear strength
V_{res}	concrete residual tensile strength vertical force
V_{sw}	transversal reinforcement shear force
$X_{bilinear}$	y-coordinate of the slope change point (bilinear approximation)
$Y_{bilinear}$	y-coordinate of the slope change point (bilinear approximation)
a	shear span
b	section width
b_{tot}	total width
b_w	web width
c	depth of the compression zone
c_1, c_2	coefficients (Hordijk (1992) [12])
d	section effective depth
d_b	bar diameter
d_{dg}	average roughness parameter
d_F	vertical distance from the tip of the crack to the flexural reinforcement
d_{FOM}	depth of the optical fibres inside the slit
d_g	maximum aggregate diameter
dH	horizontal propagation increment
d_{sw}	stirrups diameter
e	finite element length
err_{DIC}	DIC measurement error
f_c	concrete compressive strength
$f_{c,eff}$	effective concrete compressive strength
f_{cp}	corrected concrete compressive strength
f_{ct}	concrete tensile strength
f_y	reinforcement yield strength
f_{yw}	stirrups yield strength
f_t	reinforcement ultimate tensile strength
f_{tw}	stirrups ultimate tensile strength
h	section height
k_b	strength reduction factor (Cavagnis et al. (2018) [8])
l_B	consideration length of the CSC tributary cracks (Cavagnis et al. (2018) [8])
l_F	quasi-horizontal critical crack length (Cavagnis et al. (2018) [8])
l_{da}	unbounded length (Cavagnis et al. (2017) [3])
l_{trib}	tributary length (Cavagnis et al. (2018) [8])
n	number of bars
s	crack slip; stirrups spacing
s_{rm}	crack spacing
u	horizontal displacement between crack lips
$u_A = u_s$	horizontal displacement between crack lips at the height of the tensed flexural reinforcements

v	vertical displacement between crack lips
w	crack opening
w_c	maximum crack width for stress transfer
$w_{\perp \mathbf{L},i}$	crack opening perpendicular to L_i
x	horizontal coordinate
x_d	dowel action distance (Cavagnis et al. (2017) [3])
x_{tip}	x-coordinate of the tip of the failure crack
$x_{\psi,2}$	point from which the rotation of the compression chord relative to the assumed rigid body under the CSC stops being constant
y	vertical coordinate
y_{tip}	y-coordinate of the tip of the failure crack
y_{top}	vertical distance between the CSC tip and the top surface of the beam
α	horizontal crack angle; crack inclination
α_1	horizontal angle of the quasi-vertical part of the critical shear crack (bilinear approximation)
α_2	horizontal angle of the quasi-horizontal part of the critical shear crack (bilinear approximation)
β_{BF}	quasi-horizontal critical crack angle (Cavagnis et al. (2018) [8])
Δ	crack sliding
δ	displacement capacity
ε	normal strain
ε_{FOM}	optical fibres measured strain
ε_s	flexural reinforcement strain
ε_{uw}	stirrups ultimate strain
ε_{yw}	stirrups yield strain
$\varepsilon_{1,2}$	principal strains
ζ	integration parameter; dilatancy angle
η_{fc}	brittleness factor
η_w	efficiency factor
η_ε	concrete softening factor
λ_i	horizontal angle of the segment linking the rotation centre to a crack point i
ρ	flexural reinforcement ratio
ρ_{eff}	effective reinforcement ratio
ρ_{sw}	transverse reinforcement ratio
σ_{agg}	normal aggregate action stresses
σ_N	prestressing stress
σ_{res}	residual tensile stress of concrete
σ_{sr}	stress in reinforcement after cracking
σ_{sw}	stress in transverse reinforcement
τ_{agg}	tangential aggregate action stresses
τ_{b0}	bound stress before yielding
τ_{b1}	bound stress after yielding
φ	concrete friction angle
χ_s	flexural reinforcements curvature
ψ	rotation
$\emptyset_{c,eff}$	effective concrete area diameter

13 References

[1] Andrea Monserrat López, Miguel Fernández Ruiz, Pedro Miguel Sosa (2021). *The influence of transverse reinforcement and yielding of flexural reinforcement on the shear-transfer actions of RC members.* Engineering Structures, Volume 234, 2021, 111949, ISSN 0141-0296, https://doi.org/10.1016/j.engstruct.2021.111949.

[2] Campana S, Anastasi A, Fernández M, Muttoni A. (2013). Analysis of shear-transfer actions on one-way RC members based on measured cracking pattern and failure kinematics. Mag Concr Res. 2013;65(6):386–404.

[3] Cavagnis, Francesco & Fernández, Miguel & Muttoni, Aurelio. (2017). *An analysis of the shear-transfer actions in reinforced concrete members without transverse reinforcement based on refined experimental measurements.* Structural Concrete. 19. 10.1002/suco.201700145.

[4] Cavagnis, Francesco & Fernández, Miguel & Muttoni, Aurelio. (2015). *Shear failures in reinforced concrete members without transverse reinforcement: An analysis of the critical shear crack development on the basis of test results.* Engineering Structures. 103. 157-173. 10.1016/j.engstruct.2015.09.015.

[5] Classen M. (2020). *Shear Crack Propagation Theory (SCPT) – The mechanical solution to the riddle of shear in RC members without shear reinforcement*, Engineering Structures, Volume 210, 110207, ISSN 0141-0296, https://doi.org/10.1016/j.engstruct.2020.110207.

[6] Fernández M, Muttoni A, Sagaseta J. (2015). *Shear strength of concrete members without transverse reinforcement: a mechanical approach to consistently account for size and strain effects.* Eng Struct 2015;99:360–72.

[7] Fernández M. (2021). *The influence of the kinematics of rough surface engagement on the transfer of forces in cracked concrete*, Engineering Structures, Volume 231, 111650, ISSN 0141-0296, https://doi.org/10.1016/j.engstruct.2020.111650.

[8] Francesco Cavagnis, Miguel Fernández Fernández, Aurelio Muttoni. (2018). *A mechanical model for failures in shear of members without transverse reinforcement based on development of a critical shear crack*, Engineering Structures, Volume 157, Pages 300-315, ISSN 0141-0296, https://doi.org/10.1016/j.engstruct.2017.12.004.

[9] Galkovski, Tena, Jaime Mata-Falcón, and Walter Kaufmann (2022). *Effective Reinforcement Ratio of RC Beams: Validation of Modelling Assumptions with High-Resolution Strain Data. Structural Concrete* (in press). doi: https://doi.org/10.1002/suco.202100739.

[10] Galkovski, Tena & Lemcherreq, Yasmin & Mata-Falcón, Jaime & Kaufmann, Walter. (2021). Fundamental Studies on the Use of Distributed Fibre Optical Sensing on Concrete and Reinforcing Bars. Sensors. 21. 7643. 10.3390/s21227643.

[11] G. C. Frantz and J. E. Breen (1978). *Control of cracking on the side faces of large reinforced concrete beams*, p. 262, 1978.

[12] Hordijk DA. (1992) *Tensile and tensile fatigue behaviour of concrete; experiments, modelling and analysis.* Heron. 37(1):3–79.

[13] Marti, Peter & Alvarez, Manuel & Kaufmann, Walter & Sigrist, Viktor. (1998). *Tension Chord Model for Structural Concrete.* Structural Engineering International. 8. 287-298. 10.2749/101686698780488875.

[14] Monney, F. (2022). *Revisiting Detailing Rules for Bending Bars, Anchorage and Minimum Shear Reinforcement in Concrete Structures* (Doctoral thesis). EPFL.

[15] Muttoni A, Fernández M (2018-2019). *Polycopié « Structures en béton : conception, dimensionnement et vérification ».* Faculté de l'environnement naturel, architectural et construit ENAC, section génie civil, Laboratoire de construction en béton IBETON, EPFL (Lausanne).

[16] Muttoni A, Fernández M. (2008). *Shear strength of members without transverse reinforcement as function of critical shear crack width*. ACI Struct J 2008;105:163–72.

[17] Nick, Hugo. (2023). *Détection automatique des fissures dans les ouvrages d'art* (Master thesis). EPFL.

[18] Nicola Gehri, Jaime Mata-Falcón, Walter Kaufmann. (2020). Automated crack detection and measurement based on digital image correlation, Construction and Building Materials, Volume 256, 119383, ISSN 0950-0618, https://doi.org/10.1016/j.conbuildmat.2020.119383.

[19] Niketić F. (2017). *Development of a consistent approach for design and assessment of structural concrete members using stress fields and strut-and-tie models* (Doctoral thesis). EPFL.

[20] Nonis, Christopher & Niezrecki, Christopher & Yu, Tzuyang & Ahmed, Shafique & Su, Chefu & Schmidt, Tim. (2013). *Structural Health Monitoring of Bridges using Digital Image Correlation.* Proceedings of SPIE - The International Society for Optical Engineering. 8695. 869507. 10.1117/12.2009647.

[21] Pantoja-Rosero B.G., dos Santos K.R.M., Achanta R., Rezaie A., Beyer K. (2022). *Determining crack kinematics from imaged crack patterns*, Construction and Building Materials, Volume 343, 128054, ISSN 0950-0618, https://doi.org/10.1016/j.conbuildmat.2022.128054.

[22] Rupf M. (2014). *Querkraftwiderstand von Stahlbeton- und Spannbetonträgern mittels Spannungsfeldern* (Doctoral thesis). EPFL.

[23] Ulaga T. (2003). *Betonbauteile mit Stab- und Lamellenbewehrung: Verbund- und Zuggliedmodellierung* [PhD thesis]. Thesis no. 15062 [in German]. Zurich, Switzerland: ETHZ; 2003:160.

[24] Vecchio FJ, Collins MP. (1986). *The modified compression field theory for reinforced concrete elements subjected to shear*. ACI J. 83(2):219–231.

[25] Walraven JC. (1981). *Fundamental analysis of aggregate interlock.* J Struct, Div.1981;107(11):2245–2270.